POLITECNICO DI TORINO

Master's Degree in Aerospace Engineering

Master's Degree Thesis

Aerodynamic drag estimation based on the Energized Wake Area approach

Supervisors
Dr. Andrea Sciacchitano
Prof. Gaetano Iuso
Eng. Edoardo Saredi

Candidato
Davide Grassi

December 2021

Summary

Aerodynamic drag determination of transiting objects is relevant in many sectors, such as speed sports and the automotive industry. Typical approaches for on-site drag determination rely on the use of power meters and modelling of the energy budget in cycling, or the coast down technique in automotive. Recently, the research team of TU Delft has introduced the Ring of Fire system for on-site drag determination, which relies on large-scale stereoscopic PIV measurements in combination with the conservation of momentum in a control volume. Although the approach has been proven effective for the combined drag determination and quantitative visualisation of the flow field behind the model, it does require an expert user to process the acquired images. Recently, McPhaden and Rival (2018) proposed the Lagrangian drift volume approach for the unsteady drag determination of an accelerating object. Based on the Lagrangian drift volume approach, the Energized Wake Area (EWA) model has been developed in this project, for the experimental evaluation of constant speed-moving objects' drag. The model has been used to determine the drag of both two-dimensional bluff and streamlined bodies. The results have then be compared with those obtained with the conservation of momentum in a control volume. The activities conducted during the project include:

- Literature study on large-scale PIV and loads determination from PIV.
- Analysis of the existing and new data acquired via dedicated experiments using the new-developed model.
- Comparison of the results with those obtained via the conservation of momentum.
- Synthesis of the research approach, results and conclusions.

Contents

Chapter 1

Introduction

From an ice-skater to a professional cyclist during the Olympics, from a super-bike to an F1 car during a race, from a peregrine falcon to an airplane flying in the sky. From the slowest to the fastest, every object moving through air is affected by a force pulling it back: Aerodynamic Drag.

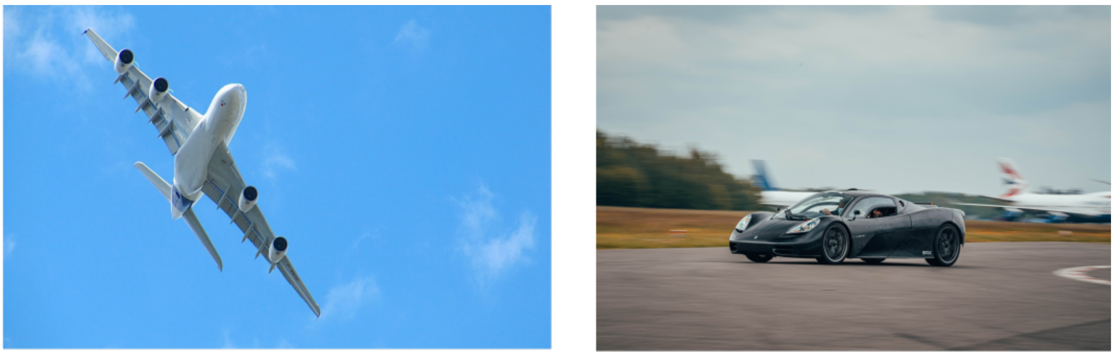

Figure 1.1: Examples of relevant industrial and sportive study cases for aerodynamic drag determination.

As stated by (Anderson Jr 1985), nature transmits forces from a fluid to a body only through skin friction and pressure. Those contributions vary depending on the shape of a body and the kind of flow. Typical bluff bodies present a high amount of pressure drag and a low percentage of friction drag. On the other hand, streamlined bodies exhibit much lower drag forces, most of which is due to friction. The total drag acting on a body depends upon different several parameters e.g. the body shape and dimension, its velocity and the fluid's characteristics. Through the dimensional analysis, it is possible to analytically express the aerodynamic drag:

$$D = \frac{1}{2}\rho A V_B^2 C_D$$

Where ρ is the fluid's density, V_B is the object's velocity and A is the reference area. On the other hand, C_D is the aerodynamic drag coefficient. For many academic, industrial and sport applications, the importance of determining the aerodynamic drag is undiscussed. During the past years, it was common to rely on balance measurements to retrieve the forces acting on the body. However, the latter does not give an insight into the essential physical relationship between the flow field's topologies and aerodynamic drag. A characteristic strictly correlated with the drag generated by an object is its wake. As a matter of fact, the wake is one of the most important feature of the problems external aerodynamics. The wake-flow behind a body hides some intriguing secrets about the drag generation; the wake's size, its turbulent structures, its energy content, and finally its momentum and pressure deficits are all strictly connected to the total amount of drag. One of the most established methods in this aspect is the Momentum Control Volume Approach. The latter takes advantage of the momentum balance equation in a control volume enveloping the fluid domain; this way, it is possible to correlate salient information from the flow's topologies to the drag generated at every point in the control volume. Knowledge of the velocity is required to retrieve the information necessary for drag quantification; for such a task, Particle Image Velocimetry is well-established. Many as (BW Van Oudheusden, Scarano, and Casimiri 2006),(Kurtulus, Scarano, and David 2007),(Laurent David, Jardin, and Farcy 2009) and (Rival and Bas Van Oudheusden 2017b) took advantage of this combination, leading to accurate loads estimation results. In the last years, a novel method for the quantification of drag of moving objects drag has been developed and improved by the Delft University of Technology research team during the work of (Spoelstra, Maximilian Hirsch, et al. 2020). The latter system is named Ring of Fire, it consists of a combination of large-scale Particle Image Velocimetry and the Momentum Control Volume approach. Despite the advantages and wide range of possibilities, the Momentum Control Volume Approach is far from being perfect. Its dependence on the Control Volume's dimensions and the spatial resolution, as well as the necessity of the pressure field , make the Momentum Control volume a not-trivial instrument.

Figure 1.2: Wake-flow behind a moving human model, reproduced from (Tao et al. 2018)

Furthermore, PIV requires experienced users due to the hidden complexity behind PIV data-processing phases. Fascinating new possibilities have been recently introduced by (McPhaden and Rival 2018) and (Galler, Weymouth, and Rival 2021). Those works have been developed based on the early-introduced concept of Lagrangian-Drift-Volume (Darwin 1953). The idea of extracting drag from the mere knowledge of which part of the fluid is moving is indeed intriguing. However, those concepts have been developed for accelerating bodies. Hence, a relationship between those concepts and a wide range of steady-velocity study cases is still missing. The current work is focused on looking for such a relationship. The problem is tackled by considering steady objects in wind tunnels, when the flow is moving with respect to the object. The main goal is perform a first step in the direction of reducing the complex process of aerodynamic loads determination, while still giving insight into the drag-generation mechanisms. After a literature review on the already-existing load determination methods, the new model, namely Energized Wake Area (EWA), has been analytically developed. In order to properly validate the model, an experimental analysis, consisting of 2D2C PIV measurements, was conducted. A final results comparison between the EWA model and the renowned Momentum Control Volume approach has then been carried out. As a first attempt, different two-dimensional bluff bodies and a NACA-0012 airfoil have been chosen. Despite the approach being dedicated to moving objects, the experimental reproduction of a translating body is not trivial. Hence, the investigation is performed via wind tunnel experiments using stationary objects.

Chapter 2

Particle Image Velocimetry

Developed at the Von Karman Institue for Fluid Dynamics in the early 1980s, Particle Image Velocimetry is nowadays one of the most utilized measurement techniques in fluid dynamics applications.
In the first section of the following chapter the theory behind the technique as well as its principal requirements will be exposed; focus has been put on the basic configuration of the PIV technique since it is of particular interest for the present work. Despite the method developed in the present work has been assessed on stationary bodies, its final aim is to be used to estimate the aerodynamic drag of translating ones. Hence, the last part of this chapter puts attention on the principal PIV applications for translating bodies.

2.1 Particle Image Velocitmetry Technique

In its most basic configuration, the PIV technique aims to measure the 2D velocity field on a planar section through the use of a particular system schematized in the Fig. 2.1.

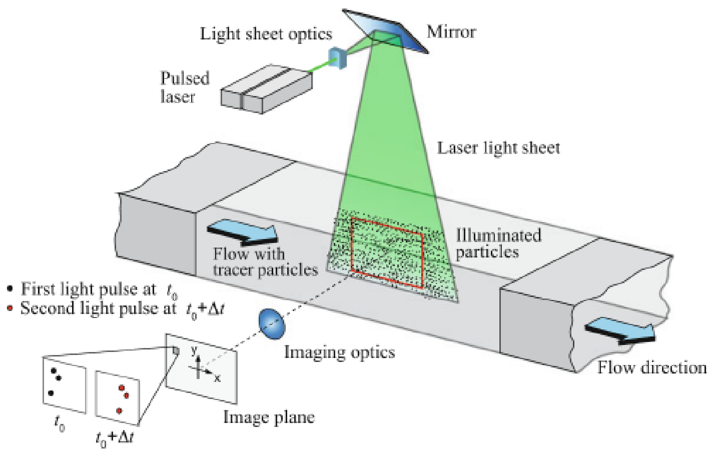

Figure 2.1: Planar PIV setup, reproduced from (Raffel et al. 2018).

The basic principle behind the technique is based on the quantitative flow visualization; this is made possible thanks to some particular seeding particles named "Tracers" which can scatter the light when illuminated by it. The source of light is usually provided by a planar laser sheet which illuminates a portion of the flow field; the laser sheet is usually generated by a pulsing laser which emits two consecutive pulses separated by a temporal interval Δt. In order to capture the tracers' position in different temporal instants, the source of light is coupled with a camera. Using this particular setup it is possible to visualize the tracers' displacements, it is then possible to derive the instantaneous velocity as the ratio between the displacement the time separation between the laser pulses:

$$V = \frac{\Delta s}{\Delta t} \Rightarrow \begin{cases} u = \frac{\Delta x}{\Delta t} \\ v = \frac{\Delta y}{\Delta t} \end{cases}$$

The PIV is a unique completely non-intrusive technique providing high spatial-resolution velocity fields; one of the main advantages of the technique is in fact that external instruments which could potentially disturb the flow are not needed. Despite the main theoretical concept is indeed pretty simple, the PIV technique is demanding in terms of specific requirements that need to be met. The main problems of the technique are often linked to its complexity and the physical limits of the setup. Another drawback is the necessity of an expert user during the image pre-processing and processing phases; The images acquired during the measurements need to be treated to allow a clear distinction of the tracers from the background. Furthermore, the whole measurement plane must be divided into more little ones to correlate the tracers' different positions. These steps involve the use of complex statistical correlation algorithms, which are usually very demanding in accuracy and experience.

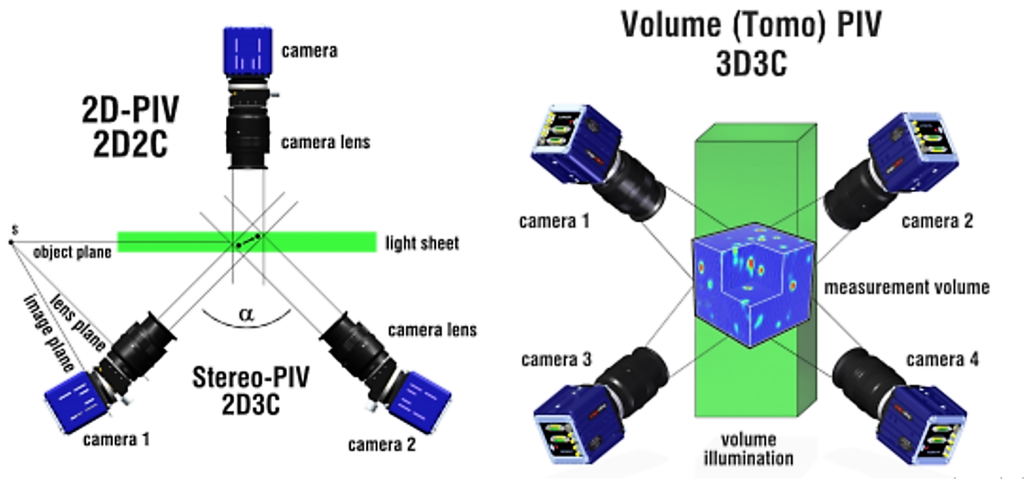

Figure 2.2: Sketches of the differencies between 2D2C,2D3C and 3D3C PIV experimental setups, reproduced from (LaVision 2017).

Since the development of its initial basic configuration, the PIV technique has undergone huge improvements. During the years many variations have been developed both to reduce or eliminate some of its drawbacks and to unlock its true potential. A renowned example is the Time-Resolved PIV, its aim is to increase the temporal resolution of the technique by emitting the laser source at high-frequency repetition. Other famous evolutions concern the possibility of retrieving all of the velocity components through 2D-3C or even 3D-3C advanced systems. Stereoscopic PIV and Tomographic PIV are classical examples of those kinds of techniques. As showed in the sketch reported in Fig.2.2 their main goal is to provide 3C (three component) velocity fields in a flow's section and a flow's volume. Many other different PIV techniques have been also developed to adapt the technique to different kinds of problems; some examples can be retrieved in literature for problems that involve micro-measurements in Brownian motions or measurements for the determination of flow's temperature field (Loboda et al. 2018; Meinhart, Wereley, and Santiago 1999; Santiago et al. 1998).

2.2 Tracer Particles

The physical properties of the particles used as tracers are vital factors that heavily affect the measurement's accuracy. The velocity measured through the PIV technique is, as a matter of fact, the velocity of the tracers particles themselves. It is then desirable that the chosen particles must follow the flow with the higher accuracy achievable. Furthermore, the light-scattering properties of the particles have to be taken into account to obtain a successful measurement. In order to quantify the tracers ability to follow the flow it is possible to utilize the Stokes number; it is defined as the ratio between the particle's response time and the flow's characteristic time:

$$\begin{cases} \tau = \frac{c}{U} \\ \tau_p = d_p^2 \frac{(\rho_p - \rho)}{18\mu} \end{cases} \Rightarrow St = \frac{\tau_p}{\tau}$$

Where the flow characteristic time is obtained as the fraction of the problem's characteristic length c over the flow's velocity U.

Figure 2.3: HFSB application for a Robotic PIV on a full-scale cyclist model, reproduced from (Jux et al. 2018).

The particle's characteristic time is a function of the particle's diameter d_p, the viscosity μ and finally the difference between particle and flow's density $\rho_p - \rho$. For the particles to be able to carefully follow the flow, the Stokes must not be higher than 0.1. As a consequence, the particle's characteristic time must be as low as possible. The choice of the particle to utilize as tracers must be then made such that the difference between the densities or either the particle's diameter is as low as possible. The kind of particles usually used in PIV techniques presents a much higher density than the flow's one, this is true especially in the case of gas experimentations. The main parameter characterizing τ_p is the particle's diameter, hence utilizing small sized particles would seem an optimal choice aimed to obtain a sufficently low time response. As reported by (Raffel et al. 2018), Mies's light-scattering theory enunciates that the ability to reflect the light is directly proportional to the square of the particle's diameter. It needs to be taken into account that the theory is applicable only when the particle diameter is larger than the wavelength of the illuminating source. Major advantages can be achieved by observing the scattered light from 180 degrees in respect to the light source. This feature is due to the peak of light scattered in that direction. Despite this great advantage PIV techniques usually present physical limitations related to the depth of field (DOF), the direction used to capture the scattered light is then usually set at about 90 degrees from the light source. A trade-off between the ability to faithfully follow the flow and the light-scattering properties needs thus to be made. The choice of the tracers also depends upon the application purposes, oil, di-ethyl-hexyl-sebacat (DEHS) and fog particles are the most commonly utilized for airflow seeding. An exceptional alternative has been introduced by (Caridi 2018) through the use of helium-filled soap bubbles (HFSB); by means of these particular tracers, it is possible to obtain both of the characteristics required for the tracers at the same time. The density of the bubble is in fact comparable with the air's one, thus allowing to increase the diameter of the bubble itself. This way the tracers present both a very low τ_p and good light-scattering abilities. An example of HSFB application has been reported in Fig.2.3.

2.3 Imaging System

The images of the illuminated particles in the object plane are obtained by a digital camera equipped with an objective. The sCMOS sensors of the camera form the image plane and capture the intensity of the illuminated particles;a schematic representation of the imaging system has been reported in Fig.2.7.

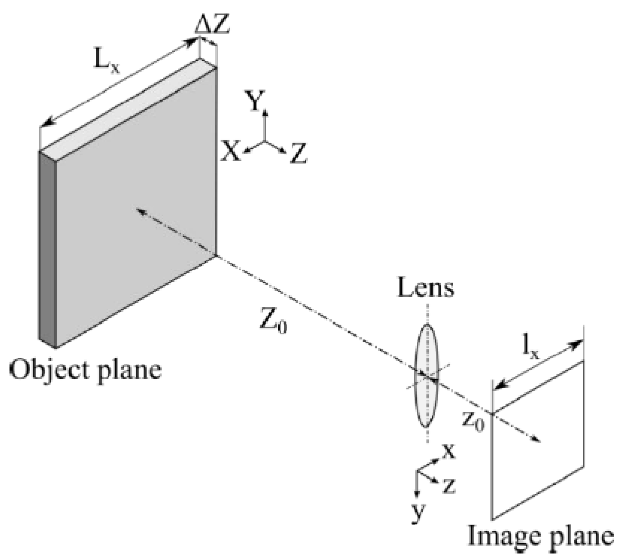

Figure 2.4: Schematic representation of PIV Imaging System, reproduced from (Andrea Sciacchitano 2014).

The imaging system is characterised by some fundamental parameters:

- The magnification M is defined as the ratio of image distance to object distance:
$$M = \frac{z_0}{Z_0} = \frac{\text{sensor size}}{\text{objective size}} = \frac{\text{n. of pixel x pixel size}}{\text{field of view}}$$
- The focal length f is the measure of lens's capacity to converge or diverge light,it physically rapresents the distance between the center of the lens and its focal point:
$$\frac{1}{f} = \frac{1}{z_0} + \frac{1}{Z_0}$$
Where f is the lens focal length,z_0 is the image distance and Z_0 is the object distance. In general, the focal length is a peculiar characteristic of the lens; it can be however adjusted in agreement with the needs by setting the correct distance between the lens's plane and the image plane. A high focal length results in higher magnification and narrow-angle of view, on the other hand, a low focal length leads to a lower magnification and a wide-angle of view.
- The f-stop $f_\#$ is a parameter defined as the ratio between the focal length and the camera's objective's aperture:
$$f_\# = \frac{f}{D}$$
Where f is the lens focal length and D is the aperture diameter of the lens. The $f_\#$ is the principal parameter determining both the depth of field (DOF) and the brightness; a high $f_\#$ means a low amount of light and so darker the image and larger DOF. On the other hand, a low $f_\#$ results in a brighter image with a smaller DOF. A representative sketch of the concept has been reported in Fig.2.5.

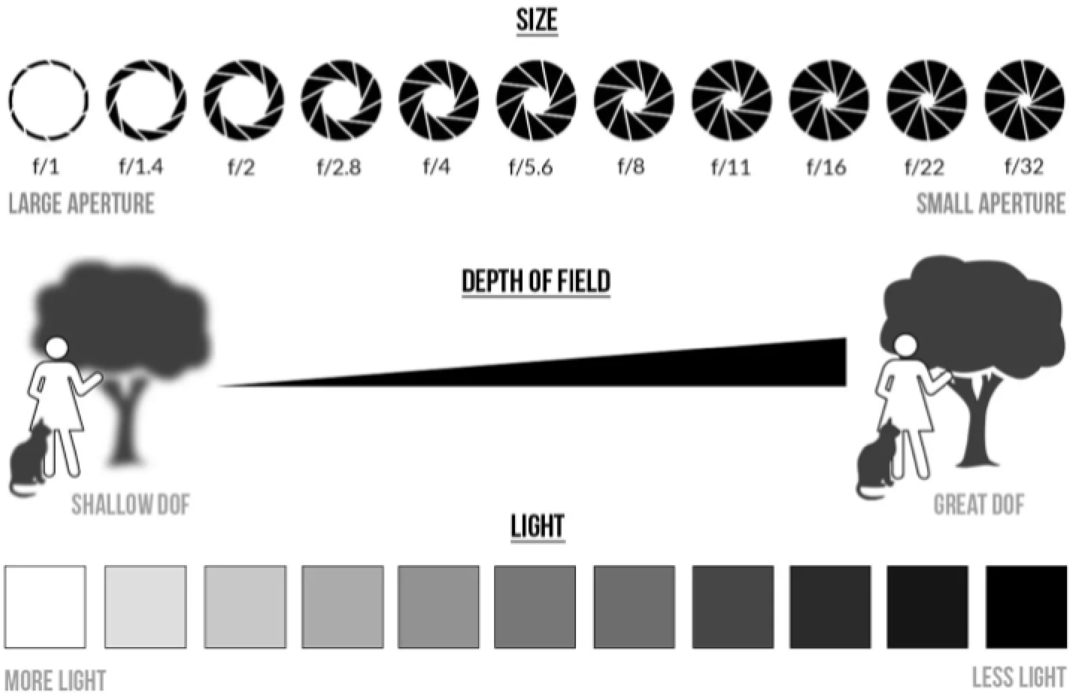

Figure 2.5: Schematic rapresentation of the effect of the $f_\#$ on the image's brightness and depth of focus, reproduced from (KarlTaylorEducation 2020).

Particular attention is needed in the choice of the imaging parameters due to their influence on the images' final quality. As a general rule the $f_{\#}$ should be selected in order to satisfy the following equations:

$$\begin{cases} d_\tau = \sqrt{d_{geom}^2 + d_{diff}^2} = \sqrt{(Md_p)^2 + (2.44\lambda f_{\#}(1+M))^2} \geq 2px \\ \Delta z < 4.88\lambda f_{\#}^2 \frac{(1+M)}{M}^2 \end{cases}$$

Where d_p is the physical particle diameter, λ is the light's wavelength and Δz is the laser sheet thickness. The first relation express the physical effect of diffraction which puts a bottom limit to the imaged particles' size. As stated by (Prasad et al. 1992), peak-locking occurs when the size of the particle images on the sensor becomes too small; hence, d_τ should be larger than $2px$ in order to avoid under-sampled images. The second expression takes instead account of the relationship between the laser sheet thickness and the DOF, in order to have all the particles in focus it needs to be larger than the laser sheet thickness.

2.4 Light Sources

The light sources most commonly utilized in PIV application are lasers, they are chosen because of their ability to be shaped into laser sheets. This is also possible by means of particular optical lens,which are able to manipulate the light coming from the laser source.

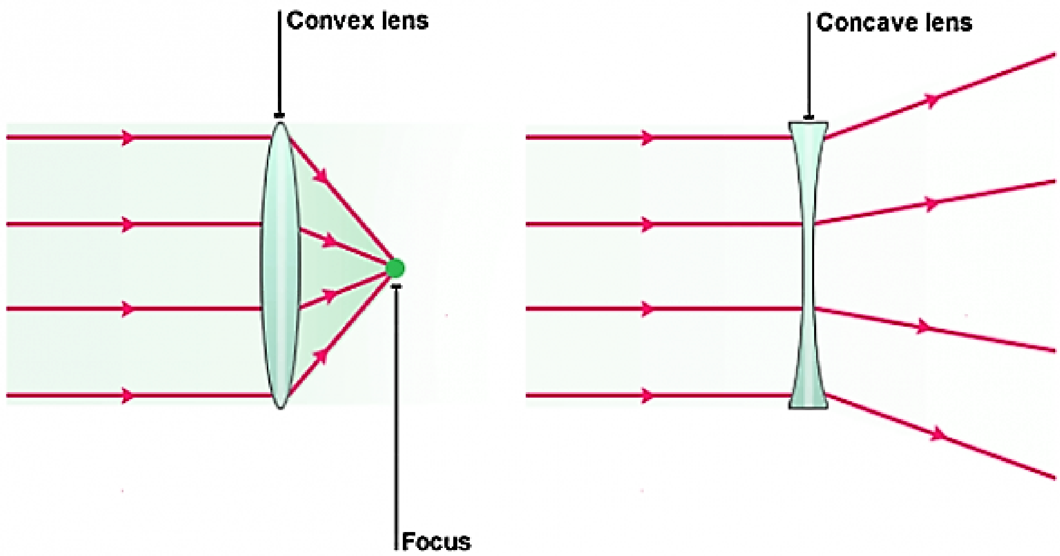

Figure 2.6: Illustration of typical lenses used in PIV measurements.

As shown in Fig.2.6 the lens system usually consists of particular combinations of concave and convex lenses. The former ones present optical expanding capacities meanwhile the latter behave oppositely. By combining both concave and convex lenses it is possible to achieve different kinds of laser sheets, the typical ones for PIV applications are linearly expanding laser sheets. This is due to their capacity to illuminate big regions of space. Common examples of laser are monochromatic high-density light sources such as Nd:YAG (neodymium-doped yttrium aluminum garnet), used for low-speed measurements, or either Nd:YLF (neodymium-doped yttrium lithium fluoride) laser which are used for time-resolved measurements. To achieve a measurement with an elevated grade of temporal resolution the characteristical times of the pulses need to be taken into account. The temporal distance between two consecutive pulses Δt and the time interval between two acquisition ΔT are two important parameters that characterize the technique's properties. A schematic rapresentation of their relationship is reported in Fig. 2.7.

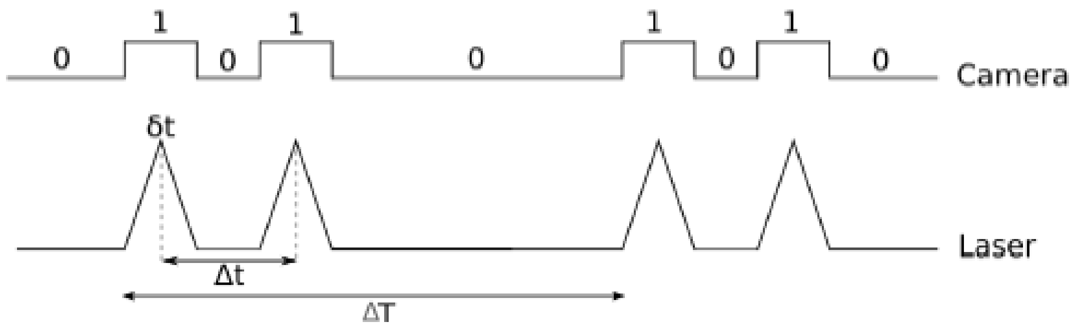

Figure 2.7: Schematic representation of PIV System's temporal characteristics.

The Δt is the one that determines the accuracy of the technique. It usually depends on several factors as the freestream velocity, the Magnification ratio and the particle's displacement. It can then be expressed as:

$$\Delta t = \frac{\Delta x}{MV}$$

Where Δx is the particle displacement in pixel, M is the magnification factor and V is the freestream velocity. In order to capture the particle's displacement, before the particle itself manages to escape the laser or the interrogation window, this time interval needs to be limitated. On the other hand, the time interval ΔT determinates the temporal resolution of the measure, as well as its ability to consecutively acquire several velocity fields in time. Such feature is referred as the acquisition frequency, which also corresponds to the inverse of ΔT.

2.5 PIV correlation algorithms

In order to obtain a single velocity field at least two PIV images are required. Nowadays the most utilized method consists in splitting the PIV images into more interrogation windows, then it is possible to compare the positions of the particles contained in the same interrogation window in two consecutive images. This proceeding is possible by means of particular statistical algorithms; this phase is a crucial milestone for the composition of the final velocity field; the selected interrogation windows need to satisfy particular requirements in order to obtain a faithful velocity field. It is necessary to select an interrogation window's size which can contain a statistically-high number of particles, thus at least 10 particles per interrogation window are required. At the same time, the chosen size needs to be small enough to ensure an high-spatial-resolution and uniform displacement of the particle. For planar PIV measurements, the most utilized technique is the Cross-Correlation algorithm. This kind of algorithm is able to determinate a particle's displacement through the comparison of the particle's position in two interregation windows. The particle's position is founded through a discrete cross-correlation function definite as follow:

$$R(\Delta s) = \sum_{s_0}^{s_0+\Delta s} I_A(s) I_B(s+\Delta s)$$

Where s is the in starting position, Δs is the shift in space and I_A and I_B are the intensities in the two interrogation windows. The cross correlation function is utilized to build a correlation map; the latter presents a peak in corrispondence of the most probable displacement, thus providing the possibility of discerning the istantaneous velocity. A schematic representation of the technique's framework is reported in Fig. 2.8.

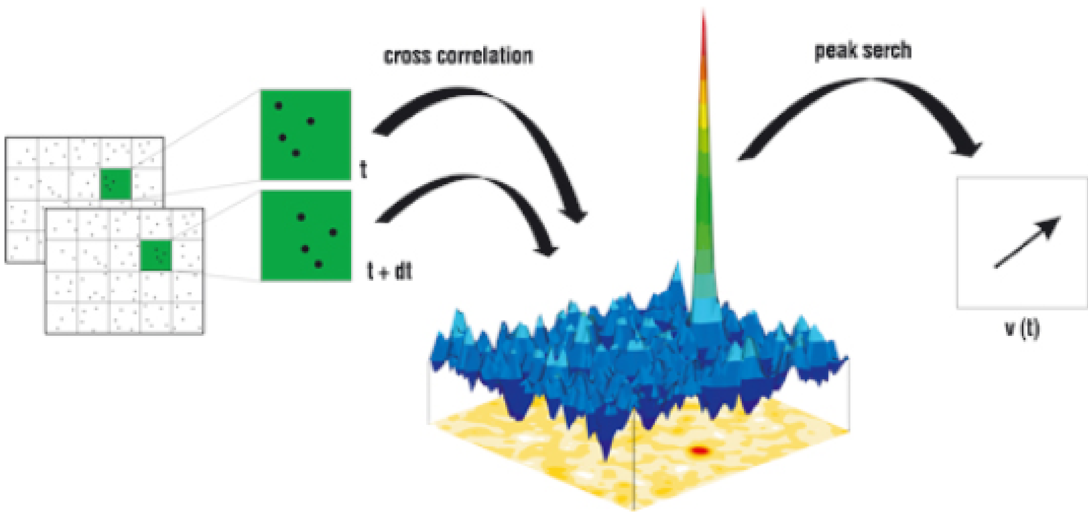

Figure 2.8: Schematic representation of PIV framework, reproduced from (LaVision n.d.).

2.6 Limitation in planar PIV

In the classical planar PIV configuration, the camera axis is orthogonal to the laser sheet; hence, only two the in-plane velocity components can be captured. Despite that, planar PIV is also used for the study of strongly 3D turbulent flows. However, in such cases it is necessary to account for the loss of correlation due to the three-dimensionality of the flow. A common mean of limitating the latter is to utilize a thicker laser sheet. Another undesired effect linked is overestimation of particle displacement. That is mainly related to the perspective angle, this error is caused by the presence of a not-null angle between the camera view axis and the axis connecting the object and its image.

2.7 PIV application for translating bodies

During the years, Particle Image Velocimetry has been implemented in the study of a vast number of aerodynamic problems. Constant-velocity translating bodies are of particular interest for the present work. A fascinating example of PIV application for translating bodies concerns the study of birds' flight; the development of PIV has infact gifted this kind of researches with huge improvements. Of particular interest is the work of (Usherwood et al. 2020), where a Goshawk, a Tawny owl and a Barn owl's gliding techniques have been investigated. In order to understand the role of the raptors' tails on lift, drag and overall stability, their wakes have been investigated. The reconstruction of the characteristics of the wake have been carried out by means of a Lagrangian 4D-PTV, using HFSB as tracer particles. Some results have been reported in Fig. 2.9.

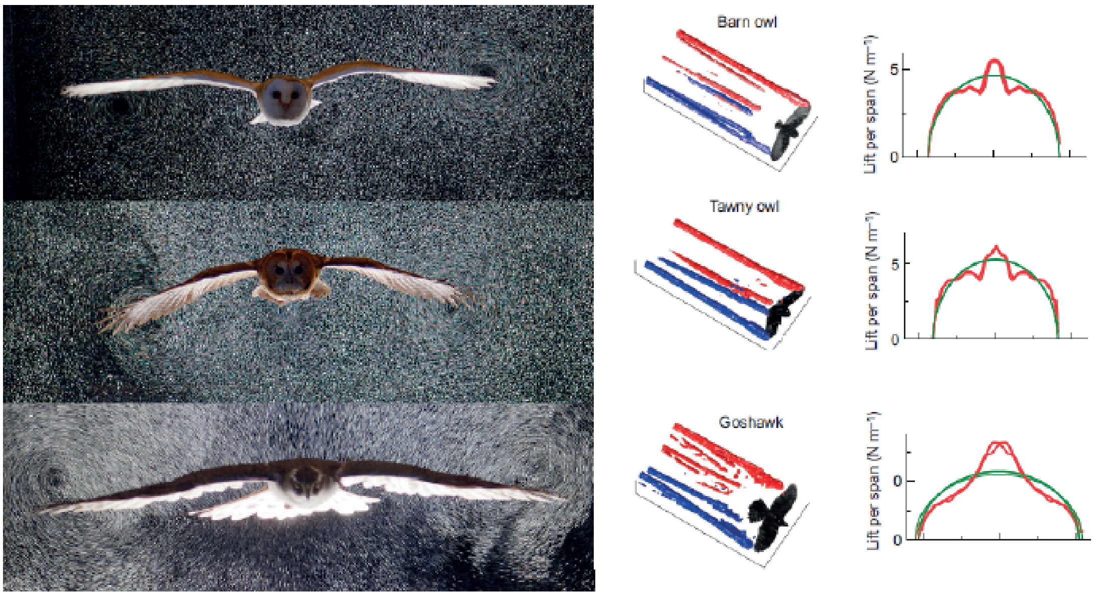

Figure 2.9: Tip Vortecies released by a Goshawk,a Tawny owl and a Barn owl gliding through HFSB (left), Wake Q-criterion iso-surfaces and lift distributions of three gliding raptors (right), reproduced from (Usherwood et al. 2020).

The aim of the experiments was to investigate the interaction between the main vortex structures produced by the birds' passage. The understanding of the vortex structures has allowed the authors to discern the downwash velocity fields. The achieved downwash distributions have been compared with the ones deriving from the classical Prandtl theory. Despite the difficulty presented by the realization of moving experimental setups, many interesting works have been conducted to deepen the knowledge of translating bodies' aerodynamics. Classical examples concern aerospace studies for industrial applications. An interesting study on the wake vortex flow of a large airliner has been carried out by (Scarano, Wijk, and Veldhuis 2002). The experimental setup consisted of a 1:48 model of an A340-300 airliner towed through a laser sheet; the main aim of the experiment was to analyze the complete evolution of the vortex structures in the wake, thus a planar PIV in a towing tank has been chosen for the measurements.

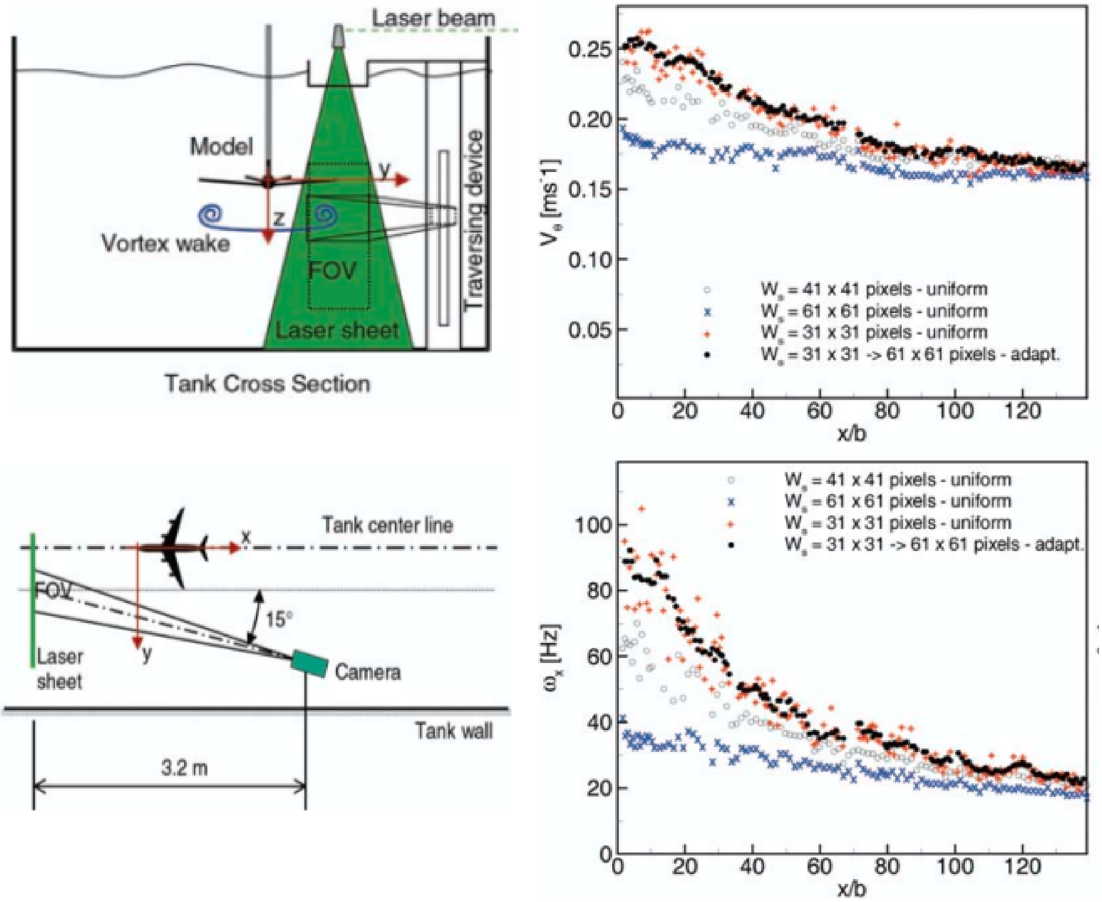

Figure 2.10: Experimental PIV setup of an airliner scale model in a towing tank (left), Maximum tangential velocity and maximum streamwise vorticity in the main vortex structure as a function of the streamwise distance (right), reproduced from (Scarano, Wijk, and Veldhuis 2002)

A vertical translating FOV method has been exploited in order to achieve this task. As showed in Fig.2.10 the results of the study helped to retrieve some interesting information about the vortex's decay process. A comparison with the potential flow theory has been carried out. The results has been found to exhibith a good agreement with agreement with the well-known vortex-pair flows. Another interesting application of PIV measurements for translating bodies has been presented in the study of (Stephens, P. R. Stevens, and Babinsky 2016). The authors investigated the aerodynamic behavior of the underbody of a realistic model of a High Goods Vehicle. The measurements have been conducted by means of a planar PIV in a towing tank. Due to the necessity of reducing the area of laser shadow regions formed by the underbody components, two different laser sheets emanated from both sides in agreement with (P. R. R. J. Stevens 2015) to have been used. Furthermore, the PIV system presented two cameras placed under towing tank in order to achieve a larger FOV. The results reported in Fig.2.11 show that the separation process strongly decreases with the distance from the ground; the maximum rate of separation is then reached at approximately half of the model length.

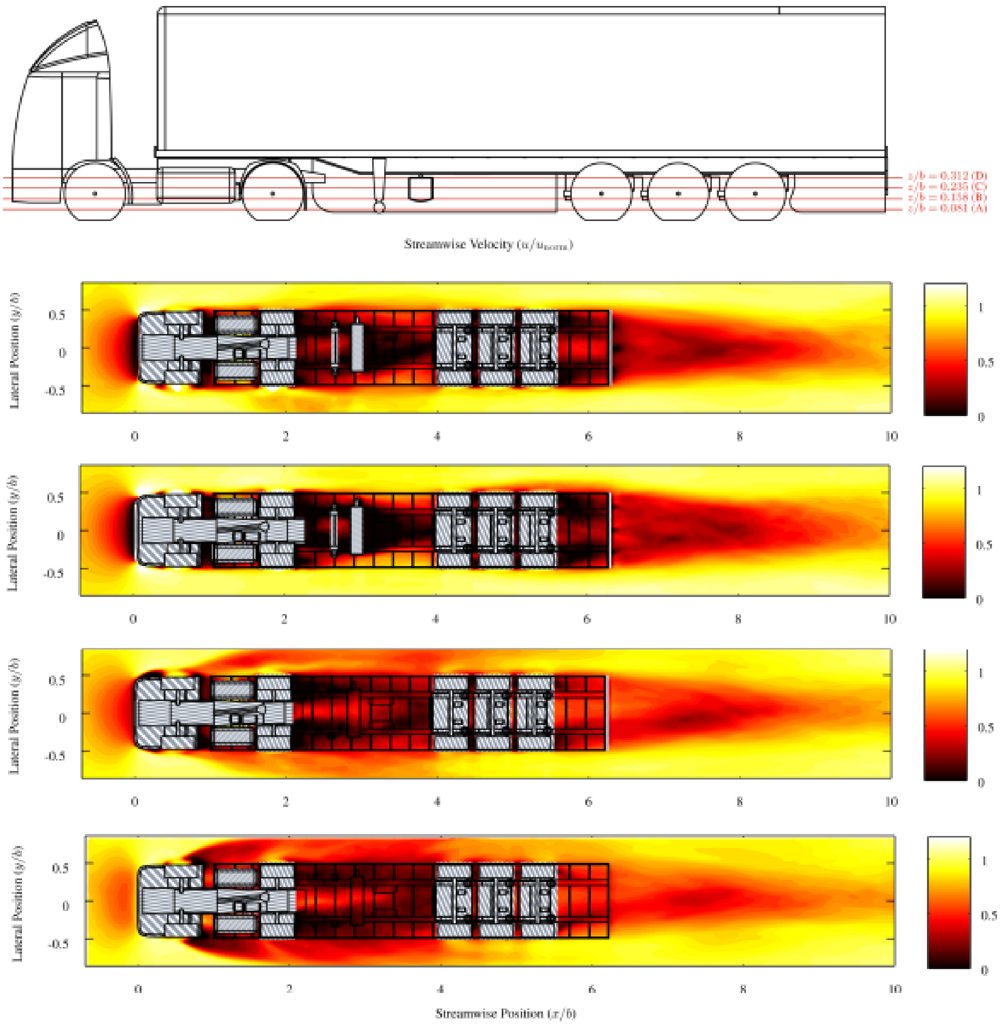

Figure 2.11: Streamwise velocity fields measured at different heights of the underbody from the ground, reproduced from (Stephens, P. R. Stevens, and Babinsky 2016).

On the other hand, two respectively inward and outward entrainment mechanisms have been observed; this behavior is also linked with the distance from the ground. The high-quality vector fields obtained during the measurements work allowed the authors to characterize the underbody flow, and thus the phenomena which lead to drag generation.

Chapter 3

Drag determination from PIV

The load determination from PIV is possible by post-processing the velocity field and achieving the quantities needed for such a goal. The following work aims to estimate the aerodynamic drag, hence both classic and new innovative methods will be introduced.
In particular, the second part of the chapter will provide a physical interpretation of the principles which led to the development of the new analytical model for drag quantification.

3.1 The Momentum conservation Control Volume approach

One of the most common approaches used to determinate the drag consists of evaluating the momentum conservation in a finite control volume enveloping the model. An illustrative scheme of the method applied to a general bluff body is reported in Fig. 3.1.

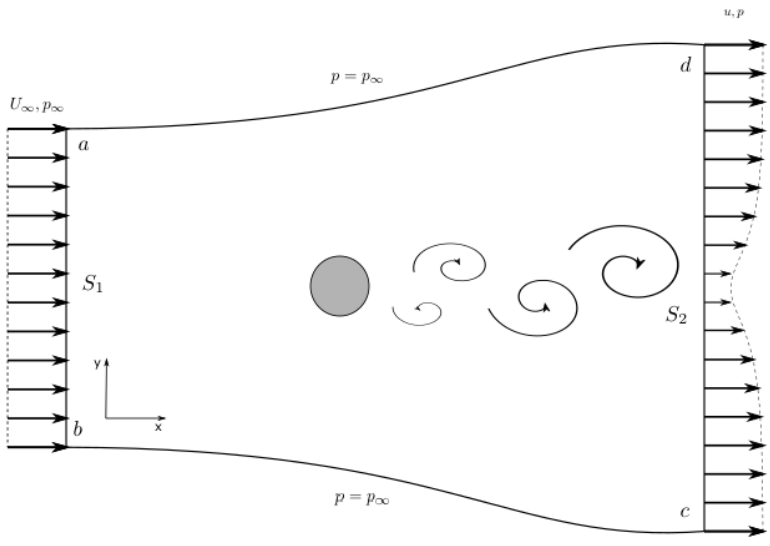

Figure 3.1: Momentum Conservation in a control volume.

This kind of approach is indeed a powerful instrument for the non-intrusive evaluation of aerodynamic loads, especially for cases of moving objects. Furthermore, it allows an insight into the correlation between forces acting on the body and the vortex generation mechanism. Despite its advantages, many factors need to be taken into account in order to provide a correct estimation. Some of those have been analyzed by (Laurent David, Jardin, and Farcy 2009), the control volume's dimension in particular has been shown to play a crucial role. The relative contributions of the various terms forming the total istantaneous drag strongly depends upon the considered volume dimensions, as showed in the results reported in Fig. 3.2.

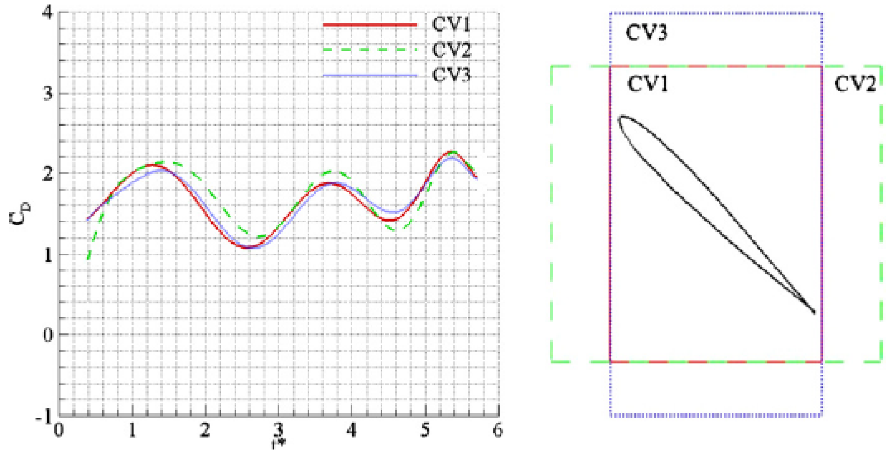

Figure 3.2: Influence of control volume's dimensions on a moving airfoil's drag coefficent,(Laurent David, Jardin, and Farcy 2009).

However, aerodynamic forces acting on a body should be insensitive to the dimensions of the control volume. Despite this, the authors arrived at the conclusion that control volume's different shapes suit better different kinds of problems. Drag determination privileges small volumes to limit errors' propagation. On the other hand, bigger dimensions are needed for different kinds of applications where some momentum balance terms have to be neglected. Assuming that the control volume is wide enough to consider segments far away from the body, the momentum-conservation equation can be derived as follows:

$$D(t) = -\rho \iiint_{CV} \frac{\partial u}{\partial t} dV - \iint_{CS} \rho(\mathbf{V}\cdot\mathbf{n})u dS - \iint_{CS} (p\mathbf{n})_x dS - \iint_{CS} (\tau\mathbf{n})_x dS$$

This expression has been simplified by (Kurtulus, Scarano, and David 2007), which assumes that the control volume is wide enough to neglect the viscous term; it is also possible to split the surface terms in four different contributes, one for each surface of the control volume:

$$\iint_{CS} \rho(\mathbf{V}\cdot\mathbf{n})u dS = \left(\iint_{ab} \rho(\mathbf{V}\cdot\mathbf{n})u dS + \iint_{bc} \rho(\mathbf{V}\cdot\mathbf{n})u dS - \iint_{cd} \rho(\mathbf{V}\cdot\mathbf{n})u dS - \iint_{da} \rho(\mathbf{V}\cdot\mathbf{n})u dS\right)$$

$$\iint_{CS} p\mathbf{n} dS = \left(\iint_{ab} p\mathbf{n} dS + \iint_{bc} p\mathbf{n} dS + \iint_{cd} p\mathbf{n} dS + \iint_{da} p\mathbf{n} dS\right)$$

Considering only the pressure contributes along the streamwise direction and noticing that the scalar product $\mathbf{V}\cdot\mathbf{n}$ is null along the surfaces da and bc when they are chosen as streamlines:

$$D(t) = -\rho \iiint_{CV} \frac{\partial u}{\partial t} dV + \iint_{ab} \rho U_\infty^2 dS - \iint_{dc} u^2 dS + \iint_{ab} p_\infty dS - \iint_{cd} p dS$$

The above expression can be further simplified by considering the mass balance inside the control volume:

$$\rho \iint_{ab} U_\infty dS = \rho \iint_{cd} u dS$$

After multiplying the mass conservation equation by U_∞, the terms inside the momentum balance need to be replaced. The previous expression can be thus reformulated as follows:

$$D(t) = -\rho \iiint_{CV} \frac{\partial u}{\partial t} dV + \iint_{cd} \rho u (U_\infty - u) dS + \iint_{ab} p_\infty dS - \iint_{cd} p dS$$

Last but not least, the pressure deficit contribution can be expressed by simply integrating the pressure difference on the downstream boundary. The final formulation used for instantaneous aerodynamic drag evaluation is:

$$D(t) = -\rho \iiint_{CV} \frac{\partial u}{\partial t} dV + \iint_{cd} \rho u (U_\infty - u) dS + \iint_{cd} (p_\infty - p) dS$$

In case the interest is focused on the average drag acting on the body, the unsteady term of the expression needs to be treated. A common way to achieve such a task consists of computing the drag several times, while neglecting the unsteady term, and then averaging. Another way is to Reynolds-decomposing istantaneous quantities in a mean and a fluctuating contributions, hence obtaining the following expression for the time-averaged drag:

$$\overline{D} = \iint_{cd} \rho \overline{u} (U_\infty - \overline{u}) dS + \iint_{cd} (p_\infty - \overline{p}) dS + \iint_{cd} (-\rho \overline{u'u'} dS)$$

The third term present inside the latter expression is the Reynolds stress term. Such a term emerges from the Reynolds averaging of Navier-Stokes equations. The final mean drag acting on the body is then composed by the momentum deficit inside the control volume, by the pressure deficit inside the control volume, and finally by the Reynolds stress term. The latter in particular, represents the mean momentum rate of transfer due to turbulent fluctuations.

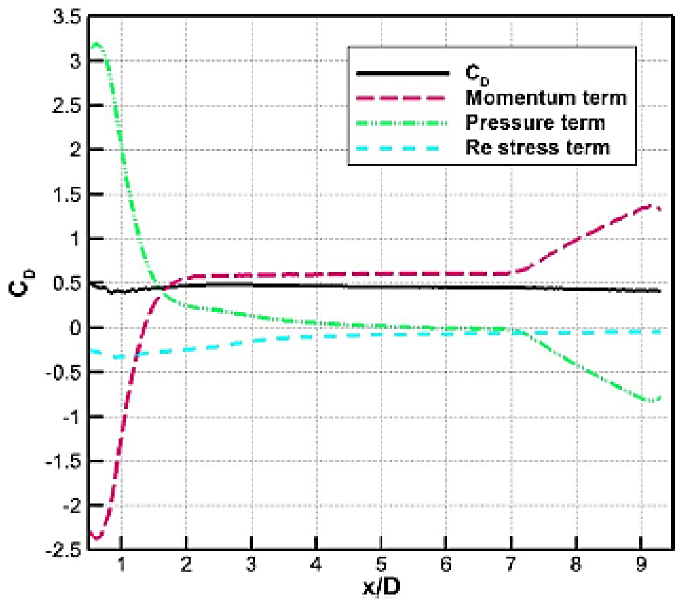

Figure 3.3: Mean drag coefficient variation with the downstram distance from the body, reproduced from (Terra, Sciacchitano, and Scarano 2017).

An analysis of the order of magnitude of these contributes for the case of a translating sphere has been reported in Fig.3.3. It can be seen that the biggest contribution to the main drag is represented by the momentum loss; as stated by (Terra, Sciacchitano, and Scarano 2017), the pressure deficit and the Reynolds stress contributions could also be neglected if the control volume boundary is placed sufficiently downstream. As shown in the momentum balance equation, knowledge of the pressure field is needed in order to estimate aerodynamic drag. PIV measurement techniques can also provide a non-intrusive pressure loads determination by solving the Pressure Poisson Equation. As showed by (BW Van Oudheusden 2013), such equation can be obtained by applying the divergence operator to the momentum conservation equation :

$$\nabla \cdot \left(\frac{\partial(\rho \mathbf{V})}{\partial t} + \rho(\mathbf{V} \cdot \nabla)\mathbf{V} + \nabla p - \mu \nabla^2 \mathbf{V} \right) = \nabla \cdot \left(\frac{\partial(\rho \mathbf{V})}{\partial t} + \rho(\mathbf{V} \cdot \nabla)\mathbf{V} - \mu \nabla^2(\mathbf{V}) \right) + \nabla^2 p$$

Considering an incompressible fluid and neglecting the viscous term, the final expression which leads to the pressure field can be expressed as:

$$\nabla^2 p = -\rho \nabla \cdot (\mathbf{V} \cdot \nabla) \mathbf{V}$$

The above formulation allows the complete evaluation of the pressure field, successful results have been achieved by (Ragni, BW Van Oudheusden, and Scarano 2012). The authors studied the pressure field on the blade tip of an aircraft propeller,some comparative results have been reported in Fig. 3.4.

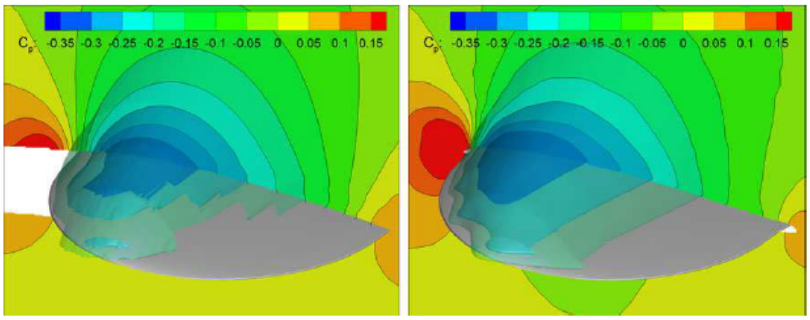

Figure 3.4: Comparison between experimental and numerical pressure distributions, reproduced from (Ragni, BW Van Oudheusden, and Scarano 2012).

According to the Poisson equation, pressure gradients need to be numerically integrated in order to compute the pressure distribution in the domain. To achieve such a task,(Kat and Bas W van Oudheusden 2010) has proposed a 2D PPE solving technique which exploits mixed Neumann and Dirichlet boundary conditions. The combination of PIV investigation and the momentum control volume approach is very attractive; however, when analyzing problem of interest at high Reynolds number, PIV-based techniques are forced to face a dynamic range limitation. As stated by (Rival and Bas Van Oudheusden 2017b), the three-dimensional nature of turbulent flows requires highly-resolved volumetric reconstructions to account for the unsteady and surface contributes.

3.2 The Ring of Fire Concept

As discussed in the previous sections, PIV measurements have nowadays been established in many fluid dynamic laboratories; in most cases, the technique is associated with wind tunnel testing. When it comes to the real situation itself however, wind tunnel tests present several limitations which prevent enough accurate simulations of reality. Of particular interest for experiments involving translating bodies is the problem of the freestream turbulence. The assumption that a pretty much homogenous flow investing a body can exactly represent the real behavior of a body moving in quiescent air is, in most cases, far from being actually true. Little turbulent fluctuations due to the external environment's conditions need to be taken into account to achieve really accurate representations of reality. A recent PIV application which provides on-site aerodynamics measurement is the "Ring of Fire" concept (RoF),the approach has been initially developed by (Spoelstra 2017) and then perfectionated by (Spoelstra, Martino Norante, et al. 2019).

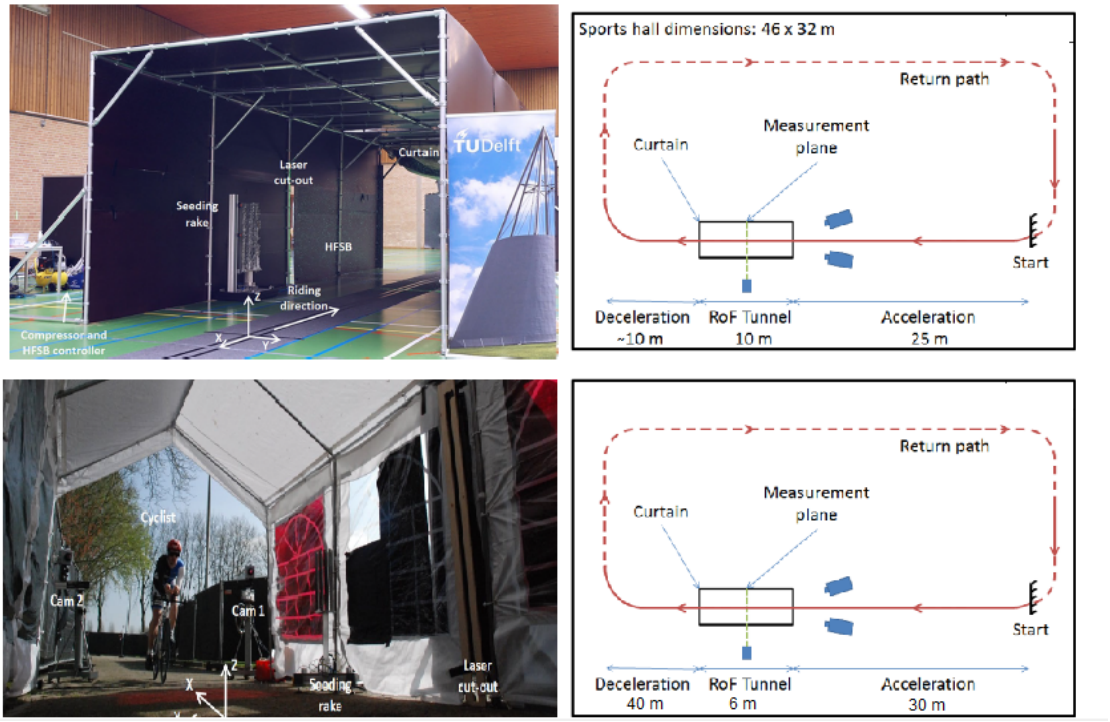

Figure 3.5: Ring of Fire experimental setup, reproduced from (Spoelstra, Martino Norante, et al. 2019).

As showed in Fig.3.5, the RoF is essentially a large-scale stereoscopic PIV technique; the experiments have been conducted in both close and open environments. Low-speed PIV systems have been used for the first case; that is due to the possibility of achieving higher-quality images thanks to a higher sensor resolution. On the other hand, time-resolved high-speed systems offering higher temporal resolution have been used in the second case. The general setup exposed in the picture is composed of two CCD cameras, a laser source that provides the laser sheet, an HFSB rake generator; finally, a duct meant to accumulate bubbles has been utilized to achieve a higher particle density in the measurement plane. The aim of the RoF was originally to evaluate the instantaneous and time-averaged drag of a cyclist; the idea consisted of applying the momentum conservation inside a control volume enveloping the cyclist during its movement. As exposed in the previous section, it is indeed possible to evalutate the drag starting from the knowledge of the velocity field; however, it is necessary to treat the unsteady term in order to pass from a steady problem to a steady one.

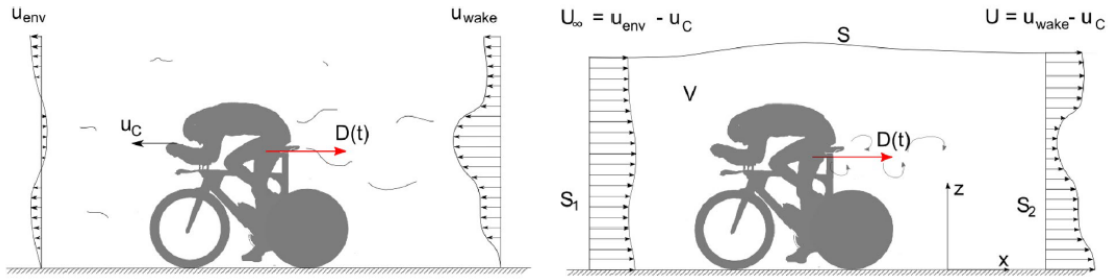

Figure 3.6: Reference frame moving with the cyclist and fixed reference frame in the left and right illustrations, reproduced from (Spoelstra, Martino Norante, et al. 2019).

To achieve such a feature, a Galileian Transformation has been applied. In agreement with (Terra, Sciacchitano, Scarano, and B. v. Oudheusden 2018), the latter permits to switch from the laboratory reference frame to one moving with the cyclist ; thus it is possible to think of the upstream velocity fluctuations as non-uniform flow investing the cyclist. As showed in the illustration in Fig. 3.6, the Galileian transformation can be written as:

$$\begin{cases} U_\infty = u_{env} - u_c \\ u = u - u_c \end{cases}$$

Where u_c is the cyclist's velocity; it is now possible to express the instantaneous drag as follows:

$$D(t) = \iint_{S_1} \rho(u_{env} - u_c)^2 dS + \iint_{S_1} p_1 dS - \iint_{S_2} \rho(u_w - u_c)^2 dS - \iint_{S_2} p_2 dS$$

The instantaneous drag can then be then used to obtain the time-averaged drag in the control volume. The experiments were conducted for a cyclist in both upright and time-trial positions, some graphic results of the wake development process behind the cyclist have been reported in Fig.3.7. As already anticipated by (ibid.), the main contribution to the drag is offered by the momentum term and the pressure one; however, it can be seen that however the first is clearly much larger than the second one. The behavior of the two terms is in contrast; the pressure term quickly decades in space, on the other hand the momentum deficit slightly grows up. The overall behavior of the two terms leads to an approximatively constant drag inside the control volume.

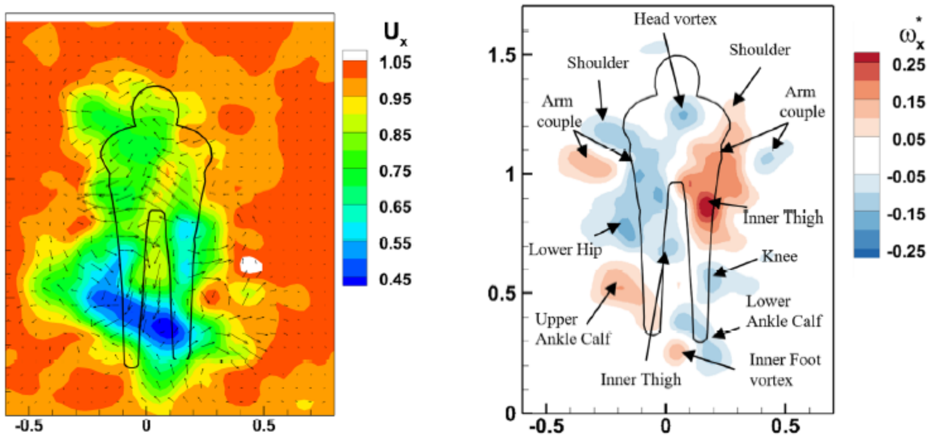

Figure 3.7: Streamwise velocity and vorticity fields in the wake of cyclist in time-trial position, reproduced from (Spoelstra, Martino Norante, et al. 2019).

The results showed by (Spoelstra, Martino Norante, et al. 2019) agree well with the literature, the main issues exposed by the authors are related to the tendency of the wake to move outside the measurement window and the time needed for the data transfer process.

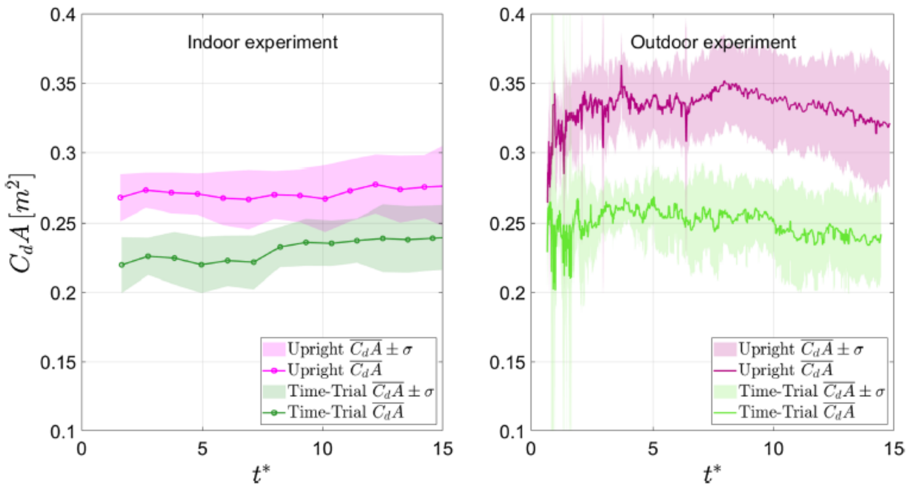

Figure 3.8: Comparison between indoor and outdoor RoF approaches results, reproduced from (Spoelstra, Martino Norante, et al. 2019)

Despite the well-behaving results, a clear divergence in terms of uncertainty has been founded between indoor and outdoor experiments. Especially in the latter, a wide uncertainty range emphasizes the non-repeatability of the experiments; this is mostly caused by the varying environmental conditions. Despite this disadvantage, the overall tendency of the curve seems to faithfully follow the indoor behavior. The comparison between the two cases can be appreciated in 3.8. The RoF approach has been also improved during recent years; examples of academic works concerning the improvement of the method are (Martino Norante 2018) and (Spoelstra, Maximilian Hirsch, et al. 2020). Nowadays, the applications of the method aren't limited to the study on a single cyclist.

Figure 3.9: RoF approach applied for the study of drafting cyclists aerodynamics, reproduced from (Mahalingesh 2020).

The RoF concept has been in fact applied to more complex cycling problems; for instance, a study on more cyclists in drafting configuration has been conducted by (Mahalingesh 2020). Some graphic results are reported in in Fig.3.9.

Figure 3.10: Ice-Skater passing through RoF laser sheet, reproduced from (TUDelft 2021).

Despite being born for the aerodynamic improvement in cycling, the RoF represents a state-of-art large-scale stereoscopic PIV approach potentially applicable in different fields. Possible applications could regard industrial measurements in the automotive field, drones flight testing and aerodynamic optimization of a wide variety of speed sports. In particular, this innovative method nowadays represents one of the few possibilities to achieve real on-site measurements for speed sports. The latest example of the RoF concept implementation concerns the aerodynamic optimization of ice-skating technique. As shown in Fig. 3.10, an Olympic-level ice-skater's drag has been estimated through the RoF approach for different skating configurations.

3.3 Lagrangian drift volume-based approaches

Due to their direct correlation to aerodynamic drag, the mechanisms lying beyond unsteady forces' generation have always been major objects of interest. A useful tool to deepen the knowledge of those mechanisms is the concept of added mass. The added mass is defined as a way of quantifying the kinetic energy added to the fluid when an accelerating object applies a work on it in a potential-flow. An example of added mass derivation has been proposed by (Crowe et al. 1998) for the study of accelerating spherical particles in multi-phase flows. The momentum balance for a particle can be expressed as:

$$m_p \frac{\partial u_p}{\partial t} = \sum F + \frac{\rho V_p}{2}\left(\frac{Du}{Dt} - \frac{\partial u_p}{\partial t}\right)$$

Where m_p,V_p and u_p are the particle's mass, volume and velocity respectively, ρ and u are the fluid's density and velocity, and finally $\sum F$ is the sum of the externals forces acting on the particle.

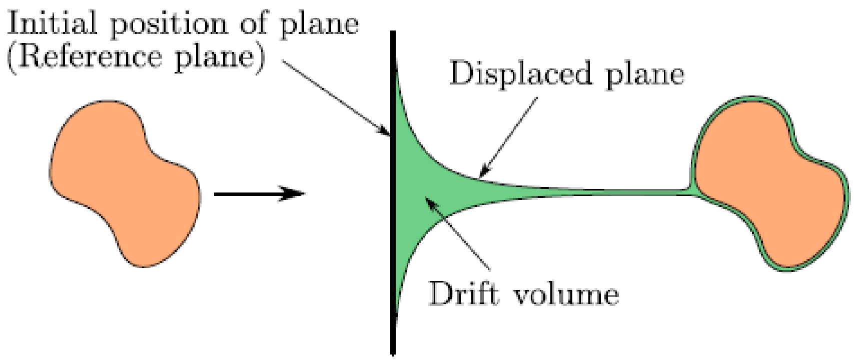

Figure 3.11: Illustraion of the drift-volume concept, reproduced from (McPhaden and Rival 2018).

Reformulating the above expression it is possible to mathematically expose the added mass phenomena:

$$\left(m_p + \frac{\rho V_p}{2}\right)\frac{\partial u_p}{\partial t} = \sum F + \frac{\rho V_p}{2}\frac{Du}{Dt}$$

It is then possible to express both the added mass and the added mass force as:

$$m_a = \rho \frac{V_p}{2}$$

$$F_{m_a} = \frac{\rho V_p}{2}\left(\frac{Du}{Dt} - \frac{\partial u_p}{\partial t}\right)$$

The particle cannot occupy the same physical space as the fluid, hence, the particle will displace it during its movement. The direct consequence is a virtual increase in the object's total mass and an increase in the total force acting on the body. As stated by (C. K. Batchelor and G. Batchelor 2000), the added mass has not to be defined but it should be discerned through an integration of the velocity's change of all the surrounding fluid. In order to calculate the added mass, (Darwin 1953) has proposed appealing idea of drift-volume. The drift volume is defined as the volume swept by a plane of Lagrangian particles crossed by a body. An illustration of the concept has been reported in Fig. 3.11.

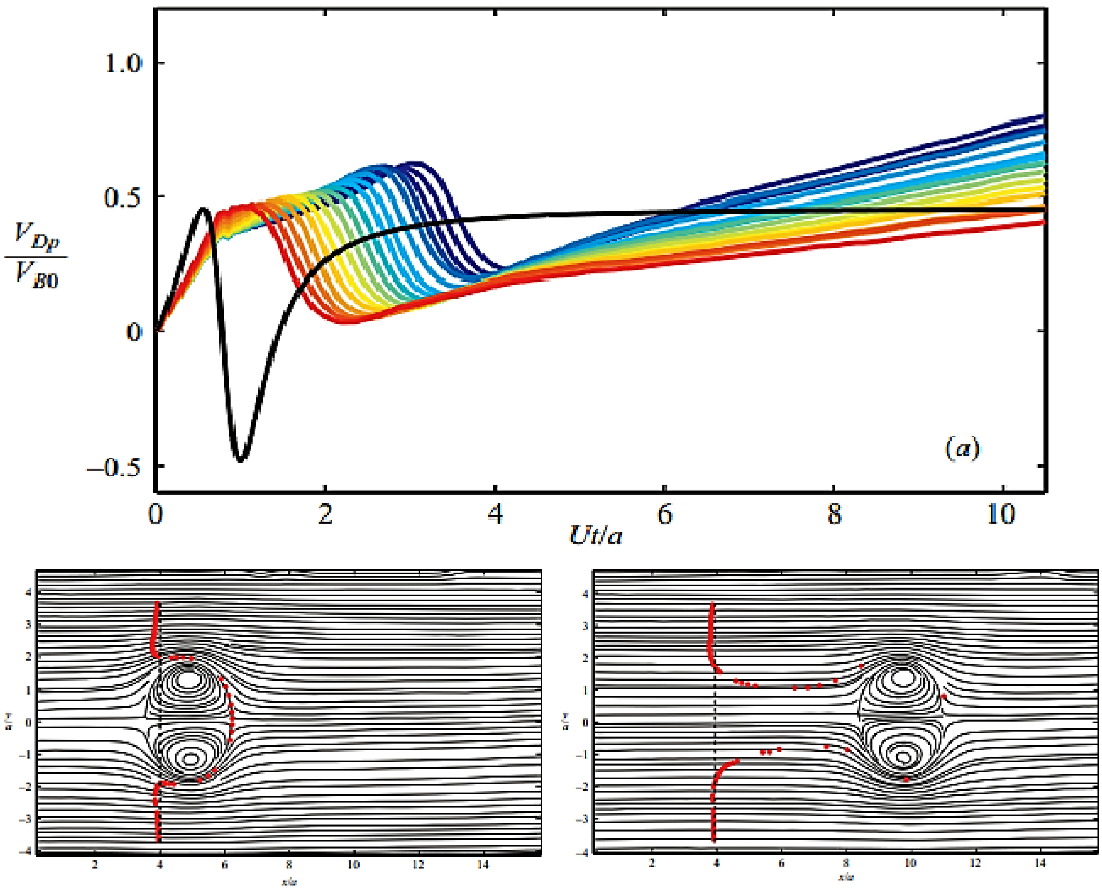

Figure 3.12: Confrontation between added mass coefficient $\frac{V_{Dp}}{V_{B0}}$ of a solid sphere in potential flow (black line) and a vortex ring added mass coefficient for different particle plane position (coloured lines)(top),Passage of a vortex ring (shown in streamlines) through a plane of virtual Lagrangian particles (bottom), reproduced from (J. O. Dabiri 2006).

Through his proposition, the author was able to demonstrate the equivalence between the drift volume and added mass associated with translating bodies. Hence, a Lagrangian technique for the calculation of added mass was developed. Furthermore, a new interpretation of the added mass as the physical mass of fluid worked upon by a translating body was provided. Many examples of the added mass-drift-volume proposition's applications can be found in the literature. The fascinating possibility of unsteady-force evaluation through that kind of simple approach has motivated the works of many others, as for example (Lighthill 1956), (Benjamin 1986) and (Eames, Belcher, and Hunt 1994). An example of the drift-volume application for real viscous flows has been presented by (J. O. Dabiri 2006). By means of DPIV measurements, the added mass coefficient of accelerating vortex rings was determined. Some results are showed in Fig.3.12. The most emphasis-deserving result in this work is that the added-mass coefficient reaches the same value of $\frac{1}{2}$ for a solid sphere translating through a potential flow. Direct application of the drift-volume approach for the determination of unsteady forces has been proposed by (McPhaden and Rival 2018). During that work, the study of translating flat plates' unsteady drag has been conducted exploiting planar PIV measurements. According to the authors' hypothesis, it is possible to neglect the surface terms and to replace the unsteady term of momentum balance equation with the added mass force:

$$D(t) = \rho \iiint_{CV} \frac{\partial u}{\partial t} dV = \frac{\partial m_a u_b}{\partial t} = \frac{\partial(\rho \Omega_D) u_b}{\partial t}$$

The previous epression leads to:

$$D(t) = m_a \frac{\partial u_b}{\partial t} + u_b \frac{\partial m_a}{\partial t} = \rho \Omega_D \frac{\partial u_b}{\partial t} + \rho u_b \frac{\partial \Omega_D}{\partial t}$$

Where m_a is the added mass affected by the body's change in velocity, u_b is the body's velocity and finally Ω_D is the drift-volume. As stated by the authors, the added mass force is in phase with the acceleration of the body. Hence, the calculation of added mass needs to be carried out with high temporal resolution. To achieve such a task, a multi-reference plane drift-volume approach was developed in order to determine the forces associated with the moving fluid . An illustration of the approach has been reported in Fig.3.13.

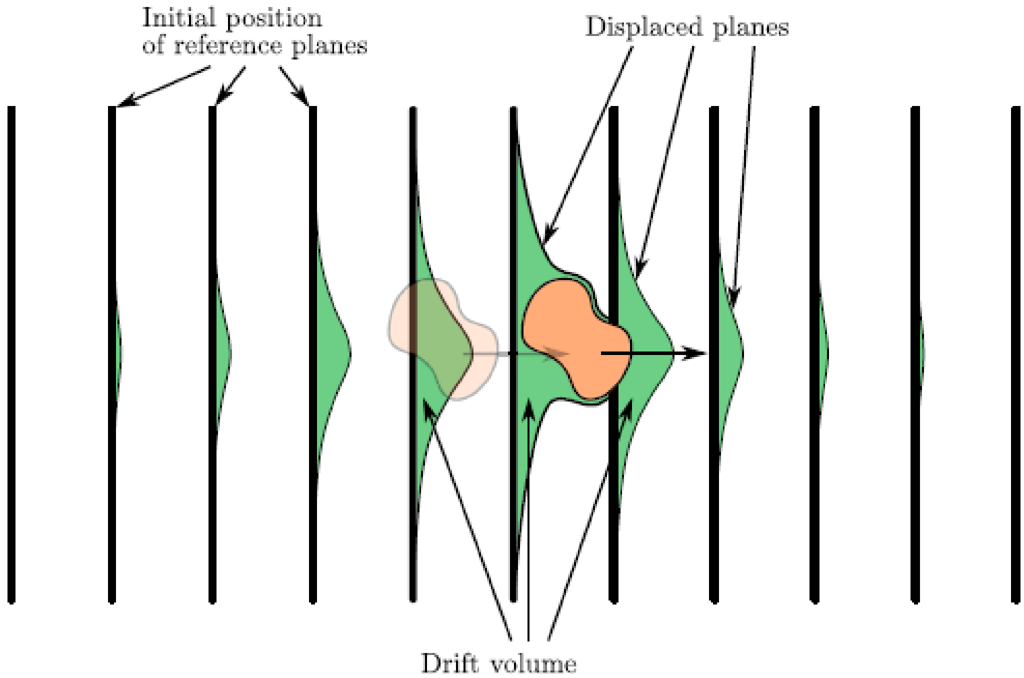

Figure 3.13: Multi-reference plane Drift-Volume approach, reproduced from (McPhaden and Rival 2018).

As already stated, the test case of the study concerned an accelerating circular flat plate. A comparison with both direct measurements and classical added mass formulation results was carried out. Furthermore, a sensitive study based on the number of reference planes was conducted to establish the correct number of planes and the correct distance between two consecutive planes. Some results are shown in Fig.3.14. The calculated force seems to follow well direct measurements until $t^* = 0.25$, which corresponds to the initial acceleration time. After the acceleration phase, the body moves at a constant speed, hence the initial assumptions lose validity. The surface contributes due to the momentum lost, the pressure deficit and the viscous stress cannot be neglected anymore.

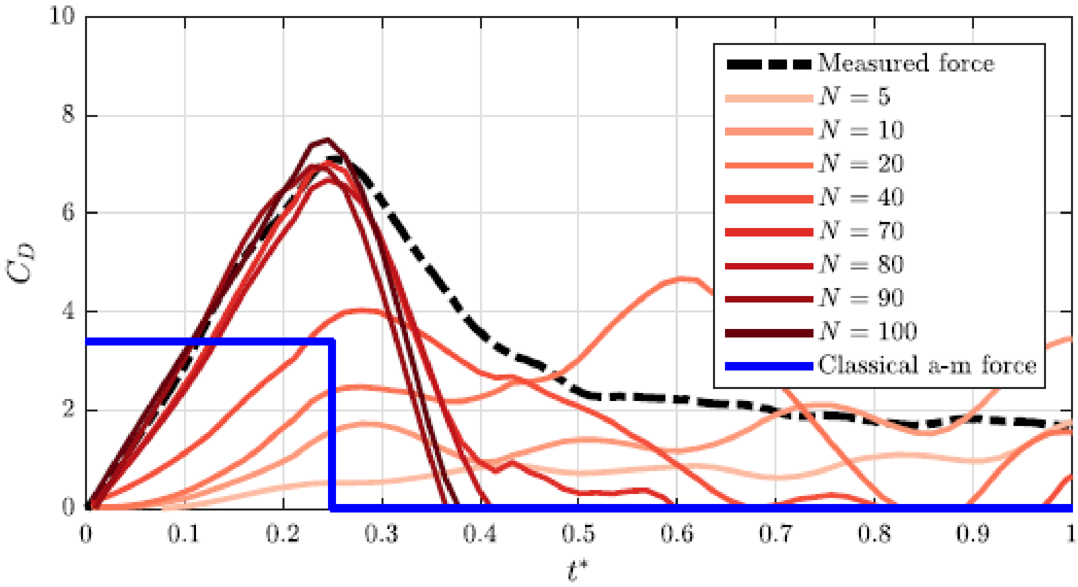

Figure 3.14: Drag coefficient varying with time for different numbers of reference planes and comparison with direct measurements and classical added mass force, reproduced from (McPhaden and Rival 2018).

In a similar fashion, (Galler, Weymouth, and Rival 2021) introduced the concept of Energized Mass. The Energized Mass concept has been developed for the study of separating flows over accelerating bodies. As stated by the authors, the definition of added mass for potential flows is not suitable for the study of viscous flows. Hence, the forces arising from the boundary layer formation and the viscous separation phenomenas, cannot be properly modelled through the mere concept of added mass. The Energized mass concept was derived from the work-energy theorem. The change in force and mass of the system is related to the temporal variation of kinetic energy; a physical interpretation of such a relationship can be found in the power exchange between the fluid surrounding the body and the body itself:

$$F_{EM}U + U(u - \frac{1}{2}U)\frac{\partial m_e}{\partial t} = \frac{1}{2}\frac{\partial (m_e U^2)}{\partial t}$$

Where F_{EM} is the energized mass force, U is the body velocity, u is the velocity at which the mass transits the system and m_e is the energized mass itself. A fluid portion energized by the passage of the body will increase system's inertia proportionally to its instantaneous kinetic energy. Considering the instant of motion, it is possible to neglect u:

$$F_{EM}U - \frac{1}{2}U^2\frac{\partial m_e}{\partial t} = \frac{1}{2}U^2\frac{\partial m_e}{\partial t} + m_e U\frac{\partial U}{\partial t}$$

The work made by the body on the fluid is then related to both the variation of fluid's kinetic energy and the total increase of the newly defined Energized mass. The total force acting on the body is then:

$$F_{EM} = m_e\frac{\partial U}{\partial t} + U\frac{\partial m_e}{\partial t}$$

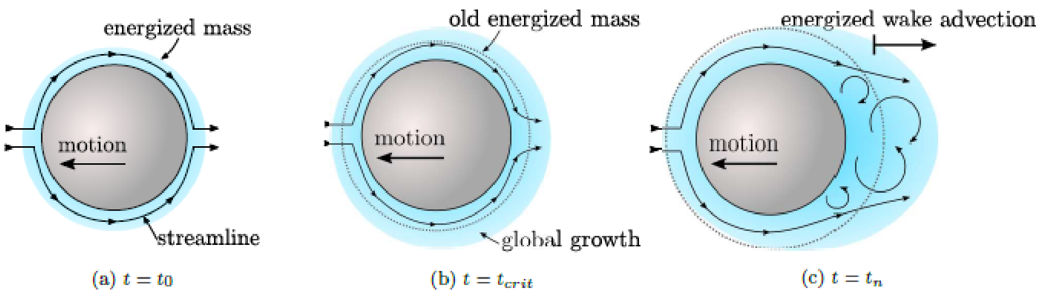

Figure 3.15: Energized mass development process for an accelerating sphere, reproduced from (Galler, Weymouth, and Rival 2021).

In the same fashion of classical added mass, the Energized mass provides the measure of an increase of the total mass of the system related to the change of the fluid's kinetic energy. A physical description of the Energized mass development mechanism has been hypothesized by the authors. Considering the case of an accelerating translating sphere, at the starting time of the motion the energized mass is restricted near the body; hence the flow can be considered potential. During the acceleration, the growing shear-layer causes a gradual increase in the energized mass total volume, although it is still uniformly distributed around the body.

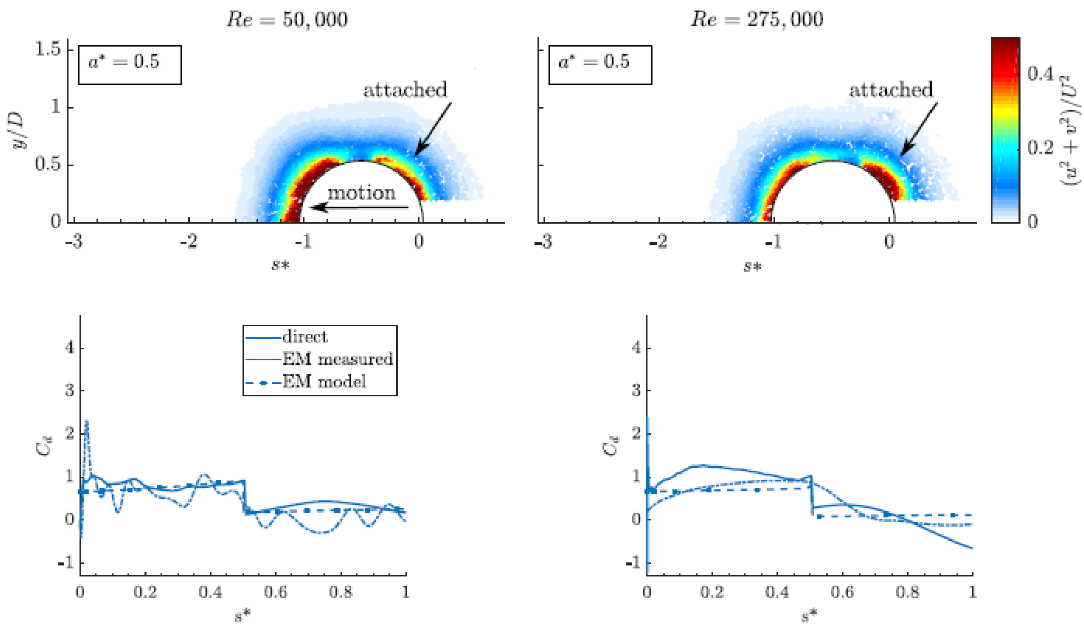

Figure 3.16: Energized mass field for $a^* = 0.5$,$Re = 5 \times 10^4$ (Top-left) and $Re = 2.75 \times 10^5$(Top-right). Comparison of drag coefficient obtained through analytical EM model,experimental EM approach and direct force measurements for $Re = 5{\times}10^4$ (Bottom-left) and $Re = 2.75{\times}10^5$(Bottom-right), reproduced from (Galler, Weymouth, and Rival 2021).

After the acceleration, the sphere will reach its final velocity, and the flow will separate from the body's surface. The separating shear-layer will eventually lead to the formation of the wake.

In those conditions, the energized mass volume will increase while stretching downstream and encompassing the whole wake. An illustration of the main process has been reported in Fig.3.15. The hypothesis about the energized mass's development suggest that its growth is mostly due to the feeding shear-layer and vortex ring formation mechanisms. Basing on the mass balance between the feeding shear-layer and the forming vortex ring, the authors developed an analytical model for the energized mass. To assess the model, planar PTV measurements on an accelerating sphere were carried out in an optical towing-tank. Some results have been reported in Fig.3.16. For $a^* < 0.5$, Energized mass fields show no dependence from both the Reynolds number and the acceleration moduli for $a^* < 0.5$. On the other hand, a strong dependence from the Reynolds number has been observed in the post-acceleration phase. The comparison with direct force measurements confirms that the shear-layer mass-flux is the main responsible for the accumulation of energized mass. The instantaneous energized mass's contribution appears to be more important in the acceleration phase. On the other hand, the rate of change of energized mass contributes more significantly in the post-accelerating phase. Major discrepancies were observed during the steady translation phase; a Reynolds number-dependency has also been observed during this phase. Most of the divergences in the steady-phase have been attributed to the moving separation line on the sphere.

3.4 Derivation of Energized Wake Area Model

Following the results of (McPhaden and Rival 2018) and (Galler, Weymouth, and Rival 2021) for accelerating bodies, a new analytical model for the drag estimation of steady-translating bodies has been developed in the current work. The energy exchange in the wake between the body and the fluid has been used to provide the basis for the new approach. As stated by (Buresti 1998), the presence of two counter-rotating vortexes in a shedding period, separated by a distance comparable with the wake-width, strongly increase the wake's total kinetic energy. Hence, the work done by the body on the flow must balance the change of the fluid's kinetic energy:

$$D\Delta x = (\frac{1}{2}m_F U_B^2 - \frac{1}{2}m_F U_0^2)$$

Where m_F is the mass of fluid, Δx is the body's displacements,U_B is the body's velocity and U_0 is the flow's initial velocity which is null in this case since considering the body to be initially firm. Expressing the energized fluid's mass as the product of the fluid density and the energized fluid's total volume:

$$D\Delta x = \frac{1}{2}\rho V_F U_B^2$$

Where V_F is the volume of energized fluid. As stated in the work of (Carmody 1964), most of the kinetic energy transferred from the body to the fluid will be stored in a near-wake's portion of fluid in proximity of the body's trailing edge. Hence, as a first assumption, it is possible to assume that the portion of energized fluid equals the volume of a cylinder of dimensions $A_w\Delta x$,where A_w is the cylinder's base. A schematic representation of the application of this concept to a flat plate normal to the flow has been reported in Fig.3.17.

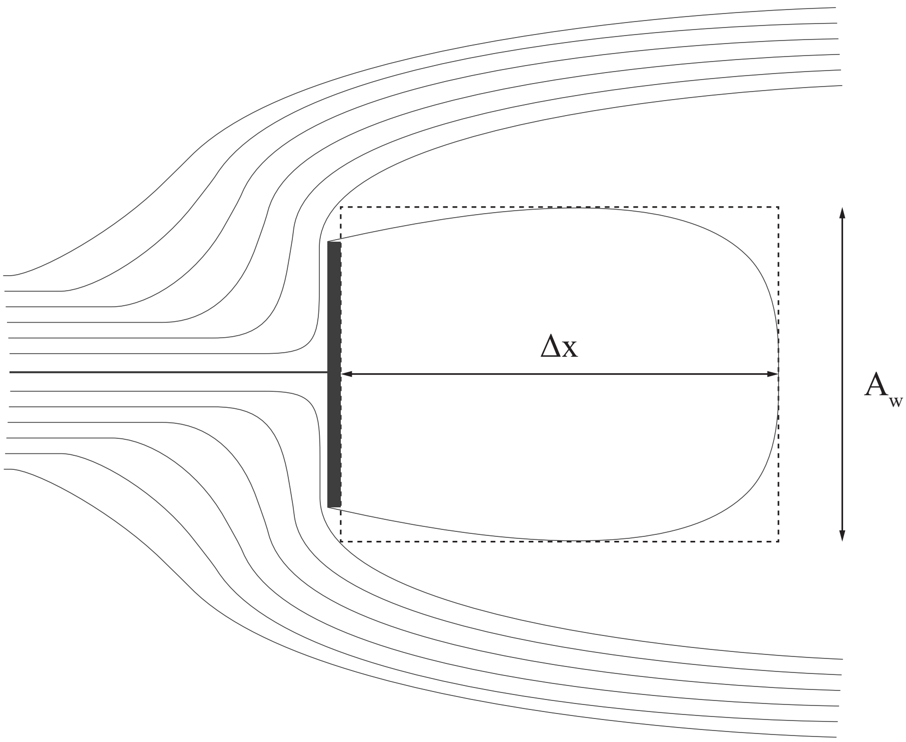

Figure 3.17: Approximation of the energized portion of the wake as a cylinder of area A_W and height Δx.

The base-area of this cylinder can then be estimated as the energized-wake area's projection on the body. The previous expression can then be reduced to:

$$D\Delta x = \frac{1}{2}\rho A_W U_B^2 \Delta x$$

Expressing the drag force in its classical formulation:

$$\frac{1}{2}\rho U_B^2 A C_D \Delta x = \frac{1}{2}\rho A_W U_B^2 \Delta x$$

Where A is the body's reference area. By simplifying both sides of the equation, a simplified expression for the drag coefficient can be achieved:

$$C_D = \frac{A_W}{A}$$

Through this expression, the drag coefficient has been directly related to the wake's size and and the concentration of kinetic energy. Further evidence of the relationship between the fluid's kinetic energy, the wake's size and aerodynamic drag, can be found in literature. According to the results of (Nedić, Ganapathisubramani, and Vassilicos 2013), the drag of bluff bodies can be varied either by changing the kinetic energy's dissipation rate or by either changing the wake's shape. The calculation of the total drag acting on the body has been thus reduced to the determination of the energized wake's projected area. To achieve such a task, a wake-contouring process needs to be carried out to identify the interested portion of the wake. After isolating the wake,it is finally possible to discern A_W. The final resulting drag coefficient is then only a function of the body geometry and its wake's projected area. The chosen wake-contouring method, as well as the individuation of A_W, will be discussed in the following chapters.

Chapter 4

Experimental Setup

In order to validate the developed analytical model, 2D2C PIV measurements have been carried out to determine the planar velocity field in the wake of different bluff bodies and a NACA-0012 airfoil. The choice of the models and their design is discussed in the first part of the following chapter, on the other hand the second part is dedicated to the description of the experimental setup utilized for the current experiment. Finally, the last part of the chapter is focused on data acquisition and pre-processing techniques exploited to retrieve high-fidelity velocity fields from raw images.

4.1 Wind tunnel

The experiments have been carried out in the "W-tunnel", a low speed and low turbulence open circuit wind tunnel situated at TU Delft high-speed laboratory HSL.

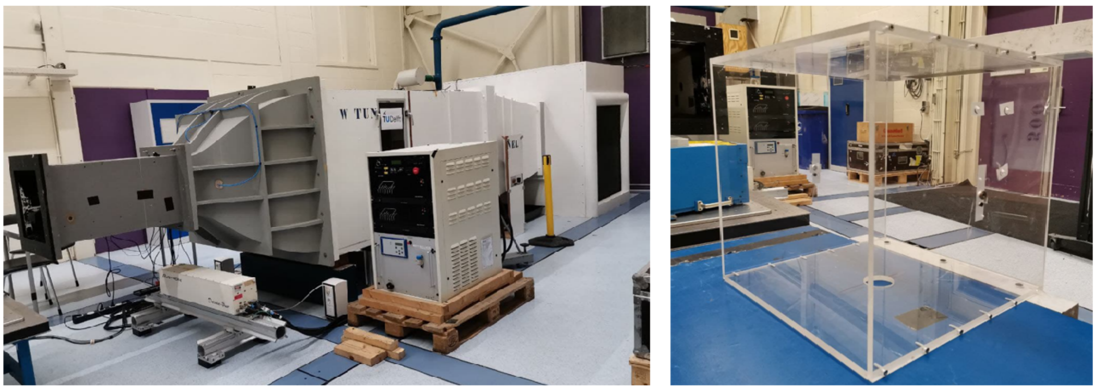

Figure 4.1: W-tunnel setup and test section.

The W-tunnel setup starts with a centrifugal fan which allows a maximum flow speed of $35m/s$, the velocity can be regulated by setting the revolutions per minute of the fan itself. In order to obtain a Reynolds numbers range between 6×10^4 and 10^5, a velocity of 18 m/s has been set. Right after the fan a diffuser and a settling chamber can be found, the latter presents multiple grid sheets necessary to achieve low turbulence levels in the order of 0.5% depending on the flow velocity. The settling chamber is followed by the contraction and a $0.4m \times 0.4m \times 0.4m$ cubic test section. The test section is a box made by plexiglass panels as shown in Fig.4.1, the plexiglass panels are meant to allow full optical access in order to grant the PIV measurements needed for the present experiment.

4.2 Test models choice and design

The test models for the current experiments consist of different bluff bodies and a NACA-0012 airfoil. The choice of the bluff bodies has been made after a literature review (Cheeseman 1976), different 2D bluff bodies presenting a wide range of drag coefficient's values at a $Re \approx 10^5$ have been then selected. The models all present the same characteristic length of 0.05 m and a span-wise length of 0.4 m; they have been designed with the help of STAR CCM+ CAD software package ad produced at the TU Delft Aerodynamic laboratory, sketches of the models with the respective drag coefficients have been reported in Fig.4.2.

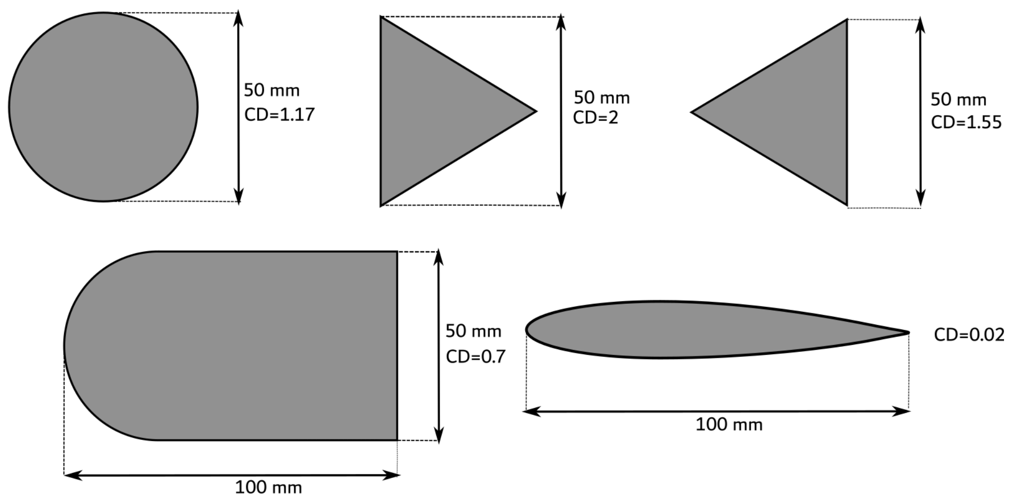

Figure 4.2: Model geometries and dimensions with respective drag coefficients for $Re \approx 10^5$, (Cheeseman 1976).

To obtain a full 2D flow the test models have been designed such that they completely span over the full width of the test section, thus preventing the formation of tip vortices. Despite the formation of tip vortices has been prevented, the formation of horseshoe vortex will take place because of the junction flow in the proximity of the sidewalls, however its effect in the measurement plane results negligibile.

4.3 Geometry modifications

In order to enlarge the range of the analyzed drag coefficients, some modifications have been made to the starting geometries. The modifications have been made in the cases of the circular and D-shape cylinders and in the case of the NACA 0012 airfoil, thus leading to a significant decrease and increase of drag coefficient for the formers and the latter respectively. In the case of the cylinders the drag reduction has been achieved by means of a passive flow-control device as zigzag strips; such device is used to trigger the boundary layer trasition from laminar to turbulent,the device is showed in Fig.4.3.

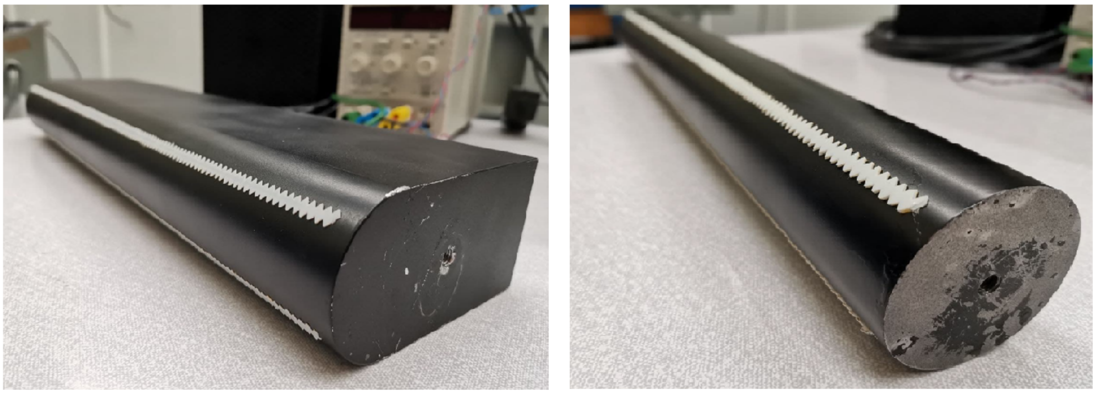

Figure 4.3: Aerodynamic zigzag strips applied on the test models.

By means of a tomographic PIV technique, (Elsinga and Westerweel 2012) observed shear-layer separating from the strip with undulating vortices, those structures have been later found to break into smaller vortical structures near the wall. Two important parameters to be accounted for are the angular position of the strips and their relative surface roughness. The strips have been placed at 45 from the leading edge, the relative surface roughness can be calculated as follows:

$$k_\epsilon = \frac{\epsilon}{D} = \frac{0.0005[m]}{0.05[m]} = 0.010$$

Where ϵ is the thickness of the strips. For the airfoil case a significantly higher drag coefficent can be obtained by simply varing its incidence,the selected configurations have been reported in Fig.4.4.Angles of 5 and 15 degrees have been chosen in order to achieve a drag increase in both stalled and not-stalled conditions. In both cases, a wider wake than the null incidence configuration is expected, thus the developed model can be tested for the cases of different-sized wakes.

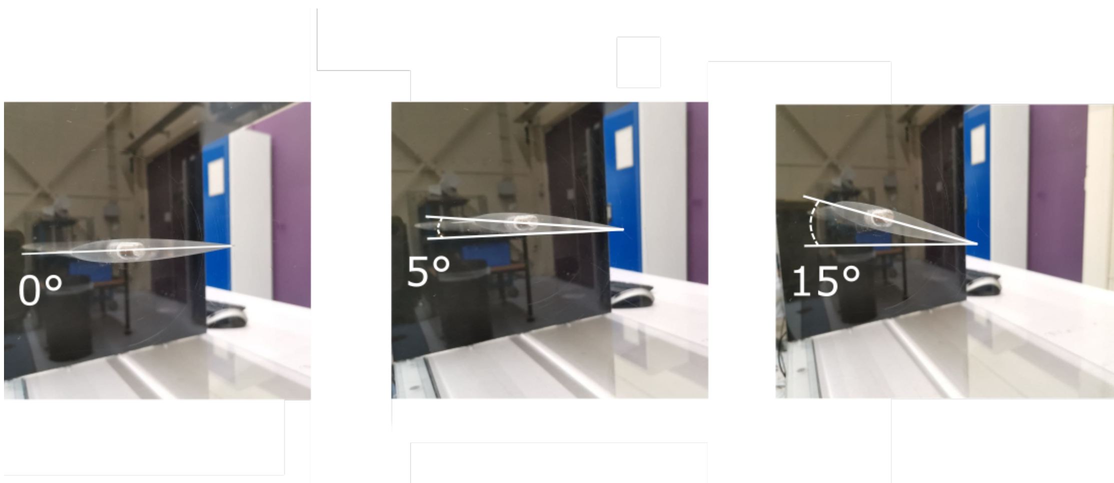

Figure 4.4: NACA-0012 airfoil configurations at different angles of attack.

4.4 PIV Setup

The PIV setup is composed by a source of illumination,an imaging system a reconding device and finally a seeder; a schematic rapresentation of the complete PIV setup is shown in Fig 4.5. The source of illumination for the experiment is a Nd:YAG double pulse Quantel *Evergreen* laser with a wavelength of 532 nm, a pulse energy of 200 mJ at a repetition rate of 15 Hz. A combination of cylindrical and spherical lenses is put right in front of the laser beam; the laser beam can thus be reshaped into a laser sheet. The final laser sheet presents a thickness of 2 mm,in order to illuminate the flow in a complete 2D section it needs to invest both the test section and the tested models at mid-span as showed in Fig.4.6. The recording task has been carried out by utilizing a LaVision's double shutter Imager sCMOS camera, such recording device presents a maximum resolution of 2560×2160 px , a pixel size of 6.5×6.5 μm^2 and a maximum sampling rate of 50 Hz. The camera has been positioned normal to the laser sheet so that the image distortion can be minimized and the wake velocity field can be acquired with higher accuracy.The chosen lens present a focal length of 35 mm, thus allowing to provide a FOV of approximatively 250×330 mm^2. The selected FOV is so that a measurement plane wide enough to satisfy the control-volume approach hypothesis can be provided. After setting the camera's parameters it has been possible to discern the Magnification factor M and the distance from the lens plane needed to achieve the desired FOV Z_0:

$$M = \frac{z_0}{Z_0} = \frac{\text{sensor size}}{\text{objective size}} = \frac{2560 \times 6.5 \times 10^{-6}}{0.330} = 0.0504$$

$$z_0 = f(1 + M) = 0.0630m$$

$$Z_0 = \frac{z_0}{M} = 1.25m$$

In order to achieve bright images with DOF a compromise has been made by setting a $f_{\#}$ of 4, thus leading to a DOF value of 0.0180 m much larger of laser sheet's thickness. Finally, fog particles of approximately $1\mu m$ have been generated using a seeder positioned next to the wind tunnel's fan. The lowest between camera's acquisition rate and laser repetition rate determines image acquisition rate's upper limit, the sampling frequency for the current experiment corresponds then to the laser's repetition rate of $15Hz$. A total number of 1000 images per test case has been acquired, thus leading to a total acquisition time of $66.66s$. As already stated in the previous sections the time between two images of an image pair depends on several factors; the most important one is the particle displacement that needs to be set in order to properly reconstruct the velocity field from the acquired images, for the current experiment a maximum displacement of 10 px has been supposed in the freestream:

$$\Delta t = \frac{\Delta x}{MU_\infty} = 89 \times 10^{-5}s$$

The global paramaters of the PIV setup have been reported in Tab.4.1.

M	$\Delta t[s]$	$f[m]$	$f_{samp}[Hz]$	$f_{\#}$	$FOV[m^2]$	$DOF[m]$	$z_0[m]$	$Z_0[m]$
0.0504	89×10^{-5}	0.035	15	4	0.270×0.330	0.0180	0.0630	1.25

Table 4.1: Parameters of the PIV setup.

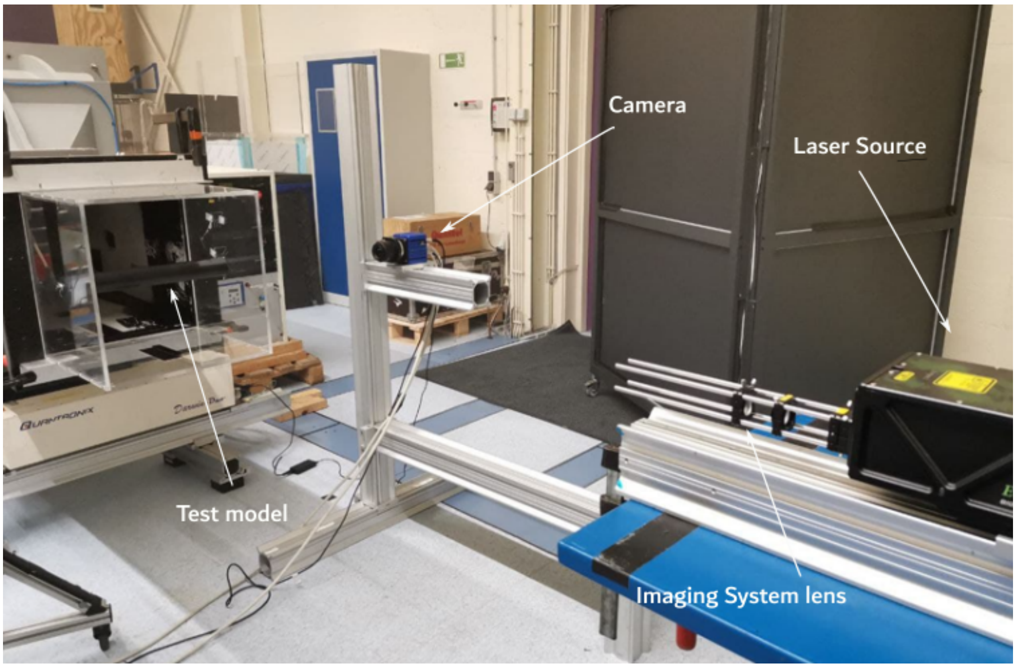

Figure 4.5: PIV setup.

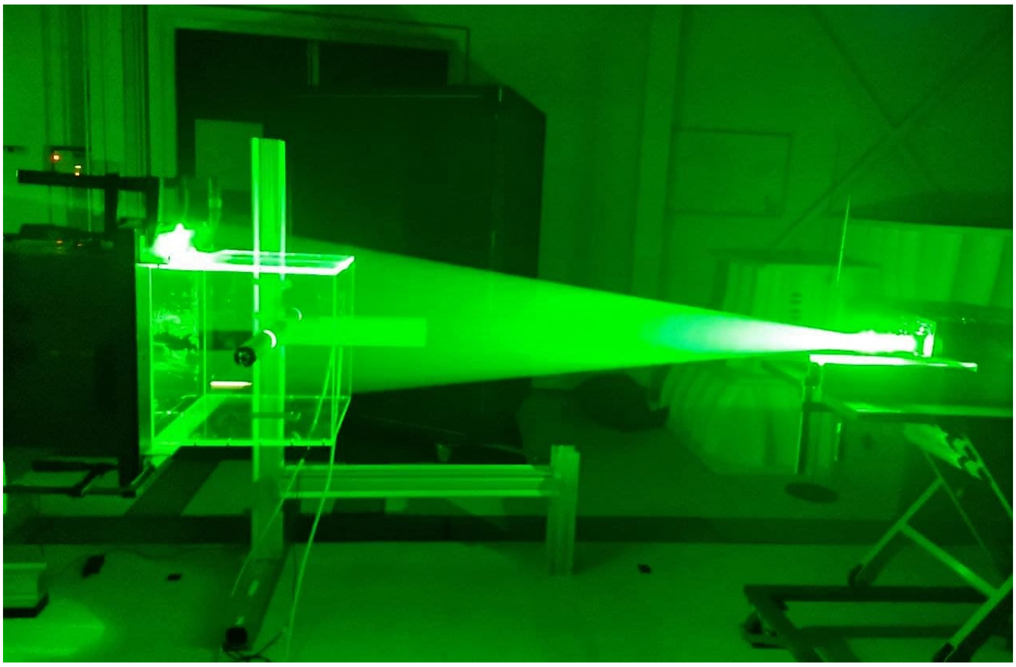

Figure 4.6: Laser sheet and imaging system.

4.5 PIV Data acquisition and processing

LaVision Davis 8 software has been used to process the PIV data acquired during the experiments, in order to obtain instantaneous velocity fields a cross-correlation analysis needs to be carried out to correlate PIV images in couples and derive particle displacement. The raw images derived from PIV are not suitable for cross-correlation analysis due to background noise, poor particle-background contrast or reflection coming from the bodies. To achieve images with higher quality, a filtering process has been carried out by applying two filters which goal is to reduce reflection and background noise and to enhance the particle-background contrast respectively. It has however to be taken into account that too strong refection could saturate the sensor's pixel, thus the particles crossing those pixels will not be imaged and resolved. The first task has been carried out by the "Subtract sliding minimum in time" filter, this filter eliminates the background noise by subtracting a certain level of intensity in a short defined time from the source image.

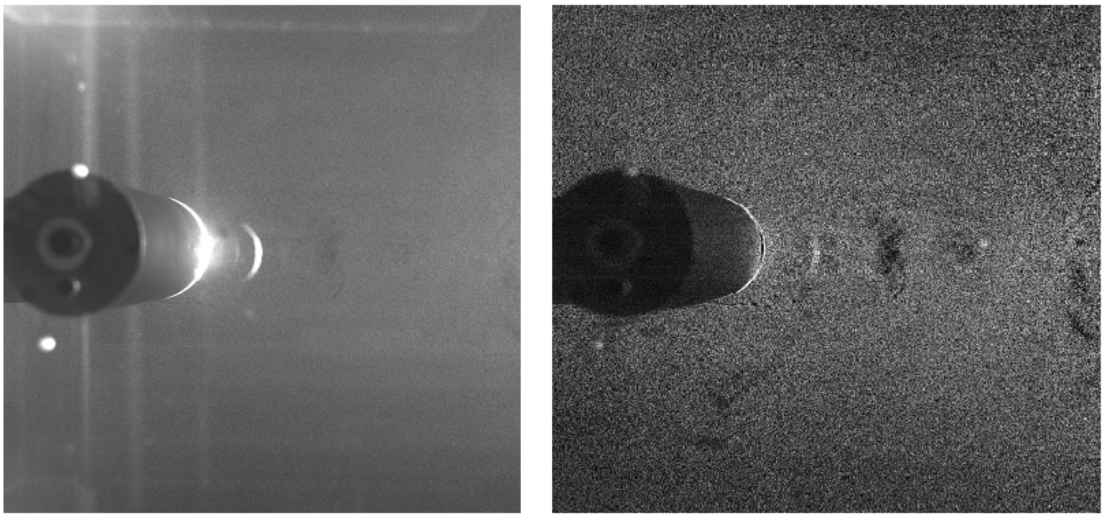

Figure 4.7: Comparison of an acquired image before and after processing filters application

The level of intensity to be subtracted highly depends on the quality of the starting images, the higher the reflection the higher the level of intensity that needs to be subtracted. Despite high levels of subtracted intensity lead to high-contrast images with less reflection, the cost of a reduced imaged seeding quantity needs to be paid. On the other hand low levels of subtracted intensity produce images with more imaged particles, but also with more reflection. A compromise needs thus to be made in order to achieve the desired quality, for the current work low-intensity levels have been generally used for the filter's application except for the case where higher levels of reflection were present. The second task has been carried out by the "Intensity normalization" filter which can improve the contrast between particles and background, a comparison between the same image first and after the filters' application has been reported in Fig.4.7. The cross-correlation analysis has been conducted using a multi-pass iterative cycle decreasing interrogation windows size at every iteration, for the current work round-shaped interrogation windows of 64×64 px with an overlap of 75% have been utilized for the first iteration and round-shaped interrogation windows of 32×32 px with an overlap of 75% have been utilized for the second one. Despite the filtering process, resulting vector fields usually contain outliers and noisy vectors that need to be eliminated in order to increase the vector fields' final accuracy. Noisy vectors are eliminated through a vector post-processing phase meanwhile the "Universal outlier detection" algorithm is exploited to eliminate outliers. Following the algorithm introduced by (Jerry Westerweel and Fulvio Scarano 2005), low-quality velocity vectors are detected in a determinate region by computing their residuals with region's median. If residuals are found to be larger than a determinate threshold, they will be eliminated from the vector field. The empty spaces will be then filled are then filled by linearly interpolating the neighboring vectors. The final vector field is obtained by fitting each vector with a second-order polynomial using a determinate number of neighboring vectors, the central vector itself is then replaced by the value of the fitted polynomial.

4.6 Freestream correction

Considering the bluff bodies models dimensions, the total blockage is approximatively 12.5%, on the other hand the airfoil model presents a much lower blockage of approximatively 3%,3.67% and 6.47% at 0,5 and 15 degrees respectively. In order to retrieve the true freestream velocity, an average of the velocity values on the top-boundary has been computed. The adimensionlized velocity values with respect to the adimensionalized distance have been reported in Fig.4.8.

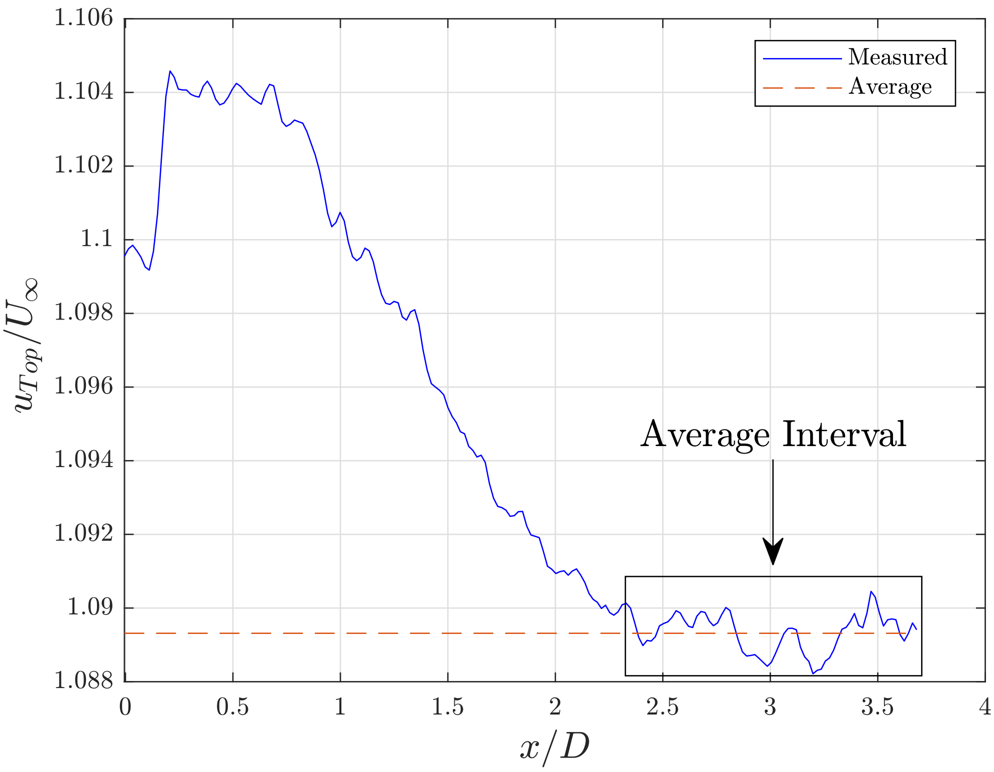

Figure 4.8: Non-dimensional velocity at the top boundary with highlighted averaging integral.

Where U_∞ is the velocity wind tunnel pre-setted freestream velocity . The average has been computed only on an interval after the acceleration zone,where the velocity reaches approximately constant values on the top-boundary. The values of the blockage ratios and the respective corrected freestream velocities have been reported in Tab 4.2. From now on the corrected freestream velocity will be referred as U_∞ and its value will be used instead of the former's one.

Geometry	Blockage Ratio	Non-dimensional freestream velocity
Circular	12.5%	1.09
Circular + Zig Zag Strips	12.5%	1.09
Triangle	12.5%	1.09
Reverse Triangle	12.5%	1.13
D-Shape	12.5%	1.07
D-Shape +Zig Zag Strips	12.5%	1.06
NACA-0012 (0°)	3.2%	1.16
NACA-0012 (5°)	3.7%	1.17
NACA-0012 (15°)	6.5%	1.2

Table 4.2: Blockage ratios and corrected non-dimensionalized freestream velocities for all the study cases.

Chapter 5

Data Reduction techniques

In the first part of the present chapter, the main data reduction techniques and the post-processing approaches are reported. Time-averaged velocity fields have been computed from the instantaneous ones by means of a Reynolds decomposition. Mean fluid dynamic quantities as pressure, turbulent kinetic energy and streamlines have been retrieved from the mean velocity field. By means of such knowledge, drag computation using both the newly-developed EWA model and the renowned MCV approach has been carried out. When reconstructing other quantities from the mean velocity field, uncertainties already present in the latter will propagate; hence, the second part of the chapter is dedicated to the uncertainty analysis of mean drag and its related quantities.

5.1 Mean velocity field computation

Knowledge of time-averaged velocity field is needed in order to calculate mean drag, hence averaging of instantaneous velocity fields is performed. Reynolds decomposition has been applied to the istantanuous velocity fields retrived from PIV measurements:

$$u = \overline{u} + u' \Rightarrow \begin{cases} \text{Time avaraged velocity } : \overline{u} = \frac{1}{N}\sum_{i=1}^{N} u_i \\ \text{Fluctuatig velocity} : u' = u - \overline{u} \end{cases}$$

Where N is the number of instantaneous velocity fields u_i acquired over time. In order to achieve an accurate averaging, it has to be taken into account that some samples might present unphysical behavior and noisy regions. The main reason could be attribued to either insufficient or even non-uniform seeding particles; another reasonable motivation could be linked to a strong laser reflection.

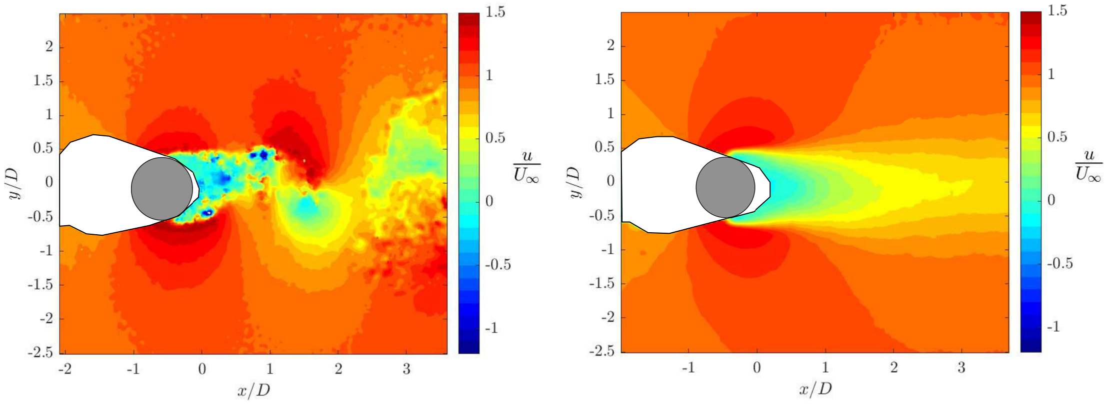

(a) Istantaneous velocity field

(b) Average velocity field

Figure 5.1: Comparison of istantaneous and average velocity fields for the cylinder case.

To take care of those problematics, some biased samples have been excluded from the averaging process; only the vectors whose values of standard deviation lie in an interval of ± 3 standard deviation have been used for the average operation. A comparison of time-averaged and instantaneous velocity fields for the cylinder case has been reported in Fig.5.1,it can be noticed that the symmetrical flow oscillations lead to symmetrical mean flow-field.

5.2 Time-avareged Pressure field reconsruction

In order to retrieve the pressure field from PIV measurements, the Poisson Pressure Equation (PPE) needs to be numerically solved. As showed in the work of (BW Van Oudheusden 2013), the Poisson equation FOR A 2D equation can be expressed as:

$$\frac{\partial^2 p}{\partial x^2} + \frac{\partial^2 p}{\partial y^2} = -\rho \left(\left(\frac{\partial u}{\partial x} \right)^2 + \left(\frac{\partial v}{\partial y} \right)^2 + 2 \left(\frac{\partial u}{\partial y} \frac{\partial v}{\partial x} \right) \right)$$

For the present work time-averaged pressure field is requested, hence the final expression of the PPE is obtained by averaging the velocity field:

$$\frac{\partial^2 \overline{p}}{\partial x^2} + \frac{\partial^2 \overline{p}}{\partial y^2} = -\rho \left(\left(\frac{\partial \overline{u}}{\partial x} \right)^2 + \left(\frac{\partial \overline{v}}{\partial y} \right)^2 + 2 \left(\frac{\partial \overline{u}}{\partial y} \frac{\partial \overline{v}}{\partial x} \right) + \left(\frac{\partial^2 \overline{u'u'}}{\partial x^2} \right) + \left(\frac{\partial^2 \overline{v'v'}}{\partial y^2} \right) + 2 \left(\frac{\partial^2 \overline{u'v'}}{\partial x \partial y} \right) \right)$$

Mean velocity gradients are the major contributor to the pressure gradients, however, fluctuating velocity also play a large role in the computation of bluff bodies' wake's pressure field. The previous expression is an elliptical partial differential equation, thus the solution does not present preferred information propagation's paths. The solution depends upon the immediately neighboring points in every point of the domain, hence the pressure field cannot present discontinuities. The discretization of pressure's second-order derivatives has been obtained by means of a second-order center finite-difference scheme; a 5-point computational molecule has been utilized. The right-hand side of the Poisson equation numerically represents the source term; it can be seen that all the quantities composing those terms are retrievable from PIV data. Using first-order difference scheme for the first derivatives and second-order central scheme for the second derivatives it is possible to obtain:

$$\frac{\partial \overline{u}}{\partial x} = \frac{\overline{u}_{i+1,j} - \overline{u}_{i-1}, j}{2\Delta x}$$

$$\frac{\partial \overline{v}}{\partial x} = \frac{\overline{v}_{i,j+1} - \overline{v}_{i,j-1}}{2\Delta x}$$

$$\frac{\partial \overline{u}}{\partial y} = \frac{\overline{u}_{i+1,j} - \overline{u}_{i-1,j}}{2\Delta y}$$

$$\frac{\partial \overline{v}}{\partial y} = \frac{\overline{v}_{i,j+1} - \overline{v}_{i,j-1}}{2\Delta y}$$

$$\frac{\partial^2 \overline{u'u'}}{\partial x^2} = \frac{\overline{u'u'}_{i+1,j} - 2\overline{u'u'}_{i,j} + \overline{u'u'}_{i-1,j}}{\Delta x^2}$$

$$\frac{\partial^2 \overline{v'v'}}{\partial y^2} = \frac{\overline{v'v'}_{i,j+1} - 2\overline{v'v'}_{i,j} + \overline{v'v'}_{i,j-1}}{\Delta y^2}$$

Being the domain composed of four boundaries, four boundary conditions are needed. A no-slip condition should also be imposed on the points composing the body surface. For the current work's purposes, the pressure field is needed only downstream the body. As shown in Fig.5.6, only four mixed Dirichlet-Neumann Boundary conditions have been applied.

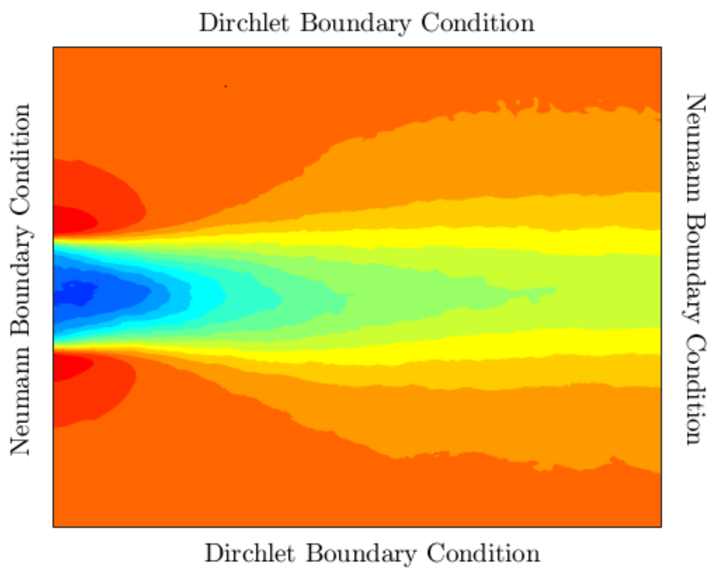

Figure 5.2: Velocity field with boundary conditions for the circular body case.

At the top and bottom sides of the domain, the flow is unaffected by the presence of the model, hence Dirichlet boundary condition is used to assign the value retrieved from Bernoulli's equation:

$$p_{Bernoulli} = p_\infty + \frac{1}{2}\rho(u_\infty^2 - u^2)$$

Where p_∞ and u_∞ are the free stream pressure and velocity respectively. On the other hand, the left and the right boundaries deal with the separated turbulent flow. Strong velocity gradients are present, hence the implementation of Neumann conditions has been chosen. The pressure derivatives are calcuated by Reynolds-averaging the x-momentum Navier-Stokes equation after neglecting the viscous terms:

$$\frac{\partial \overline{p}}{\partial x} = -\rho \left(\overline{u} \left(\frac{\partial \overline{u}}{\partial x} \right) + \overline{v} \left(\frac{\partial \overline{u}}{\partial y} \right) + \left(\frac{\partial \overline{u'u'}}{\partial x} \right) + \left(\frac{\partial \overline{u'v'}}{\partial y} \right) \right)$$

$$\frac{\partial \overline{p}}{\partial y} = -\rho \left(\overline{u} \left(\frac{\partial \overline{v}}{\partial x} \right) + \overline{v} \left(\frac{\partial \overline{v}}{\partial y} \right) + \left(\frac{\partial \overline{u'v'}}{\partial x} \right) + \left(\frac{\partial \overline{v'v'}}{\partial y} \right) \right)$$

After discretizing the main variables and setting the boundary conditions, the PPE is reduced to a linear system. A schematization of the system structure has been reported in Fig. 5.3.

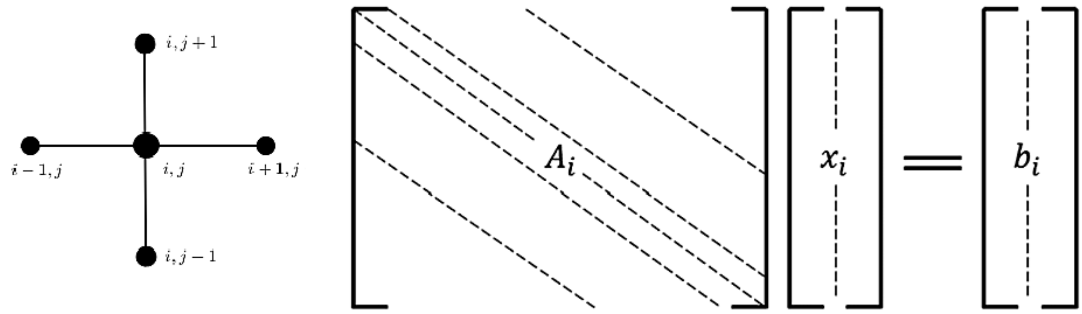

Figure 5.3: Computational molecule of a typical 2nd-order centrate scheme (Left), schematization of the system of linear equations derivng from the second-order centrate-finite-difference scheme, reproduced from (Turkoz and Celik 2015) (Right).

Where A is the penta-diagonal coefficient matrix with −4 on the main diagonal and 1 on the non-zero main diagonals,x is the pressure solution vector and b is the source term. For non-boundary rows,the generic equation will be:

$$f_{i-1,j} + f_{i+1,j} + f_{i,j+1} + f_{i,j-1} - 4f_{i,j} = b_i$$

Finally,the pressure field retrivied from PIV measurements can been adimensionalized as:

$$C_P = \frac{p - p_\infty}{\frac{1}{2}\rho U_\infty^2}$$

The classical non-dimensional pressure coefficient expression has been chosen to provide a quantification of the pressure loss with respect to the freestream pressure.

5.3 Streamlines

Important flow characteristics are streamlines. According to its definition, a streamline is a line instantaneously tangent to the flow velocity at any point. Streamlines cannot intersect at the same instant in time, since a fluid particle cannot have two different velocities at the same point in space. Streamlines for the circular body case have been reported in Fig.5.4

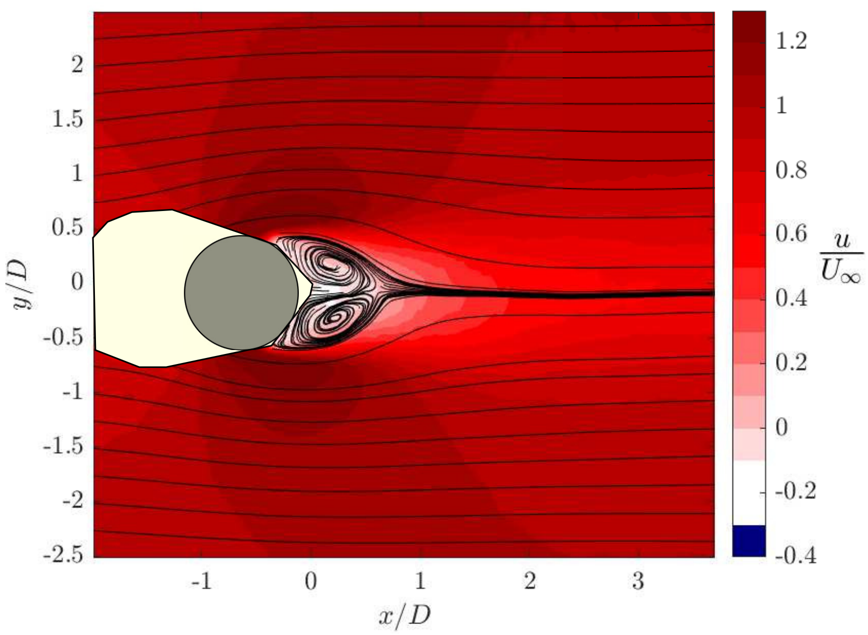

Figure 5.4: Streamlines plot with velocity contour plot in background for the circular body case.

In most of the cases,streamlines are useful since they can provide the effective direction of the wake-flow. As a consequence, the study of a determinate quantity by means of the streamlines is not limitated to its magintude.

5.4 Turbulent kinetic energy.

Turbulence kinetic energy (TKE) is the energy content of eddies in turbulent flows, it can be calculated as the sum of the velocity's component variances:

$$TKE = \frac{1}{2}(\overline{u'^2} + \overline{v'^2} + \overline{w'^2})$$

When flows become turbulent, transport mechanisms like diffusion got much stronger. As a consequence of the turbulent diffusion, the fluid dynamic quantities tends to be smoother.

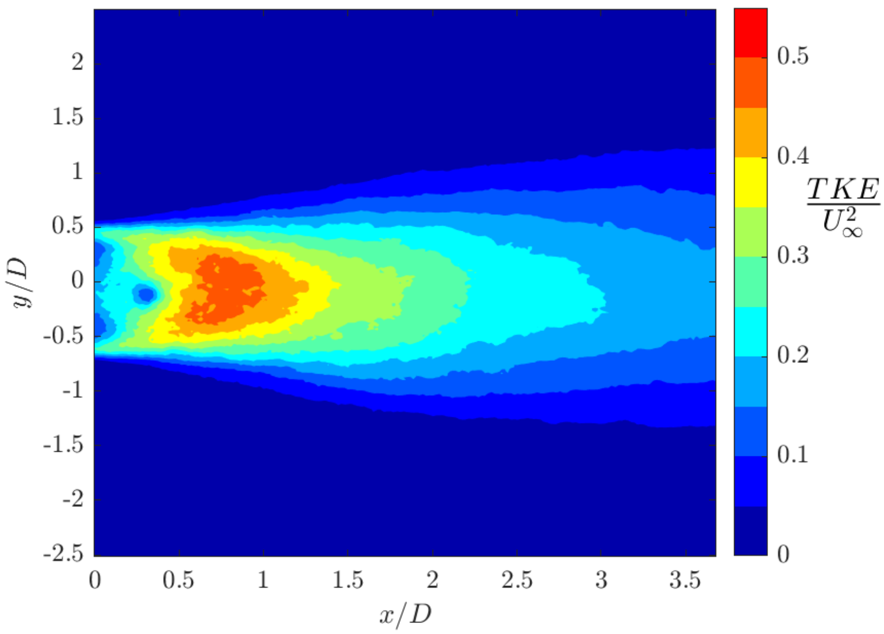

Figure 5.5: Non-dimensional TKE contour plot for the circular body case.

The increase of the diffusion is mostly due the presence of eddies, whose movements enhance the flow's transportation mechanisms. The TKE field for the circular body case has been reported in Fig. 5.5. High turbulent fluctuations lead to high turbulent kinetic energy values. Hence, concentration of turbulent kinetic energy can be found in the zones affected by velocity oscillation.

5.5 Drag computation through EWA approach

The analytical model developed in the current work aims to estimate the drag as a mere function of the body and the wake's geometrical characteristics. The drag coefficient has been analytically discerned as the ratio between the energized wake's area projected onto the body A_W , and the body's reference area A:

$$C_D = \frac{A_W}{A}$$

Where the reference-area A corresponds to the body reference length D for a two-dimensional case. Before estimating the parameter A_W, the wake itself needs to be identified through a wake-contouring process. The wake-contouring has been carried out by isolating portions of the wake presenting a velocity lower than a chosen cut-off velocity. As already stated, a cut-off velocity equal to half of the free stream velocity has been selected. However, a range of cut-off velocities going from $0.5U_\infty$ to $0.9U_\infty$ has been analyzed to understand the sensitivity of the model from such a parameter. Due to the limitations in the spatial resolution, the narrower wakes of the airfoil at 0 and 5 degrees of incidence have not been completely resolved. Hence, a range varying from $0.75U_\infty$ and $0.95U_\infty$ has been selected for such cases. On the other hand, the energized-wake area has been individuated by projecting the wake onto the body's trailing edge; hence, only salient information on the wake after the trailing edge are needed for the purposes of the current work. Hence, the wake-isolation process has been simplified by cutting the flow-field field before the trailing edge. Examples of the resulting velocity field after the contouring-processes have been reported in Fig.5.6.

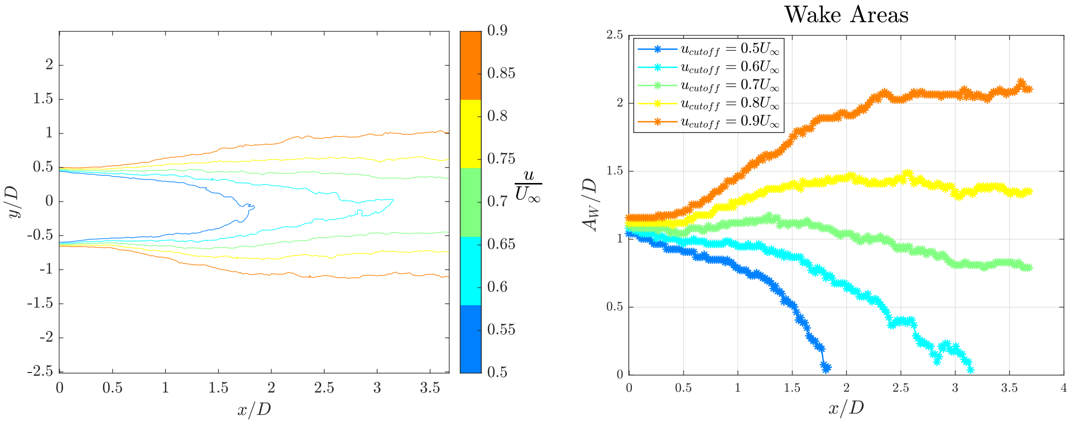

(a) (b)

Figure 5.6: Velocity contour lines corresponding with the cut-off velocities (a), Wake areas corresponding to the chosen u_{cutoff} range (b).

After the contour process, the areas have been calculated by numerically integrating the distance between two edges of the wake in every station:

$$\frac{A_w}{D} = \int_a^b d\left(\frac{y}{D}\right)$$

Where a and b are the vertical edges of the wake. Mostly due to the reflection present on the body, the trailing edge of the body does not correspond with the actual one. Hence, a linear interpolation of the wake's areas on the actual trailing edge has been carried out to estimate the real value of A_W. As shown in the picture, the calculated wake's areas don't show a constant-rate behavior in space. Hence, only the first linear region of the contoured wake has been interpolated to achieve higher accuracy.

5.6 Drag computation through MCV approach

Computing the time-averaged drag through Momentum Control Volume (MCV) approach requires the knowledge of Momentum, Pressure and Reynolds stress contributes. Being the data two-dimensional, it is possible to express time averaged drag as follow:

$$\overline{D} = \int_{-\infty}^{\infty} \rho\overline{u}(U_\infty - \overline{u})dy + \int_{-\infty}^{\infty} (p_\infty - \overline{p})dy + \int_{-\infty}^{\infty} (-\rho\overline{u'u'})dy$$

Hence, knowledge of the Reynolds stress term in the streamwise direction is needed. In agreement with (Andrea Sciacchitano and Wieneke 2016), such a term has been can be expressed as the variance of the streamwise velocity field:

$$\overline{u'u'} = \frac{1}{N-1}\sum_{i=1}^{N}(u_i - \overline{u})^2$$

The Reynolds stress terms emerge from Reynolds averaging of the non-linear term in the Navier-Stokes equations, physically representing the mean momentum rate transfer due to turbulent fluctuations.

5.7 Uncertainity in drag computation

PIV measurements are affected by a certain degree of uncertainty. Instantaneous velocity fields ' uncertainty is mostly due to the correlation of the vector components; on the other hand, statistical quantities are affected by the finite number of samples. According to (Andrea Sciacchitano 2014), the uncertainties already present in the velocity field propagate in the derived quantities, e.g. pressure and Reynolds stresses. Hence, the drag computed through the momentum control volume approach will be affected by a certain grade of uncertainty. According to (Andrea Sciacchitano and Wieneke 2016), the latter can be calculated by means of the linear uncertainity propagation formula:

$$U_{\overline{D}} = \sqrt{\left(\frac{\partial \overline{D}}{\partial \overline{u}}\right)^2 U_{\overline{u}}^2 + \left(\frac{\partial \overline{D}}{\partial \overline{p}}\right)^2 U_{\overline{p}}^2 + \left(\frac{\partial \overline{D}}{\partial \overline{u'u'}}\right)^2 U_{\overline{u'u'}}^2}$$

As shown in the work of (Koradiya 2018), the three derivatives can be computed by differentiating the mean drag with respect to the interested variables:

$$\frac{\partial \overline{D}}{\partial \overline{u}} = \rho \int_{-\infty}^{\infty} (u_\infty - 2\overline{u}) dy$$

$$\frac{\partial \overline{D}}{\partial \overline{p}} = \int_{-\infty}^{\infty} dy$$

$$\frac{\partial \overline{D}}{\partial \overline{u'u'}} = -\rho \int_{-\infty}^{\infty} dy$$

Both mean pressure and the Reynolds stress contributions depend only on the normal-to-flow distance over which deficit integrals are taken. On the other hand, the velocity derivative depends on the mean-velocity value; the higher the latter, the lower the uncertainty. Velocity measurements will assume a Gaussian distribution if the number of samples is high enough. The uncertainty related to the mean velocity can then be expressed as its standard deviation divided by the number of samples:

$$U_{\overline{u}} = \frac{\sigma_{\overline{u}}}{\sqrt{N}}$$

Being directly proportional to the standard deviation, the uncertainty field will show higher values in regions more affected by velocity fluctuations. A contour plot of the uncertainity of the streamwise velocity component for the circular body has been reported in Fig.5.7.

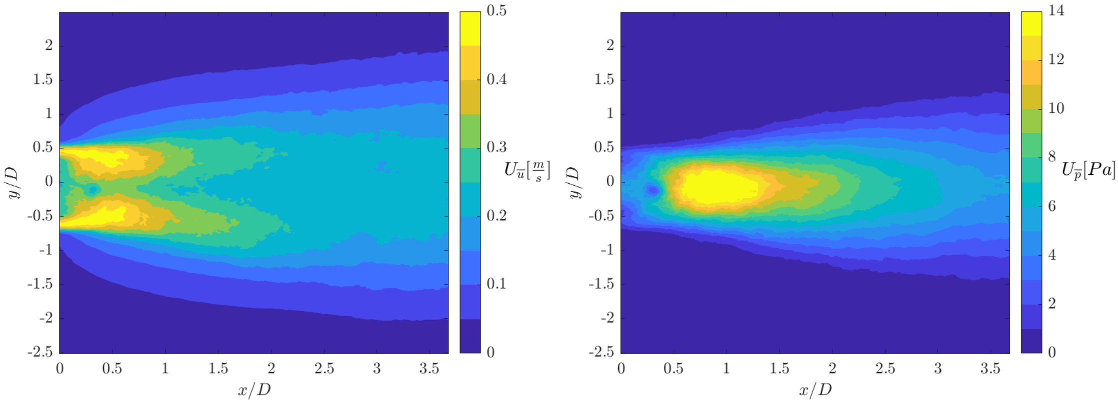

(a)

(b)

Figure 5.7: Contour-plot of the uncertainty of the streamwise velocity component $U_{\overline{u}}$ for the circular body(a), Contour-plot of the pressure uncertainty $U_{\overline{p}}$ for the circular body (b)

It can be seen that the zones most affected by the uncertainty are the two symmetric shear layers springing from the body. In those zones, a maximum uncertainty of $0.5\frac{m}{s}$ is reached. The uncertainty then gradually decreases moving downstream, reaching values of approximately $0.3\frac{m}{s}$. The most unaffected zone is clearly the freestream which presents almost null uncertainty. In agreement to (Pattnaik 2017), mean pressure uncertainties are computable by applying the linear-uncertainty-propagation formula to the terms of the Poisson equation:

$$U_{\overline{p}} = \frac{\rho \Delta x}{\sqrt{12}} \sqrt{\left[2U_{\overline{V}}\left(\left(\frac{\partial \overline{u}}{\partial x}\right)^2 + \left(\frac{\partial \overline{u}}{\partial y}\right)^2 + \left(\frac{\partial \overline{v}}{\partial x}\right)^2 + \left(\frac{\partial \overline{v}}{\partial y}\right)^2\right)\right] + \left[\frac{12U^2_{\overline{v'v'}} + U^2_{\overline{u'v'}}}{\Delta x^2}\right]}$$

Where $\overline{V}$ is the mean velocity field and v' are the velocity fluctuations normal to the flow. The contour plot of pressure uncertainty has been reported in Fig. 5.7 . Major uncertainties in pressure have been found in a central region of the wake extending approximatively from $0.5x/D$ and $2x/D$. The highest peak of pressure uncertainty is about $14Pa$ in that zone. Out of this region, pressure uncertainty rapidly decreases. The lowest reached values are between $2Pa$ and $6Pa$ in the rest of the wake and approximatively null in the freestream. It needs to be taken into account that this method involves the assumption that uncertainties in all the velocity components are equal to $U_{\overline{V}}$. Furthermore, mean velocity components are assumed to be uncorrelated among them. Finally, the uncertainty of Reynolds normal stress can be computed. As stated by (Andrea Sciacchitano and Wieneke 2016), the uncertainty of Reynold stresses takes account for both measurement's uncertainties and uncertainties due to the spurious fluctuations:

$$U_{\overline{u'u'}} = \sigma_u^2 \sqrt{\frac{2}{N-1}} \simeq \overline{u'u'}\sqrt{\frac{2}{N}}$$

The uncertainty due to spurious fluctuations can be neglected if the velocity fluctuations are larger than the measurement error. Hence, the previous expression results to be accurate enough for the present work. Being directly dependent from $\sigma_{\overline{u}}$, a similar behaviour to $U_{\overline{u}}$ is expected. Reynolds normal stress uncertainty reaches peaks of $7\frac{m^2}{s^2}$ in the free shear-layers, then it rapidly decreases to low values in the far-wake and the freestream.

Chapter 6

Results and Discussion

The following chapter is dedicated to the presentation and the analysis of the current work's main results. In the first part of the chapter, the flow's main topologies will be reported and discussed. To facilitate the exposition, from now on the tested bodies will be referred to as shown in Tab. 6.11. The voice "Triangle" is referred to the triangular body with the vertex facing the flow, while the "Reverse Triangle" one refers to the triangular body for which the flat edge is the one facing the flow. On the other hand, the second part of the chapter focuses on drag quantification; this part aims to expose the results of the new Energized Wake Area (EWA) approach and to assess its sensitivity from the cut-off velocity parameter. Finally, the Momentum Control Volume (MCV) approach has been used as a reference in order to validate the results obtained through the EWA model.

6.1 Bluff bodies flow's topologies

6.1.1 Velocity fields

Typical bluff bodies' mean-velocity fields exhibit some common features; early separation, large-expanding wakes, velocity-loss and pressure-deficit zones in the near wake are few but salient examples. Despite the similarities, the differences in the wake's structure between different bluff bodies are often linked to the difference in drag. The bluff bodies' mean-velocity fields have been reported in Fig.6.1. Symmetrical flow oscillations can be observed for all of the analyzed cases; hence, the mean-velocity fields are all symmetric. The triangular bodies seem to qualitatively present the widest wake regions. The strong adverse pressure gradient on the sharp edges leads the flow to a separation; hence, a large recirculation zone behind the trailing edge is generated. The circular bodies follow the triangular ones in the wake-width ranking. The presence of Zig-Zag strips makes the boundary layer experience turbulent transition. Turbulent boundary layers are thicker and more energized, so they better contrast adverse pressure gradients and delay the separation. Moving to the D-Shape bodies, clear differences from the other ones are observed. Both the D and the DZZS present the narrowest wake among all of the analyzed cases. As observed by (Parezanović and Cadot 2012), this kind of elongated bodies induces separation-reattachment mechanisms, which lead the flow to experience a double separation. The boundary layer first experiences a laminar separation in the first part of the body. After the separation, the detached boundary layer becomes turbulent due to Kelvin-Helmholtz instability; then it re-attaches to the rear-flat part of the body and finally separates on the sharp edges of the trailing edges.

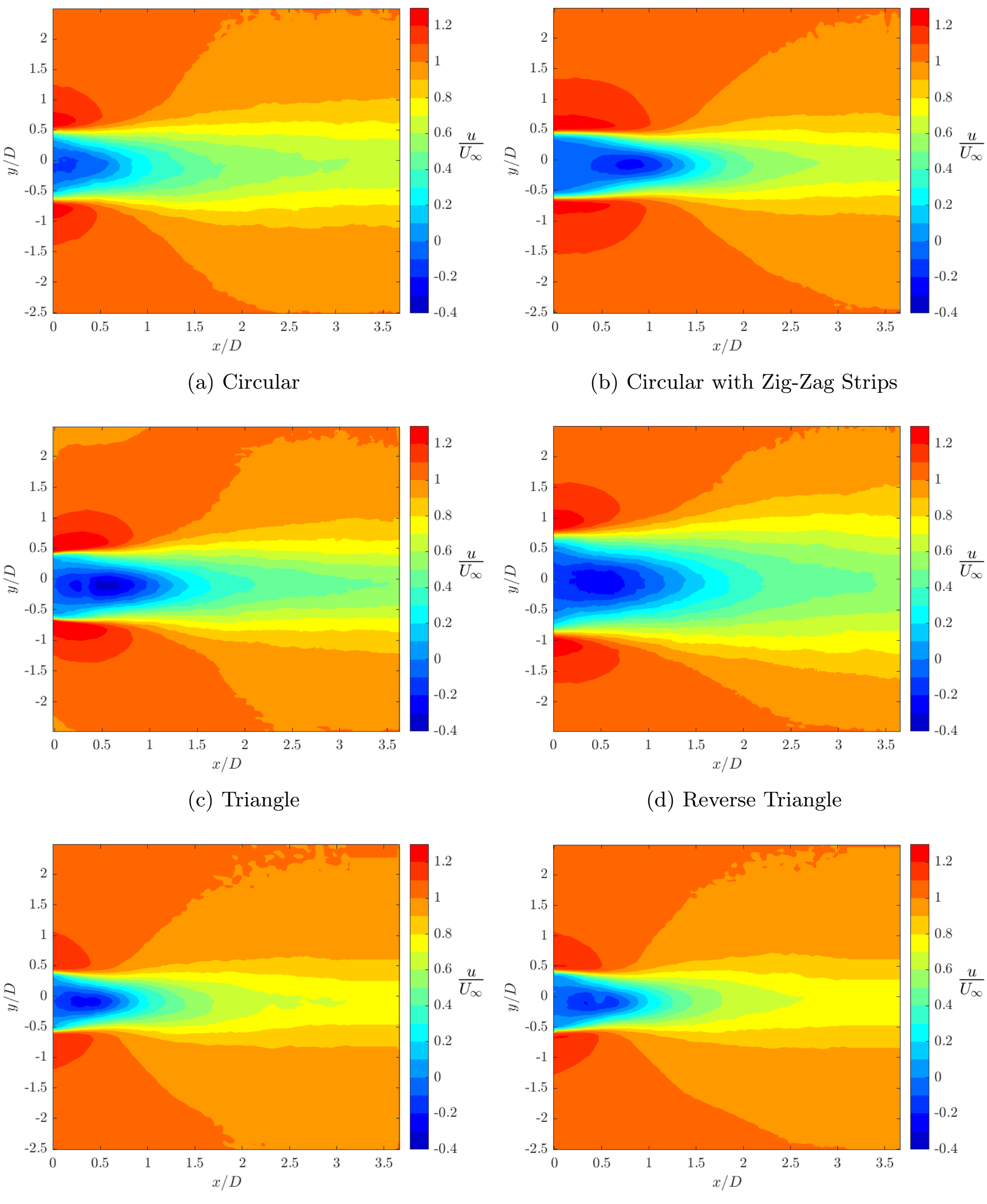

(a) Circular

(b) Circular with Zig-Zag Strips

(c) Triangle

(d) Reverse Triangle

(e) D-Shape

(f) D-Shape with Zig-Zag Strips

Figure 6.1: Bluff bodies' wake velocity fields.

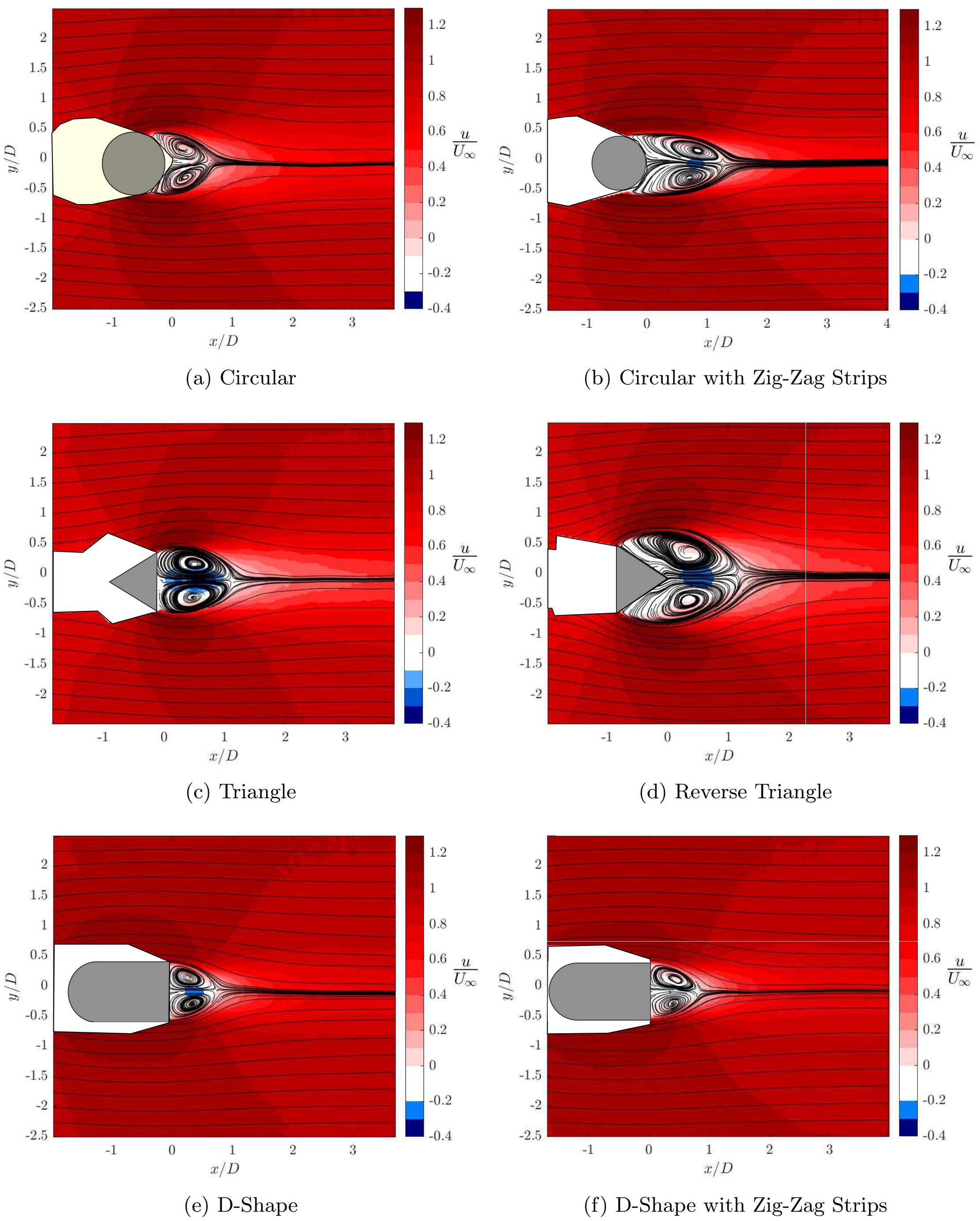

(a) Circular

(b) Circular with Zig-Zag Strips

(c) Triangle

(d) Reverse Triangle

(e) D-Shape

(f) D-Shape with Zig-Zag Strips

Figure 6.2: Bluff bodies' wake streamline fields.

This kind of mechanism disrupts the vortex shedding process; hence, the wake results narrower than the wake generated by a standard circular cylinder. High-velocity regions are also observed in the flow field; the latter envelops the separated shear layers. Those acceleration zones develop differently for each body. Low-velocity zones can instead be observed in the near-wake; those regions also show negative velocity values. That highlights the recirculating behaviour of the flow in the near-wake region after the trailing edge. Besides the velocity magnitude, substantial differences can be appreciated in the size and the shape of the main recirculation zones. Streamlines are an useful tool to expose those differencies. A comparison of the streamline fields has been reported in Fig. 6.2. The recirculation regions consist of two symmetric counter-rotating vortices. The total size of the recirculation regions varies for each case. The length of such a region can be defined as the length for which the velocity becomes null on the wake's centerline, due to the presence of a stagnation point. To quantificate those lengths, velocity profiles on the wake's centerline have been plotted and reported in Fig. 6.3.

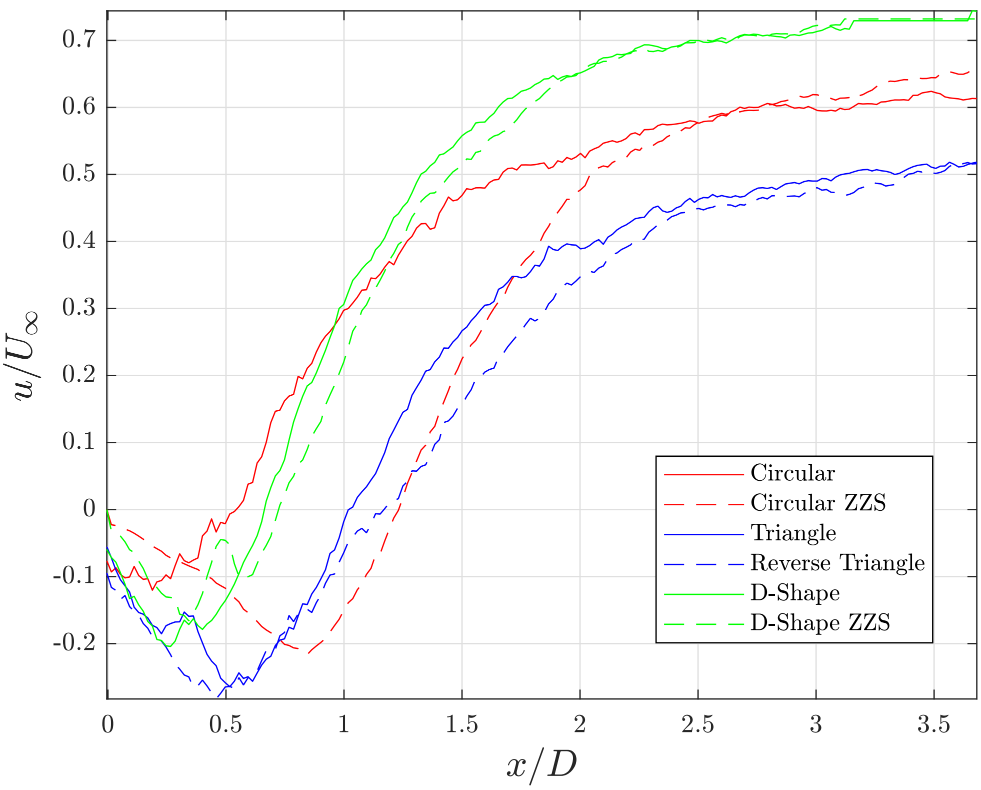

Figure 6.3: Comparison of velocity profiles on the wake's center-line.

The behavior of the velocity on the center-line agrees well with the observations made above. Low-velocity values are present in the near-wake; the velocity rapidly recovers moving downstream, a steep velocity gradient can be observed in the middle wake. On the other hand, an almost constant trend has been found in the far-wake. A clear difference can be observed between two circular cases; in the C case, a wider but shorter recirculation region extending up to $0.5D$ can be observed. On the other hand, the CZZS presents a narrower but much longer recirculation zone extending up to $1.25D$. That well agrees with results achieved by (Koradiya 2018), where

Zig-Zag strips have been applied on a cylinder's surface for drag reduction purposes. The same difference has not been found between the D-Shape bodies; the DZZS case shows a slightly longer recirculation zone though. The same goes for the triangular cases; however, RT shows a bigger recirculation region than T. That is mostly due to the main counter-rotating vortices partially developing on the triangular afterbody for the RT case. It is expected that the structure of the wake is somehow linked to the velocity losses along the wake itself. To quantify those losses, the velocity profiles at $0.5D$,$1.5D$,$2.5D$ and $3.5D$ have been reported in Fig.6.4.

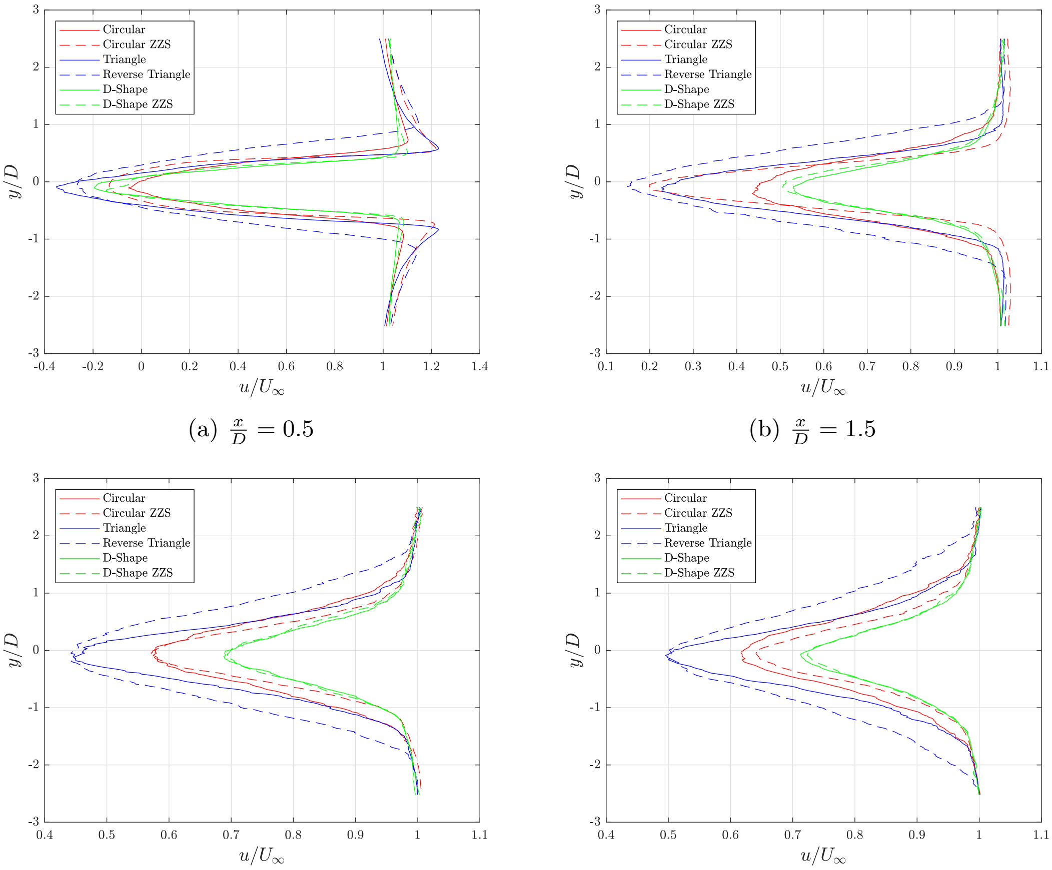

(a) $\frac{x}{D} = 0.5$ (b) $\frac{x}{D} = 1.5$

(c) $\frac{x}{D} = 2.5$ (d) $\frac{x}{D} = 3.5$

Figure 6.4: Comparison of the velocity profiles in four different wake stations.

The velocity profiles resemble a Gaussian bell. The lowest values are reached approximativelly on the centerline; then, the velocity slowly re-asymptotize to the freestream value moving vertically. However, if acceleration regions are present, the profiles will present values higher than 1 before asymptotizing to the freestream value. The acceleration zones are wider and more intense for the RT, the C ZZS and the T case. The highest negative-velocity peaks are reached approximatively on the wake center-line of the first station. Those result higher for the triangular cases; on the other hand,the D, the DZZS and the CZZS present almost the same velocity loss. The lowest velocity losses have instead be found for the C body. Furthermore, the velocity profiles highlight wider velocity loss zones for the triangular bodies and the C one. The second station shows many distinctions between the various cases. The RT presents the highest velocity loss, followed by the CZZS and the T case. On the other hand, the C and both the D-Shape cases show a much lower velocity loss. Moving to the third station, the profiles are starting to collapse on each other showing a certain degree of similarity. The triangular bodies reach the same velocity deficit; the same can be said for the circular cases. The D and the DZZS show completely identical behaviors; both of them present the narrowest and less-intense velocity deficit zone. Overall similar trends can be observed in the final station. In that case, the velocity loss zones are wider and present slightly lower velocity losses compared to the previous station. However, in this case the velocity deficit of the C is higher than the one with the strips. The velocity profiles clearly present higher losses and narrower velocity-loss zones in the first stations. Meanwhile, smaller losses occupying wider zones can be are found in the third and the fourth station. It can also be noticed that, for almost all the stations, the D-Shape bodies exhibit the same behavior. That provides a hint about the possibility that the Zig-Zag strips were not effective on this body. The maximum and minimum velocity values in every station have been summarized in Tab.6.1.

Circular	$x/D = 0.5$	$x/D = 1.5$	$x/D = 2.5$	$x/D = 3.5$
Min u/U_∞	-0.0531	0.43	0.57	0.61
Max u/U_∞	1.10	1	1	1
Circular ZZS	$x/D = 0.5$	$x/D = 1.5$	$x/D = 2.5$	$x/D = 3.5$
Min u/U_∞	-0.13	0.19	0.57	0.64
Max u/U_∞	1.2	1.02	1	1
Triangle	$x/D = 0.5$	$x/D = 1.5$	$x/D = 2.5$	$x/D = 3.5$
Min u/U_∞	-0.35	0.22	0.44	0.49
Max u/U_∞	1.22	1.01	1	1
Reverse Triangle	$x/D = 0.5$	$x/D = 1.5$	$x/D = 2.5$	$x/D = 3.5$
Min u/U_∞	-0.27	0.14	0.44	0.5
Max u/U_∞	1.14	1.01	1	1
D-Shape	$x/D = 0.5$	$x/D = 1.5$	$x/D = 2.5$	$x/D = 3.5$
Min u/U_∞	-0.19	0.52	0.68	0.71
Max u/U_∞	1.06	1.01	1	1
D-Shape ZZG	$x/D = 0.5$	$x/D = 1.5$	$x/D = 2.5$	$x/D = 3.5$
Min u/U_∞	-0.14	0.5	0.69	0.72
Max u/U_∞	1.1	1.01	1	1

Table 6.1: Maximum and minimum non-dimensional velocity values in four different wake stations.

6.1.2 Turbulent Kinetic Energy

The turbulent kinetic energy is associated with turbulent fluctuations, hence, with velocity oscillations present in the flow. The intense vortex shedding generated by a bluff body is the main responsible for the increase of turbulent kinetic energy in the wake. Contour plots of the non-dimensional turbulent kinetic energy field are reported in Fig.6.5. A small circular-shaped low-TKE region is present in the near-wake of all the bodies. That has to be attributed to the hole present in the test section. Major concentrations of TKE are found between the near and the middle-wake. In that zone, the vortex shedding results more intense, thus leading to high oscillations in both the horizontal and vertical velocity components.

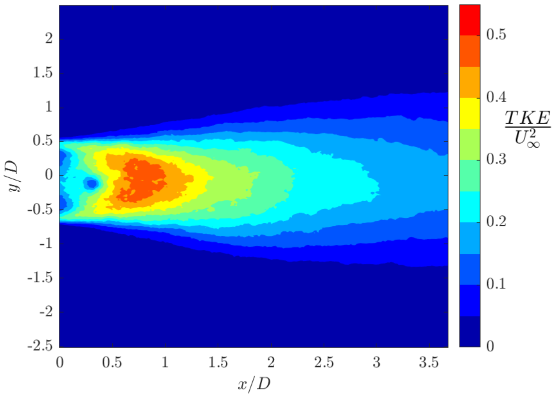

(a) Circular

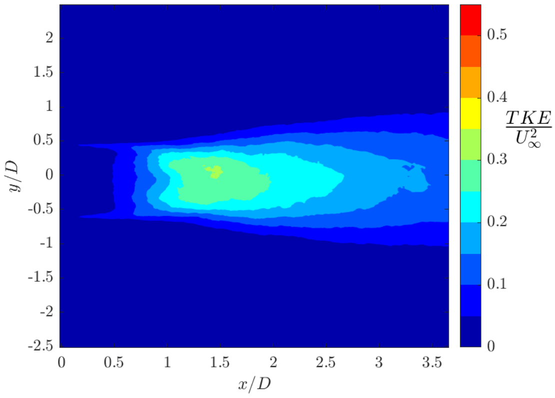

(b) Circular with Zig-Zag Strips

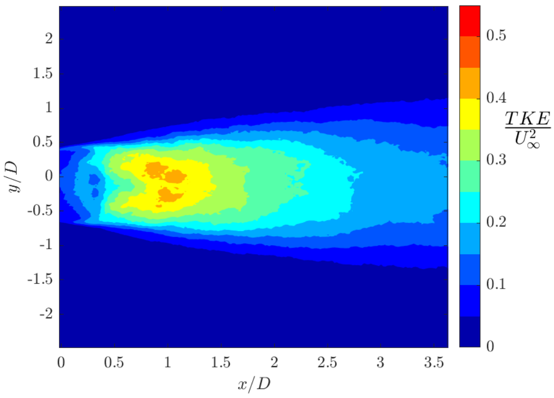

(c) Triangle

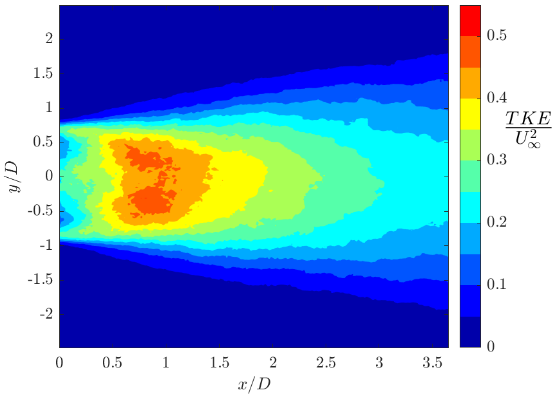

(d) Reverse Triangle

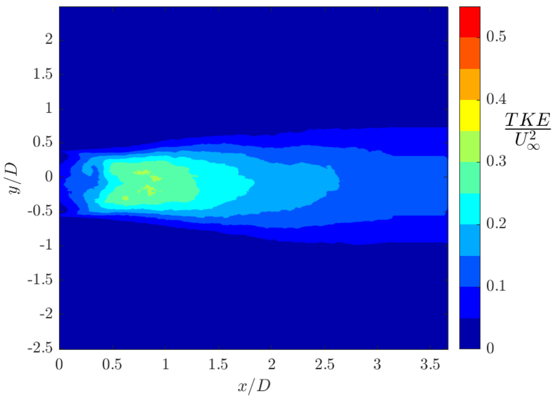

(e) D-Shape

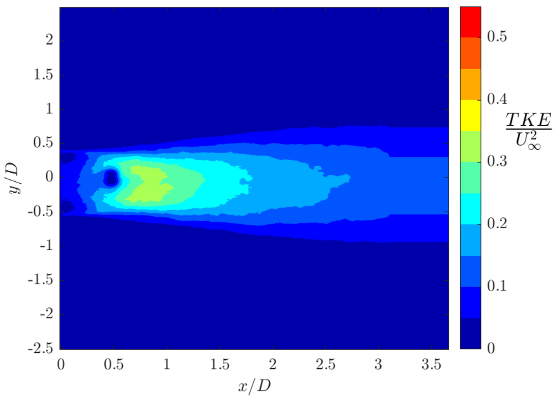

(f) D-Shape with Zig-Zag Strips

Figure 6.5: Bluff bodies' wake non-dimensional TKE fields.

After, the vortices got convected downstream and expands. In the far-wake, the effect of turbulent diffusion leads to an overall smoothing; hence, the main TKE zones becomes wider and less intense. Of particular interest is the comparison between the two circular bodies; due to the intense vortex shedding, the C case exhibits high values of TKE. On the other hand, the circular body with the strips presents a turbulent wake characterized by chaotic motion; hence, much lower velocity fluctuations. Evident differences are also found between the triangular bodies, with the RT showing higher levels of TKE. In agreement with the observation made by (Nakagawa 1989), the RT sheds stronger vortices than the T case but with a lower frequency. Hence, the velocity fluctuations result higher in the former case, thus leading to higher levels of TKE. On the other hand, the D-Shape bodies exhibit the lowest level of TKE. As already stated in section 6.1.1, the afterbody present after the circular nose of these bodies disrupts the shedding process. Hence, the velocity fluctuations got strongly damped. A more detailed analysis has been conducted by plotting non-dimensional TKE profiles in four different stations along the wake, the plots are reported in Fig. 6.6

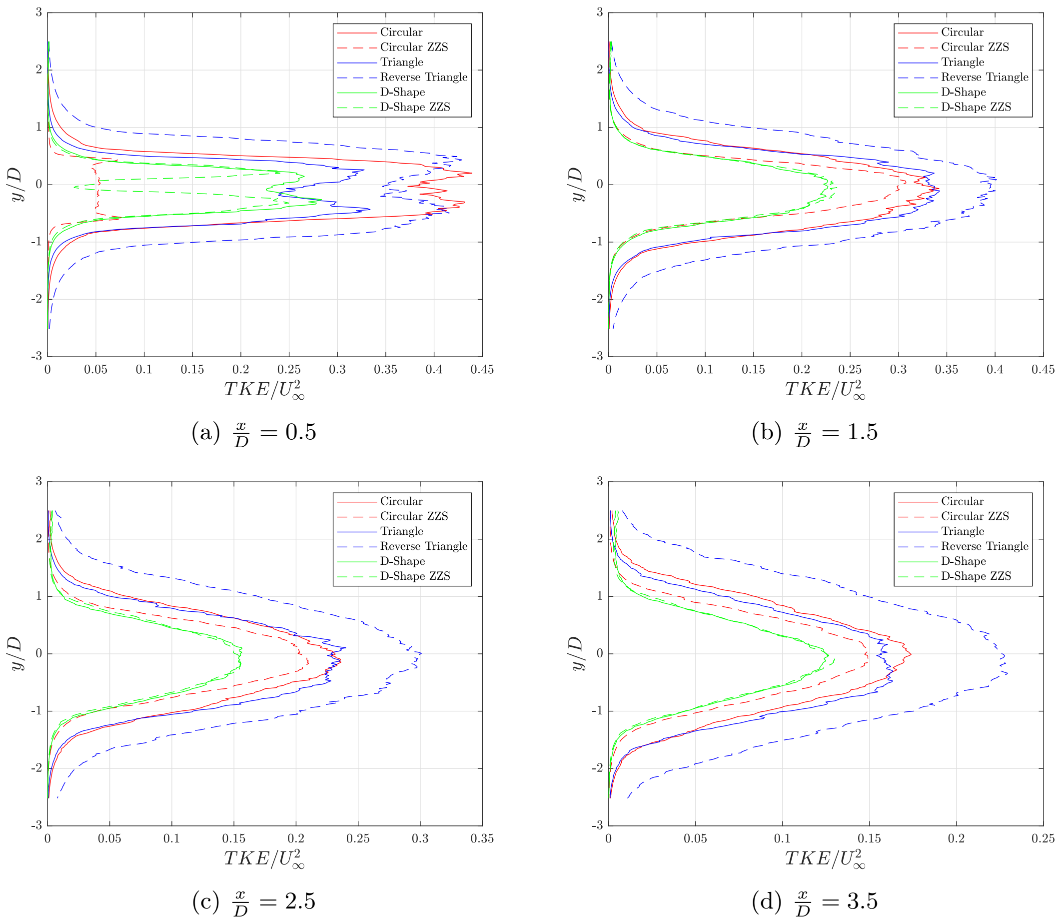

(a) $\frac{x}{D} = 0.5$ (b) $\frac{x}{D} = 1.5$

(c) $\frac{x}{D} = 2.5$ (d) $\frac{x}{D} = 3.5$

Figure 6.6: Comparison of bluff bodies' non-dimensional TKE profiles in four different wake stations.

In the near-wake station, the TKE profiles present a central zone characterized by two symmetrical spikes, both corresponding to TKE peaks. Such a zone is much wider for the RT than the other bodies. On the other hand, it results narrower in the C and T cases and shows an approximatively constant width for the CZZS and both the D-Shape bodies. Outside of that zone, the TKE rapidly decreases to null values. The highest TKE values are found in the RT and the C cases, followed by the T, both the D-shape bodies and finally by the CZZS. Of particular interest is the latter case; the TKE profile of the CZZS presents a constant value in the middle and two small peaks on the sides of the profile. This behavior has been attributed to the effect of the turbulent mixing. Furthermore, a clear difference can also be observed between the shapes of the profiles corresponding to the D-Shape bodies. This difference is mostly related to the presence of the Zig-Zag strips. Moving to the next stations, the turbulent diffusion strongly affects the profiles, now resembling a Gaussian bell. Of particular interest is the CZZS, now showing much higher values of TKE. For all of the remaining stations, the RT still presents the highest TKE peaks, followed by the C and the T cases, which now resent a strongly similar behavior. The same can be stated for the D-Shape bodies. Despite the peaks of TKE gradually decreasing moving downstream, the width of the zones showing high concentration of TKE increase. The highest and the lowest non-dimensional TKE values in every station have been reported in Tab. 6.2.

Circular	$x/D = 0.5$	$x/D = 1.5$	$x/D = 2.5$	$x/D = 3.5$
Min TKE/U_∞^2	2.8×10^{-4}	5.6×10^{-4}	9.1×10^{-4}	0.011
Max TKE/U_∞^2	0.43	0.34	0.23	0.17
Circular ZZS	$x/D = 0.5$	$x/D = 1.5$	$x/D = 2.5$	$x/D = 3.5$
Min TKE/U_∞^2	5.3×10^{-5}	1.36×10^{-4}	1.3×10^{-4}	1.8×10^{-4}
Max TKE/U_∞^2	0.08	0.3	0.21	0.15
Triangle	$x/D = 0.5$	$x/D = 1.5$	$x/D = 2.5$	$x/D = 3.5$
Min TKE/U_∞^2	1.5×10^{-4}	2.3×10^{-4}	4.9×10^{-4}	8.2×10^{-4}
Max TKE/U_∞^2	0.33	0.34	0.24	0.16
Reverse Triangle	$x/D = 0.5$	$x/D = 1.5$	$x/D = 2.5$	$x/D = 3.5$
Min TKE/U_∞^2	0.0014	0.003	0.006	0.008
Max TKE/U_∞^2	0.43	0.4	0.3	0.23
D-Shape	$x/D = 0.5$	$x/D = 1.5$	$x/D = 2.5$	$x/D = 3.5$
Min TKE/U_∞^2	5×10^{-5}	10^{-4}	1.3×10^{-4}	1.7×10^{-4}
Max TKE/U_∞^2	0.28	0.22	0.15	0.12
D-Shape ZZG	$x/D = 0.5$	$x/D = 1.5$	$x/D = 2.5$	$x/D = 3.5$
Min TKE/U_∞^2	3.9×10^{-5}	6.9×10^{-5}	10^{-4}	1.1×10^{-4}
Max TKE/U_∞^2	0.24	0.23	0.15	0.12

Table 6.2: Maximum and minimum non-dimensional TKE values in the four different wake stations.

6.1.3 Pressure fields

Pressure fields have been reconstructed from PIV data by numerically solving the PPE. Fig. 6.7 shows a comparison of the wakes' pressure fields. The wake fields do present pressure values lower than the freestream one. Major pressure deficits are located in the near-wake, which agrees well with the presence of a mean recirculation zone characterized by low-pressure vortices. Moving downstream, the pressure gradually increases, while still not reaching the freestream value. That is mostly due to the limited dimension of the domain. If the measurements were taken further downstream, a complete pressure recovery would have been appreciated.

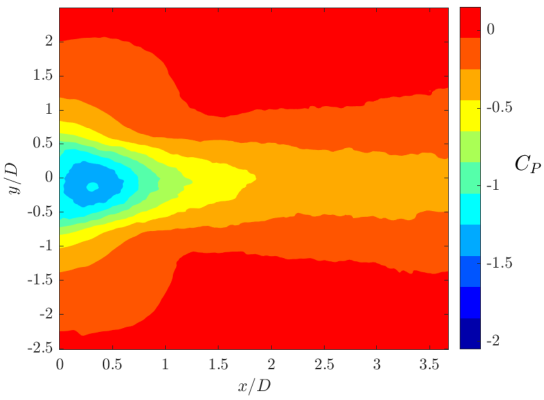

(a) Circular

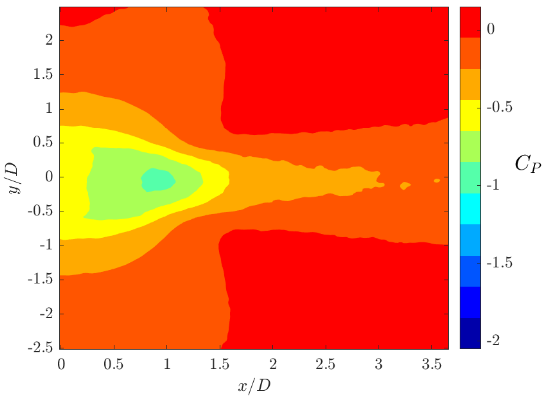

(b) Circular with Zig-Zag Strips

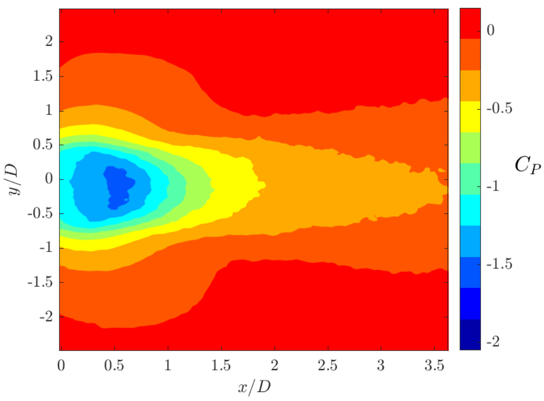

(c) Triangle

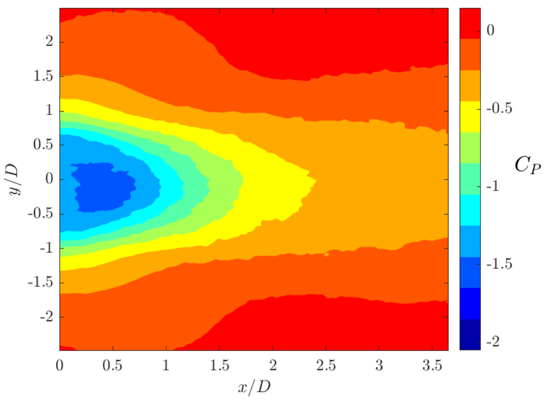

(d) Reverse Triangle

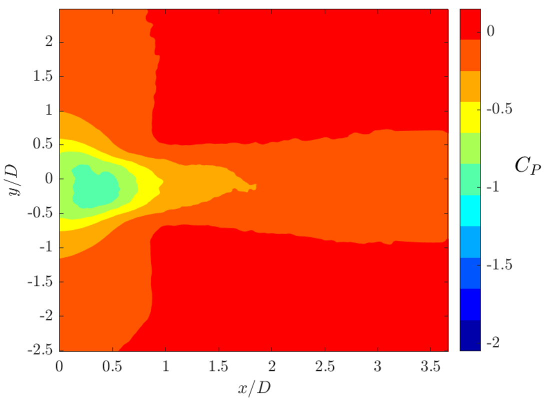

(e) D-Shape

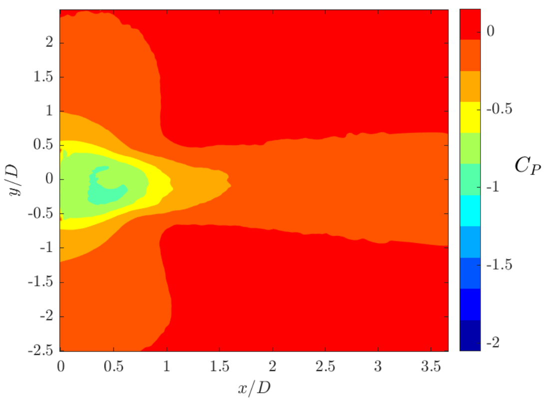

(f) D-Shape with Zig-Zag Strips

Figure 6.7: Bluff bodies' wake pressure coefficient fields.

Despite the similarities among the analyzed bodies, some differences are also observed. The cases presenting a bigger pressure deficit zone are the triangular bodies; in particular, the RT exhibits a pressure-deficit region extending for the majority of the domain. On the other hand, the D-Shape bodies behave almost identically; those bodies present a much narrower pressure-deficit zone, furthermore, the pressure recovery appears to be faster. An interesting behavior can be observed for the CZZS. In this case, the maximum pressure deficit is located more downstream, at approximatively a reference-diameter distance from the trailing edge. Furthermore, the pressure deficit is less intense than the one presented by the C case. To validate the previous statements, the base pressure trend on the center-line of the wake has been reported in Fig. 6.8. Furthermore,pressure profile have been analyzed at four stations in the wake, the profiles are reported in Fig. 6.9.

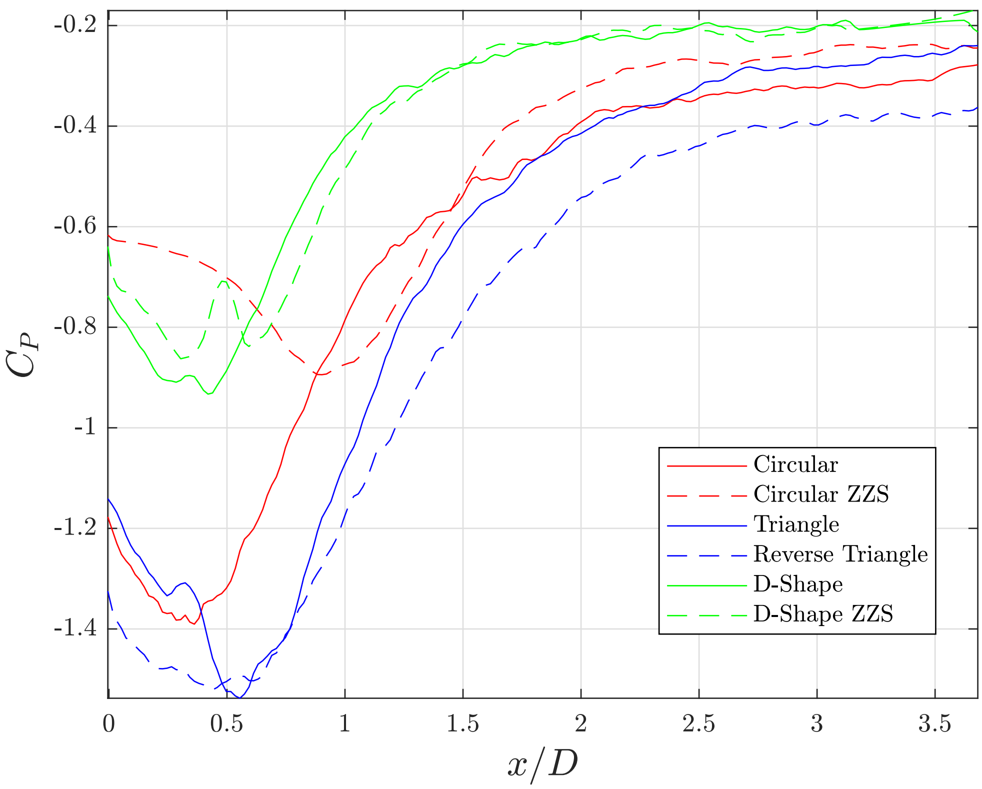

Figure 6.8: Comparison of the base pressure coefficient profiles on the wake's center-line.

Major pressure deficits can be observed in the near-wake. The triangular bodies show the highest negative peaks, followed by the C and the D-Shape cases. As already stated, the pressure-deficit peak is lower and located more downstream for the CZZS case. In agreement with the velocity trend, a steep positive pressure gradient is present right-after the main pressure deficit. Moving further downstream, the pressure gradient decreases and an asymptote is reached in the far-wake. This pressure gradient is almost equal for all the bodies; nonetheless, the RT case exibiths a slower pressure recovery. The pressure profiles present a Gaussian bell shapes. In the first station, the triangular bodies exibith the highest pressure deficits, as well as the widest zones affected by pressure losses. The difference in the peaks is not statistically significant for those bodies, however, the zone affected by the deficit is wider for the reverse one. The same can be said for the D-Shape bodies; in those cases, the pressure profiles are basically identical, except for the DZZS presenting a double peak on the center-line. Contrary, the circular bodies' trends are clearly different from each other. The C case reaches a loss peak much higher than CZZS, meanwhile, it shows a narrower zone affected by the deficit. Differently from the other bodies, the CZZS exhibits a plateau approximatively extending for $0.5D$ at the center of the profile.

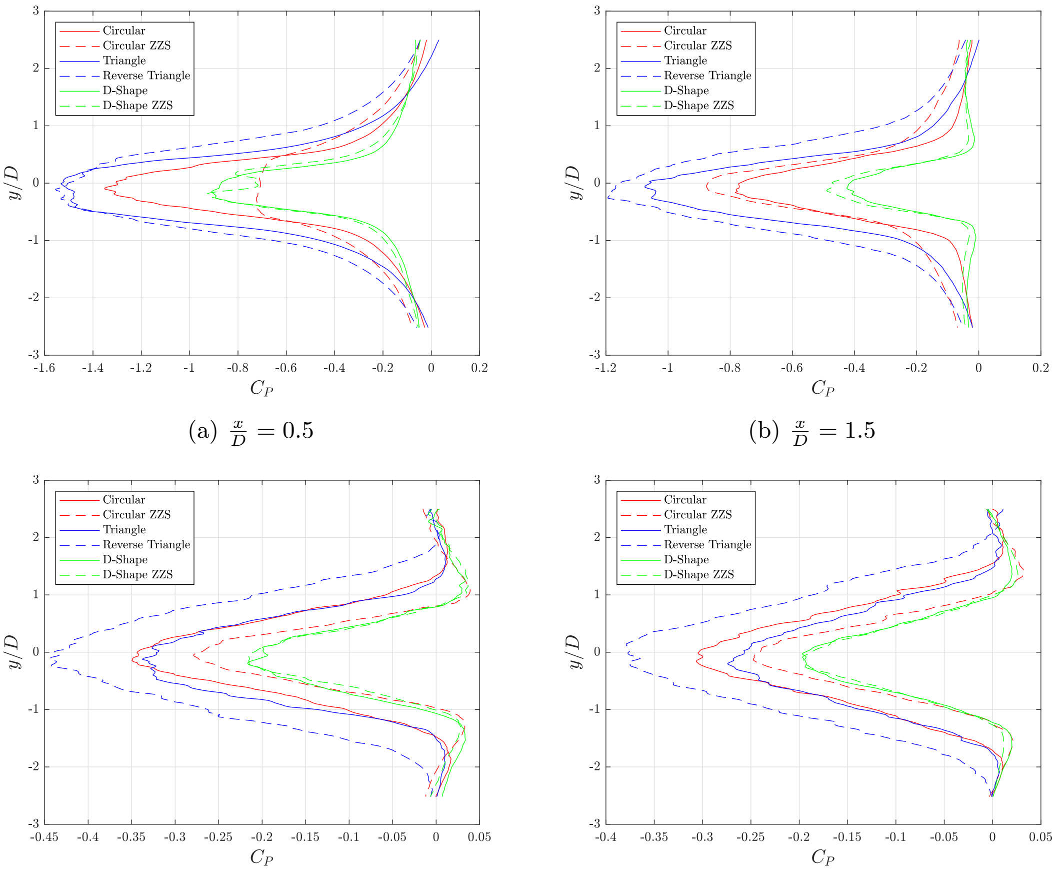

(a) $\frac{x}{D} = 0.5$

(b) $\frac{x}{D} = 1.5$

(c) $\frac{x}{D} = 2.5$

(d) $\frac{x}{D} = 3.5$

Figure 6.9: Comparison of pressure coefficient profiles in four different wake stations.

It is not clear if the reason behind this trend has to be attributed to the turbulent mixing in the near-wake or to the choice of a Neumann-boundary condition on the left boundary of the domain. Moving to the second station, this trend is cannot be appreciated anymore; in this station, the CZZS shows a pressure deficit higher than the C body's one. In this station, the highest pressure deficit is presented by the RT, followed by the T, the CZZS and the C. Hence, the D-Shape bodies show the lowest pressure deficit also in this station. The overall pressure coefficient values result negative in the first two stations, hence, none of the bodies reaches the freestream pressure. Nonetheless, the T body is the only one managing to reach the freestream pressure on the top and the bottom boundaries. Moving to the third station, the pressure profiles appear more squeezed. Positive pressure coefficient values are finally reached outside the deficit zones. The RT still exhibits the highest pressure deficit peak. A similitude has been observed between the trends of the C and the T body. The same can be said for the D-Shape bodies, which basically show identical behaviors in this station. The same similarities have also been observed in the final station; despite showing the same trend, the C and the T body present more discrepancies at the profile peak. Overviewing the plots, it is possible to notice that the pressure deficit's difference between the last two stations is far lower than the one between the second and the third one. The same goes for the width of the zones affected by a pressure deficit in the wake profiles. The highest and the lowest pressure coefficient values found in the four stations have been reported in Tab.6.3.

Circular	$x/D = 0.5$	$x/D = 1.5$	$x/D = 2.5$	$x/D = 3.5$
Min C_P	-1.35	-0.78	-0.34	-0.30
Max C_P	-0.018	-0.02	0.01	0.01
Circular ZZS	$x/D = 0.5$	$x/D = 1.5$	$x/D = 2.5$	$x/D = 3.5$
Min C_P	-0.72	-0.87	-0.27	-0.24
Max C_P	-0.046	-0.063	0.039	0.033
Triangle	$x/D = 0.5$	$x/D = 1.5$	$x/D = 2.5$	$x/D = 3.5$
Min C_P	-1.5	-1	-0.33	-0.28
Max C_P	0.03	0	0.011	0
Reverse Triangle	$x/D = 0.5$	$x/D = 1.5$	$x/D = 2.5$	$x/D = 3.5$
Min C_P	-1.5	-1	-0.33	-0.28
Max C_P	0.03	0	0.011	0
D-Shape	$x/D = 0.5$	$x/D = 1.5$	$x/D = 2.5$	$x/D = 3.5$
Min C_P	-0.9	-0.42	-0.21	-0.19
Max C_P	-0.05	0	0.03	0.02
D-Shape ZZG	$x/D = 0.5$	$x/D = 1.5$	$x/D = 2.5$	$x/D = 3.5$
Min C_P	-0.92	-0.48	-0.21	-0.19
Max C_P	-0.04	-0.02	0.03	0.02

Table 6.3: Maximum and minimum pressure coefficient values in four different wake stations.

6.2 NACA-0012 flow topologies comparison

6.2.1 Velocity fields

Typical airfoil flows are characterized by narrow wake-regions, low velocity losses, and small pressure deficits. Those features are typical of streamlined bodies presenting a delayed separation or no separation at all. However, those characteristics depend upon several factors as the Reynolds number, the geometric characteristics of the airfoil, and the angle of incidence. The wake velocity fields of the NACA-0012 at different angle of incidence are reported in Fig. 6.10.

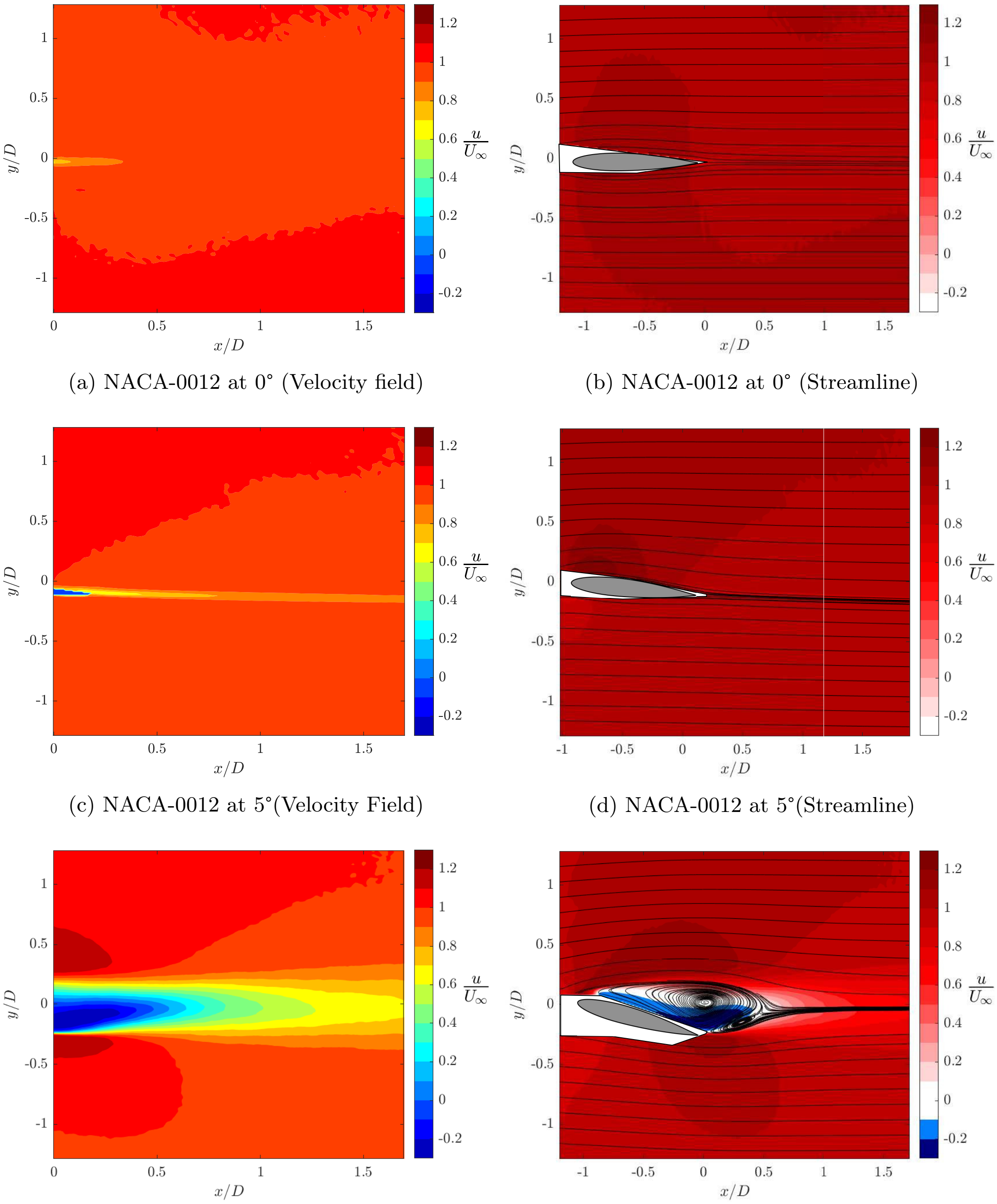

(a) NACA-0012 at 0° (Velocity field)

(b) NACA-0012 at 0° (Streamline)

(c) NACA-0012 at 5°(Velocity Field)

(d) NACA-0012 at 5°(Streamline)

(e) NACA-0012 at 15°(Velocity Field)

(f) NACA-0012 at 15°(Streamline).

Figure 6.10: NACA-0012 wake non-dimensional velocity fields for different incidences (Left),NACA-0012 wake streamline fields for different incidences (Right)

Narrow wake regions, resulting from a delayed separation, can be observed for both the low-incidence cases. Symmetrical velocity oscillations lead to a symmetrical mean velocity field for the airfoil at null incidence. On the other hand, a downwash effect can be observed for the airfoil at 5° of incidence. At 15° of incidence, the strong adverse pressure gradient on the suction side of the airfoil leads the flow to experience early separation. The resulting velocity field exhibits a wide wake with elevated velocity losses. Furthermore, the negative velocity values suggest the presence of a recirculation zone.

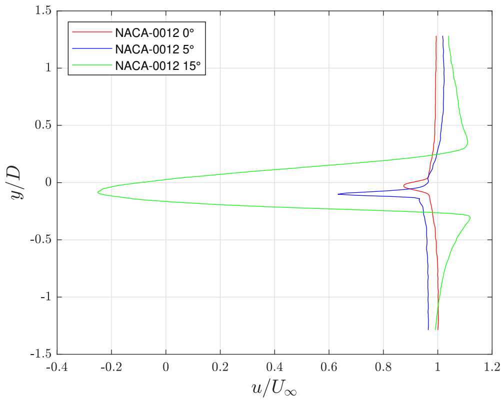

(a) $\frac{x}{D} = 0.25$

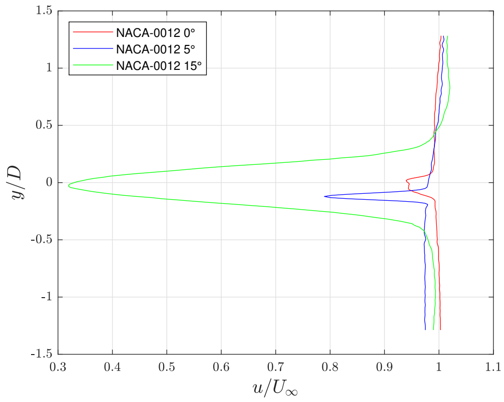

(b) $\frac{x}{D} = 0.75$

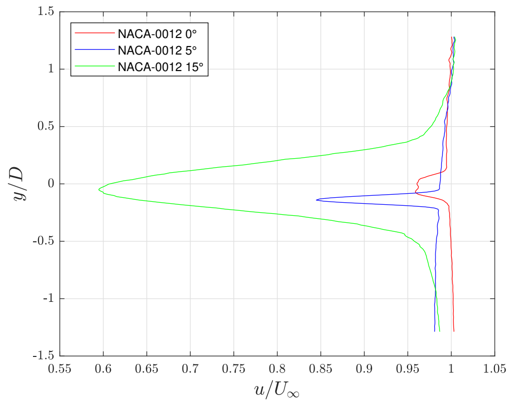

(c) $\frac{x}{D} = 1.25$

Figure 6.11: Comparison non-dimensional velocity profiles in three different wake stations.

Contrary, their absence gives hints about the absence of the latter in both the low-incidence configurations. Those statements are validated through the streamline fields reported in Fig. 6.10. As expected, the only case clearly showing a main recirculation region is the high-incidence one. This region consists of a bigger clockwise-rotating vortex and a smaller counter-rotating one. Its total length covers the whole airfoil-chord and further extends up to almost 0.5 chord-reference length after the trailing edge. The massive dimensions of the main recirculation zone put emphasis on the airfoil's stall. In order to quantify and compare the the velocity losses, velocity profiles in three station located at $0.25D$,$0.75D$ and $1.25D$ have been reported in Fig. 6.11. For the low-incidence cases, the velocity profiles exhibit a constant trend with a small peak corresponding to the wake region. On the other hand, the 15° configuration presents much higher velocity-loss peaks. Values higher than the freestream velocity are reached outside the wake-flow region for the stalled configuration. Those correspond with the acceleration regions outside the wake; being the flow highly asymmetrical, those regions also result asymmetrical. Those strong-acceleration zones can be found in the wake field only for the stalled configuration due to the presence of a large-wake region. It can be also noticed that the freestream values on the top and the bottom boundaries are slightly different for both the 5° and the 15° configurations. That is mainly due to the difference in the freestream value between the two boundaries; hence, this effect becomes more evident moving downstream to the final stations. The velocity-loss peaks are higher in the first stations, then, they gradually decrease moving downstream. On the other hand, the width of the regions affected by velocity losses increases moving downstream. The maximum and minimum velocity values retrieved in the analyzed stations are reported in tab 6.4.

NACA-0012 (0°)	$x/D = 0.25$	$x/D = 0.75$	$x/D = 1.25$
Min u/U_∞	0.87	0.93	0.95
Max u/U_∞	1	1	1
NACA-0012 (5°)	$x/D = 0.25$	$x/D = 0.75$	$x/D = 1.25$
Min u/U_∞	0.63	0.78	0.84
Max u/U_∞	1.02	1	1
NACA-0012 (15°)	$x/D = 0.25$	$x/D = 0.75$	$x/D = 1.25$
Min u/U_∞	-0.25	0.31	0.59
Max u/U_∞	1.11	1.01	1

Table 6.4: Maximum and minimum non-dimensional velocity values in three different wake stations.

6.2.2 Turbulent Kinetic Energy

Non-dimensional turbulent kinetic energy contour plots of the airfoil cases have been reported in Fig. 6.12. The narrow Von Karman vortex streets generating from the airfoil at 0° and at 5° exhibit weak velocity oscillation. Hence, approximately null TKE values are present in those cases. Slightly higher values are present in the near-wake though, right-after the airfoil trailing edge. On the other hand, much higher TKE values can be observed in the wake region of the stalled airfoil. The peak of TKE is located in correspondence with the small counter-clockwise-rotating vortex on the bottom part of the main recirculation zone. Out of that region, the TKE gradually decreases moving downstream. Three different stations have been chosen to analyze the TKE profiles in the wake region, the corrispondent plots have been reported in Fig. 6.12. As expected, major TKE values are observed for the airfoil at 15°. For that configuration, the region presenting high TKE values presents a width of approximatively one reference-chord in the first station. Due to the different TKE intensity between the two vortexes composing the main recirculation zone, this profile presents an high degree of asymmetry in the first station.

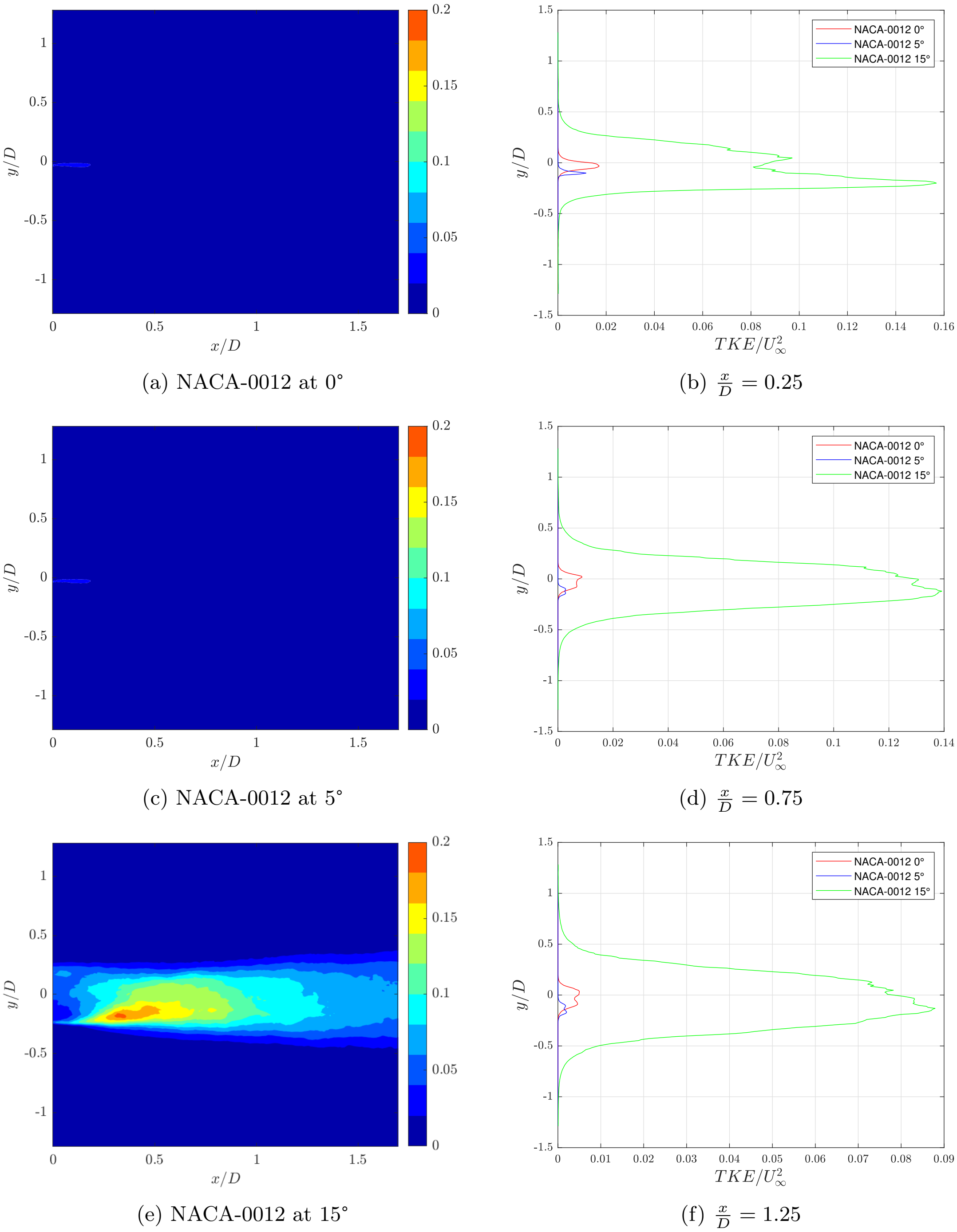

(a) NACA-0012 at 0°

(b) $\frac{x}{D} = 0.25$

(c) NACA-0012 at 5°

(d) $\frac{x}{D} = 0.75$

(e) NACA-0012 at 15°

(f) $\frac{x}{D} = 1.25$

Figure 6.12: NACA-0012 wake non-dimensional TKE fields for different incidences (Left),Comparison of wake non-dimensional TKE profiles in three different wake stations.(Right).

On the other hand, the low incidence configurations exhibit a more symmetrical trend in this station. The TKE peak has been found to be slightly lower for the 5° configuration; that is mostly due to the larger Von-Karman street generated by the airfoil at null incidence. The TKE peaks decrease moving downstream as the vortexes expand and lose intensity. Furthermore, the shape of the profiles got smoothed moving downstream thanks to the effect of the turbulent diffusion. The higest and the lowest values retrivied in the three stations have been resumed in Tab. 6.5.

NACA-0012 (0°)	$x/D = 0.25$	$x/D = 0.75$	$x/D = 1.25$
Min TKE/U_∞^2	8.5×10^{-6}	9.8×10^{-6}	1.4×10^{-5}
Max TKE/U_∞^2	0.017	0.009	0.005
NACA-0012 (5°)	$x/D = 0.25$	$x/D = 0.75$	$x/D = 1.25$
Min TKE/U_∞^2	1.7×10^{-5}	1.5×10^{-5}	1.4×10^{-5}
Max TKE/U_∞^2	0.011	0.0028	0.002
NACA-0012 (15°)	$x/D = 0.25$	$x/D = 0.75$	$x/D = 1.25$
Min TKE/U_∞^2	2.5×10^{-5}	3.5×10^{-5}	6.5×10^{-5}
Max TKE/U_∞^2	0.15	0.14	0.088

Table 6.5: Maximum and minimum non-dimensional TKE values in three different wake stations.

6.2.3 Pressure fields

The pressure fields have been reported in Fig.6.13. No significant pressure loss is observed for the low-incidence configurations. Particularly, an high pressure zone can be observed nearby the trailing edge for the null-incidence configuration; this behaviour suggest the presence of a second stagnation point. Contrary, a large pressure deficit asymmetric zone can be observed in the near-wake of the airfoil at 15° of incidence. This zone extends up to $0.5D$; then, the pressure gradually recovers moving downstream. On the other hand, it occupies a vertical distance extending from $-0.5D$ and $0.5D$; outside that range, the pressure experiences recovery also along the vertical direction. In order to provide a physical insight of the previous statements, the pressure profile in three stations have been reported in Fig.6.13. The pressure profiles of the airfoil at null incidence result are approximatively symmetric in the first two stations. Those profiles exhibit almost null values on the top and bottom boundaries; hence, the pressure reached in those points equals the freestream one. Moving towards the center-line, two similarly-symmetric compression zones can be observed; those are mostly due to the adverse pressure gradient offered by the airfoil shape. A small pressure drop is observed in the wake region; this difference gradually decreases moving downstream though. In the far-wake station, the pressure profile for the airfoil at 0° appears to lose its symmetric traits.

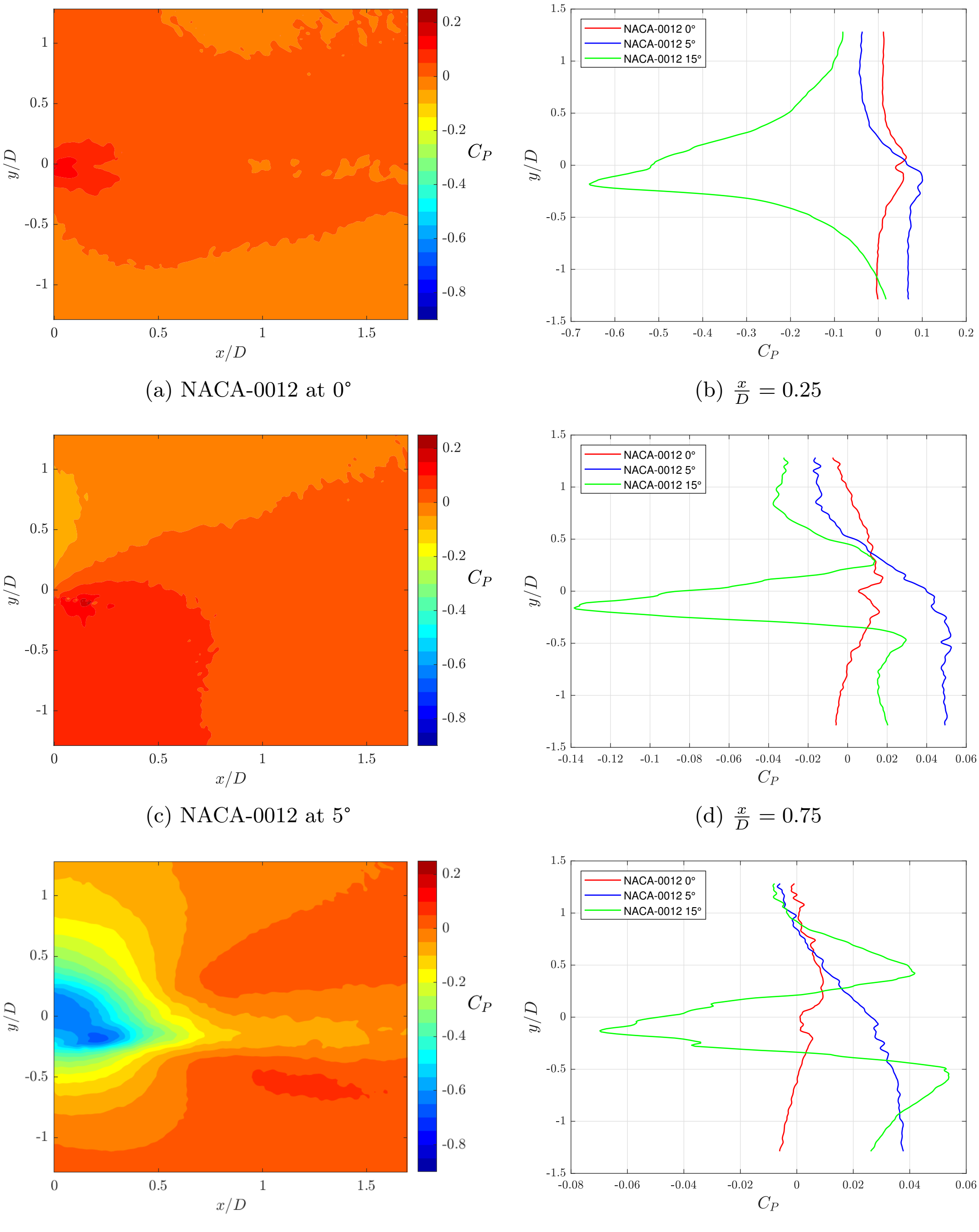

(a) NACA-0012 at 0°

(b) $\frac{x}{D} = 0.25$

(c) NACA-0012 at 5°

(d) $\frac{x}{D} = 0.75$

(e) NACA-0012 at 15°

(f) $\frac{x}{D} = 1.25$

Figure 6.13: NACA-0012 wake pressure coefficient fields for different incidences (Left), Comparison of wake pressure coefficient profiles in three different wake stations (Right).

Overall similar behaviors can be noticed for the airfoil at not-null incidences, however, those cases are asymmetrical due to the flow's asymmetry itself. Furthermore, the airfoil at 5° exhibits positive pressure differences higher than the null-incidence case. On the other hand, high-pressure deficits are observed for the airfoil at 15°; those pressure deficits drastically decrease moving downstream though. The maximum and minimum pressure coefficient values in all the stations have been resumed in Tab.6.6

NACA-0012 (0°)	$x/D = 0.25$	$x/D = 0.75$	$x/D = 1.25$
Min C_P	-0.0044	-0.0075	-0.0061
Max C_P	0.063	0.017	0
NACA-0012 (5°)	$x/D = 0.25$	$x/D = 0.75$	$x/D = 1.25$
Min C_P	-0.043	-0.017	0
Max C_P	0.1	0.05	0.04
NACA-0012 (15°)	$x/D = 0.25$	$x/D = 0.75$	$x/D = 1.25$
Min C_P	-0.65	-0.13	-0.069
Max C_P	0.017	0.029	0.053

Table 6.6: Maximum and minimum pressure coefficient values in three different wake stations.

6.3 Drag quantification models comparison

6.3.1 Bluff bodies Drag quantification

The plots reported in Fig.6.14 show the drag coefficient obtained through the MCV approach, as a function of the streamwise distance. The reported plots show an overall similar trend. Every case presents an overall constant drag coefficient over the length of the control volume. The pressure term is more relevant in near-wake, meanwhile the momentum term gives an higher contribution moving downstream. On the other hand, the Reynolds stress term gives a much smaller contribution to the total drag, while still being not neglectable. Interestingly, the D-Shape bodies show almost the same trend and the same drag coefficient; that might confirm that the transition was not achieved. The momentum term is initially negative; that is mostly due to the negative velocity values in the main recirculation zone. Furthermore, the high-velocity values present in the acceleration regions outside the shear-layers also give negative contributions. Both of those are present in the first part of the domain; hence, the momentum term acts as a trust force in that region. In agreement with the statements made in Section 6.1.1, the length of this region is higher for the bodies presenting longer recirculation zones.

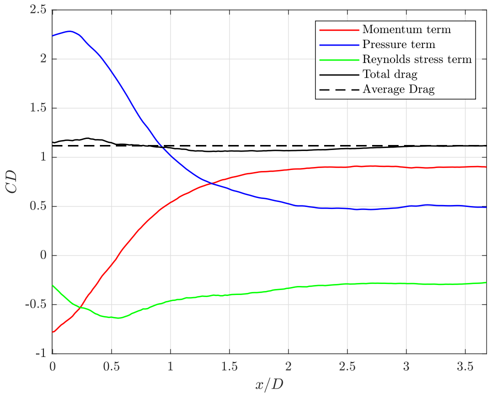

(a) Circular

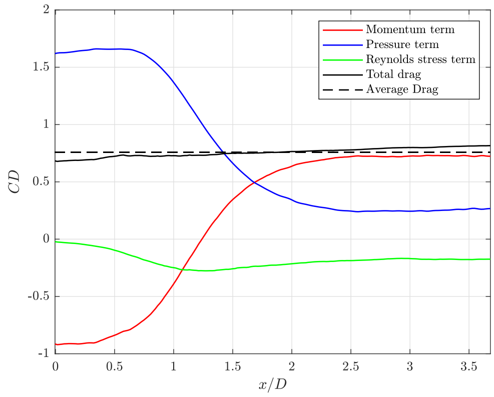

(b) Circular with Zig-Zag Strips

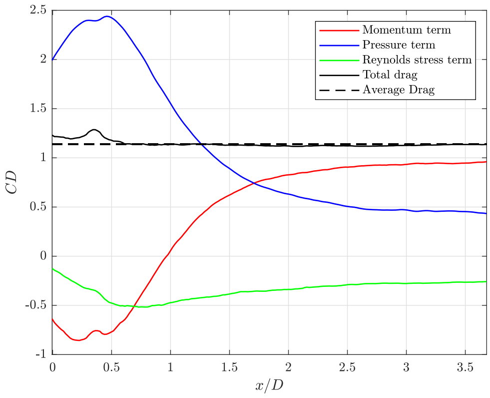

(c) Triangle

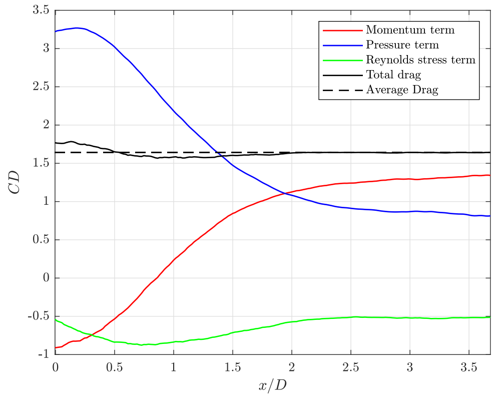

(d) Reverse Triangle

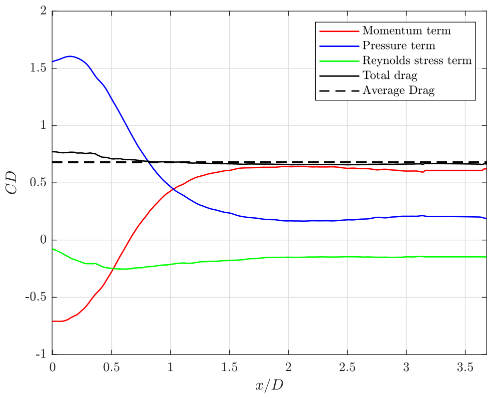

(e) D-Shape

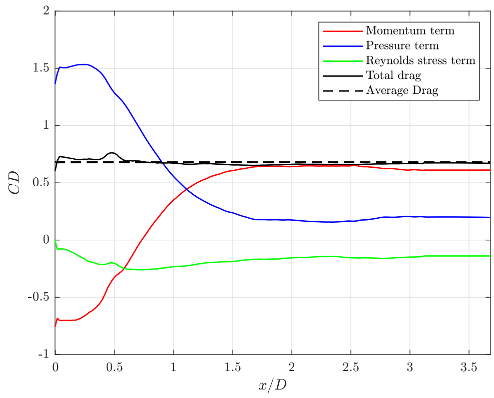

(f) D-Shape with Zig-Zag Strips

Figure 6.14: Drag coefficient obtained through the MCV approach as a function of the streamwise distance.

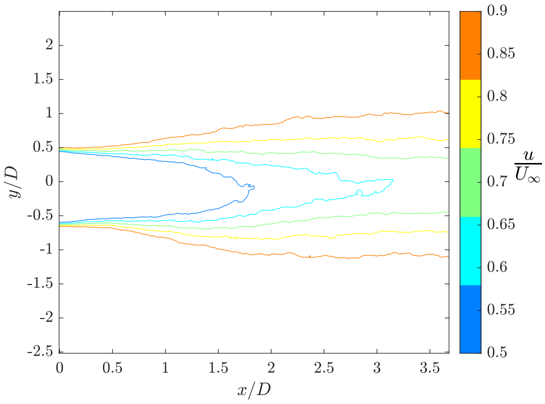

(a) Circular

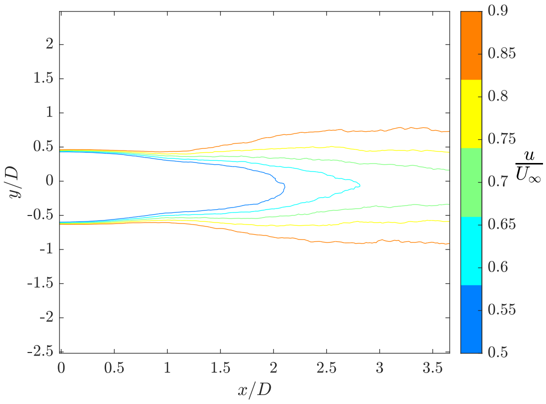

(b) Circular with Zig-Zag Strips

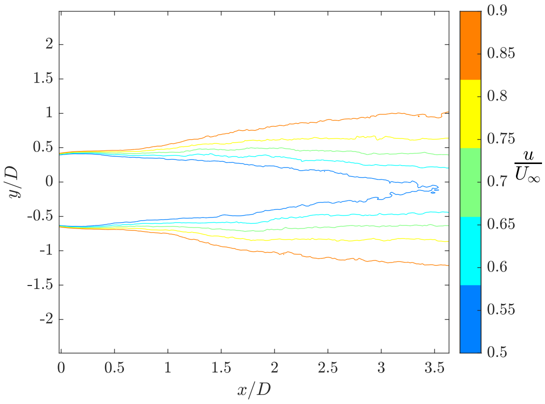

(c) Triangle

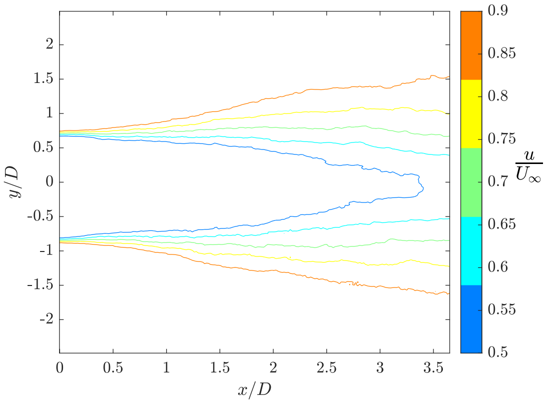

(d) Reverse Triangle

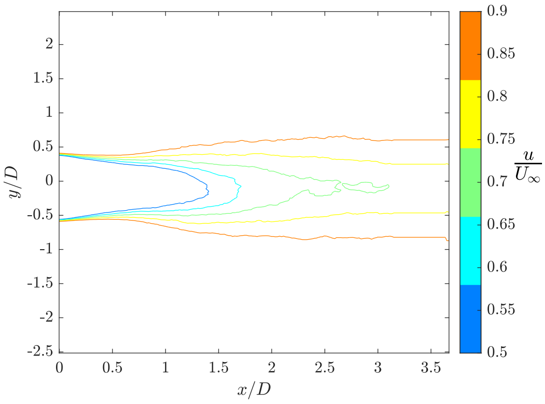

(e) D-Shape

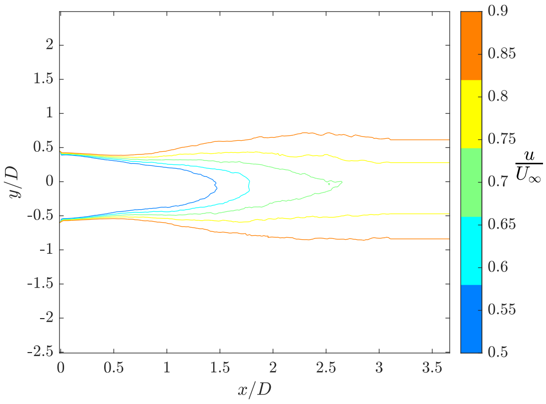

(f) D-Shape with Zig-Zag Strips

Figure 6.15: Velocity contour-lines corresponding to the cut-off velocities.

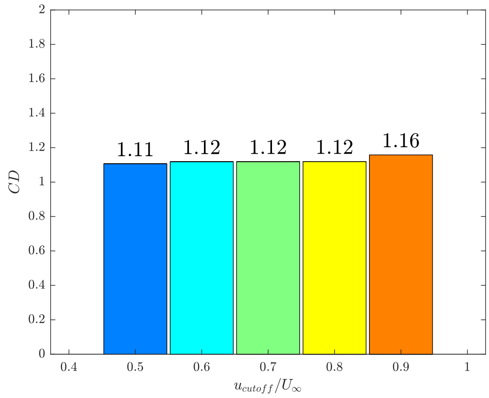

(a) Circular

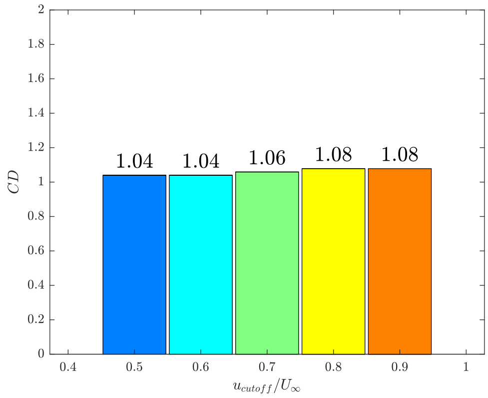

(b) Circular with Zig-Zag Strips

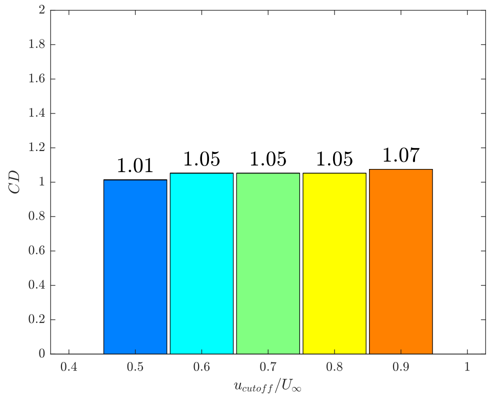

(c) Triangle

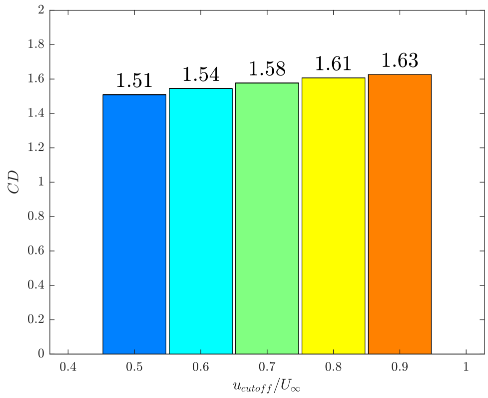

(d) Reverse Triangle

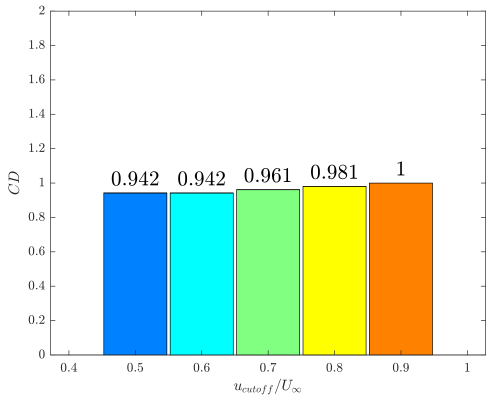

(e) D-Shape

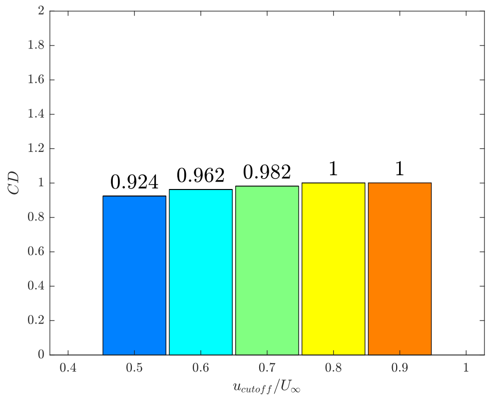

(f) D-Shape with Zig-Zag Strips

Figure 6.16: Drag coefficient obtained through the EWA approach as a function of the cut-off velocity parameter.

The momentum term increases moving downstream, eventually reaching positive values. The rate of increase is higher after the main recirculation zone; moving downstream, the slope of the curve strongly decreases until a constant trend is reached in the far-wake. The pressure deficit term shows an opposite trend. This term is higher in the near-wake due to the presence of low-pressure vortexes in the main recirculation zone. Outside of that zone, the pressure deficit term gradually decreases due to the positive pressure gradient in the streamwise direction. As for the momentum term, the pressure term finally tends to a plateau in the far-wake. The pressure deficit remains positive over the whole length of the control volume; hence, it always contributes drag force. If the measurements were taken further downstream, the pressure term would have resulted neglectable due to the complete pressure recovery. An interesting point in the plots is found at the downstream distance for which the momentum and the pressure contributes are equivalent. The location of this point varies from case to case, however, it appears to be higher for the cases presenting a larger recirculation region. Finally, the Reynolds stress term shows an overall similar trend for all the cases. This term should provide higher negative values in the near-wake, where the velocity oscillations are higher. The value of this term in correspondence of the trailing edge is directly linked to the intensity of the velocity oscillations.

Geometry	$\Delta CD(0.6U_\infty)$	$\Delta CD(0.7U_\infty)$	$\Delta CD(0.8U_\infty)$	$\Delta CD(0.9U_\infty)$
Circular	1.1%	1.16%	1.2%	4.5%
Circular ZZS	0%	1.8%	3.6%	3.6%
Triangle	3.6%	3.6%	3.6%	5.7%
Reverse Triangle	2.3%	4.3%	6.1%	7.2%
D-Shape	0%	2%	3.9%	5.8%
D-Shape ZZS	4%	5.9%	7.7%	7.7%

Table 6.7: Percentage difference in the drag coefficients for different cut-off velocity values with respect to the drag coefficient obtained for $0.5U_\infty$.

In agreement with the observation made in Section 6.1.2, the Reynolds stress value is higher in magnitude for the RT, the C and the T bodies. On the other hand, it is far lower for the D-Shape bodies and the CZZS, for which it shows almost shows null-values. The negative peaks are reached between $0.5D$ and D, in correspondence with the main recirculation zone's center. Moving downstream, the Reynolds Stress contribution should rapidly tend to null values; however, this kind of behavior is not observed in the present analysis. Due to the background noise, the rate of decrease of the Reynolds stress contributions is not high enough to allow it to reach null-values. As discussed in Section 5.5, the EWA approach relies on the measurement of the area of the wake's portion corresponding to $0.5U_\infty$ cut-off velocity, projected onto the body's trailing edge. Due to the close correlation between the drag value and the velocity cut-off parameter, a dependency study has been carried out. Fig.6.15 and Fig.6.16 report the velocity contour-lines corresponding to the chosen cut-off velocities and the correspective drag values respectivelly. The energized region individuated by the standard cut-off velocity of $0.5U_\infty$ appears closed for all the test cases. Nonetheless, its dimensions varies for each body. This region appears longer for the triangular bodies, with the RT showing a region just slightly longer than the T one. On the other hand, a clear difference has been found between the circular bodies. Moving to higher cut-off velocities, the region corresponding to $0.6U_\infty$ is still closed for the circular and the D-Shape bodies. The same cannot be said for the triangular bodies. The region corresponding to $0.7U_\infty$ is closed only for the D-Shape bodies, and finally, the regions corresponding to $0.8U_\infty$ and $0.9U_\infty$ are open for all the test cases. The width of those zones correspond with the one-dimensional areas of the energized regions. It is evident that the model is almost insensitive to the choice of the cut-off velocity.

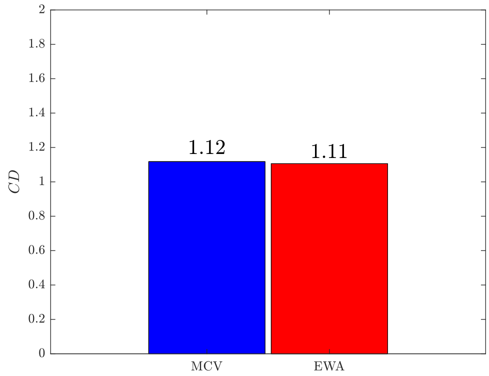

(a) Circular

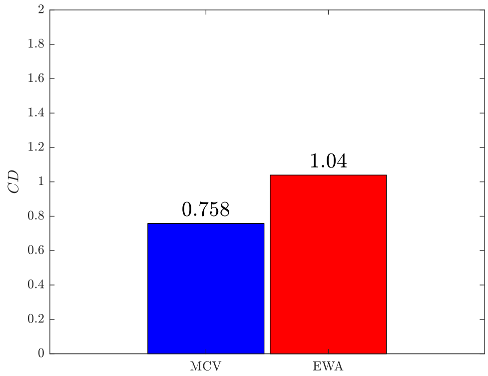

(b) Circular with Zig-Zag Strips

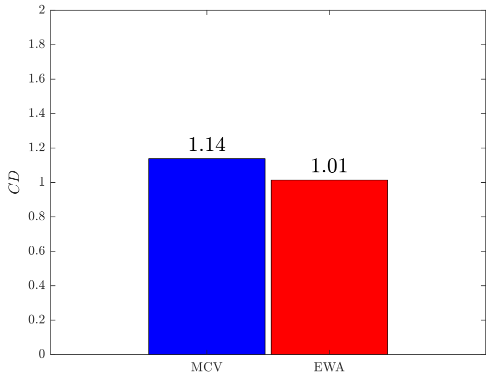

(c) Triangle

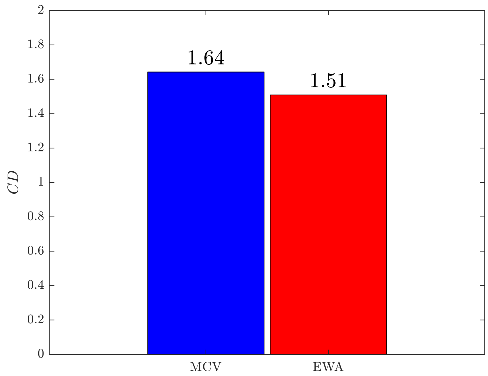

(d) Reverse Triangle

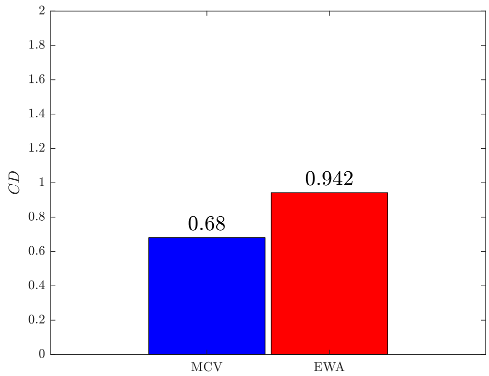

(e) D-Shape

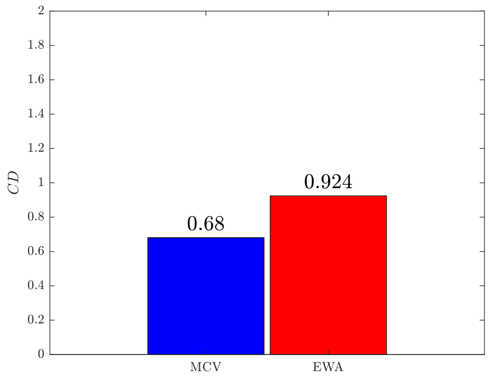

(f) D-Shape with Zig-Zag Strips

Figure 6.17: Comparison between EWA and MCV models' drag coefficients.

The percentage difference between the drag values corresponding to the standard cut-off velocity of $0.5U_\infty$ and the the others have been reported in Tab.6.7. If the cut-off velocity does not exceed the value of $0.8U_\infty$, the differences in drag stay between 1% and 5% for the T, the D, and both the circular bodies. On the other hand, a slightly higher degree of sensitivity has been found for the RT and the DZZS. Furthermore, a tendency to higher drag values for $0.9U_\infty$ can be observed for all the bodies. The EWA results have been validated through the comparison with the ones obtained through the MCV approach. Fig. 6.17 shows a direct comparison between the two models. The best agreement has been found for the C body. In this case, the difference between the drag coefficients is about 1%. On the other hand, a major difference has been found for the CZZS, showing a difference of 27.1% between the two models. The triangular bodies show an overall good agreement. The T body exhibits a difference of 10.9%; meanwhile, the RT shows a slightly minor one of 8.1%. Finally, major discrepancies are found for both the D-Shape bodies; in such cases, the difference between the two approaches is about 27%. The final drag coefficients obtained through the two models and their percentage differences have been resumed in Tab. 6.8.

Geometry	CD_{MCV}	CD_{EWA}	ΔCD
Circular	1.12	1.11	−1%
Circular ZZS	0.75	1.04	+27.1%
Triangle	1.14	1.01	−10.9%
Reverse Triangle	1.64	1.51	−8.1%
D-Shape	0.68	0.94	+27.8%
D-Shape ZZS	0.68	0.92	+26.4%

Table 6.8: Drag values obtained through the MCV and the EWA approaches with relative percentage difference.

6.3.2 Airfoil Drag quantification

The plot reported in Fig.6.18 report the drag coefficients obtained through the MCV approach for the NACA-0012 airfoil at three different incidences. For the low-incidence cases, the term giving the major positive contribution in the near-wake is the momentum one. That is mostly due to the presence of low-positive velocity values right after the airfoil trailing edge. The trend of the momentum term varies between the airfoil at null-incidence and the one at 5°. In the former case, the momentum term rapidly decreases moving downstream; that is mostly due to the fast velocity recovery in the streamwise direction. At approximatively $0.95D$, the slope reaches a plateau and remains constant in the far-wake. On the other hand, the airfoil at 5° incidence shows a much slower decrease rate; furthermore, in this case no constant trend can be appreciated in the far-wake.

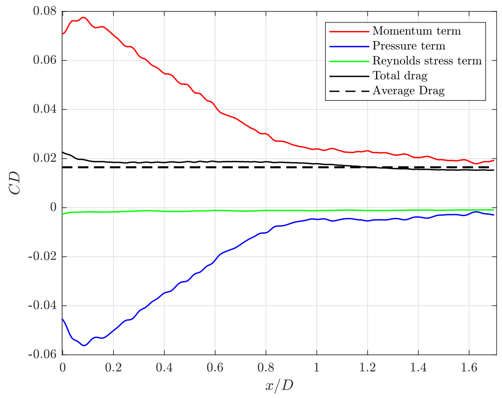

(a) NACA-0012 at 0°

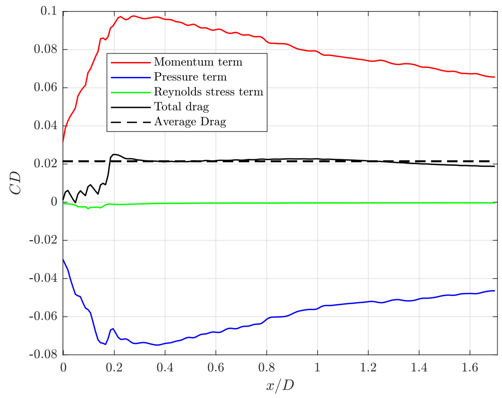

(b) NACA-0012 at 5°

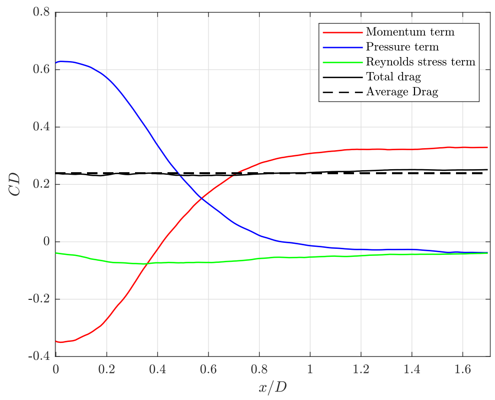

(c) NACA-0012 at 15°

Figure 6.18: Drag coefficient obtained through the MCV approach as a function of the streamwise distance.

The pressure term shows the opposite trend. In agreement with the observations made in Section 6.2.3, the flow experiences compression in the wake fields of the airfoil at low-incidence angles. Such an effect fades moving downstream, thus leading to an increase of the overall drag force. As for the momentum term, the trend of the curve varies from the airfoil at 0° of incidence to the one at 5°. For the first case, the pressure rapidly decreases reaching almost null values at half of the domain. Hence, the momentum term is the main contributor to the drag in the far-wake. The slope of the 5° pressure-term curve is much lower, hence, not-null negative pressure values are reached in the far-wake. The typical behavior of a bluff body has been observed for the stalled airfoil. The pressure term offers the main positive contribution to the drag in the near-wake, meanwhile, the momentum term acts as a thrust force. Moving downstream, the momentum term becomes positive and the pressure term reaches slightly negative values. All of the analyzed configurations achieve an overall constant drag in the streamwise direction. Due to the low-velocity oscillation, the Reynolds stress term gives a neglectable contribution to the drag in the low-incidence configurations. Nonetheless, an higher negative contribute is instead present for the airfoil at 15°. The results obtained through the EWA model are reported in Fig.6.19.

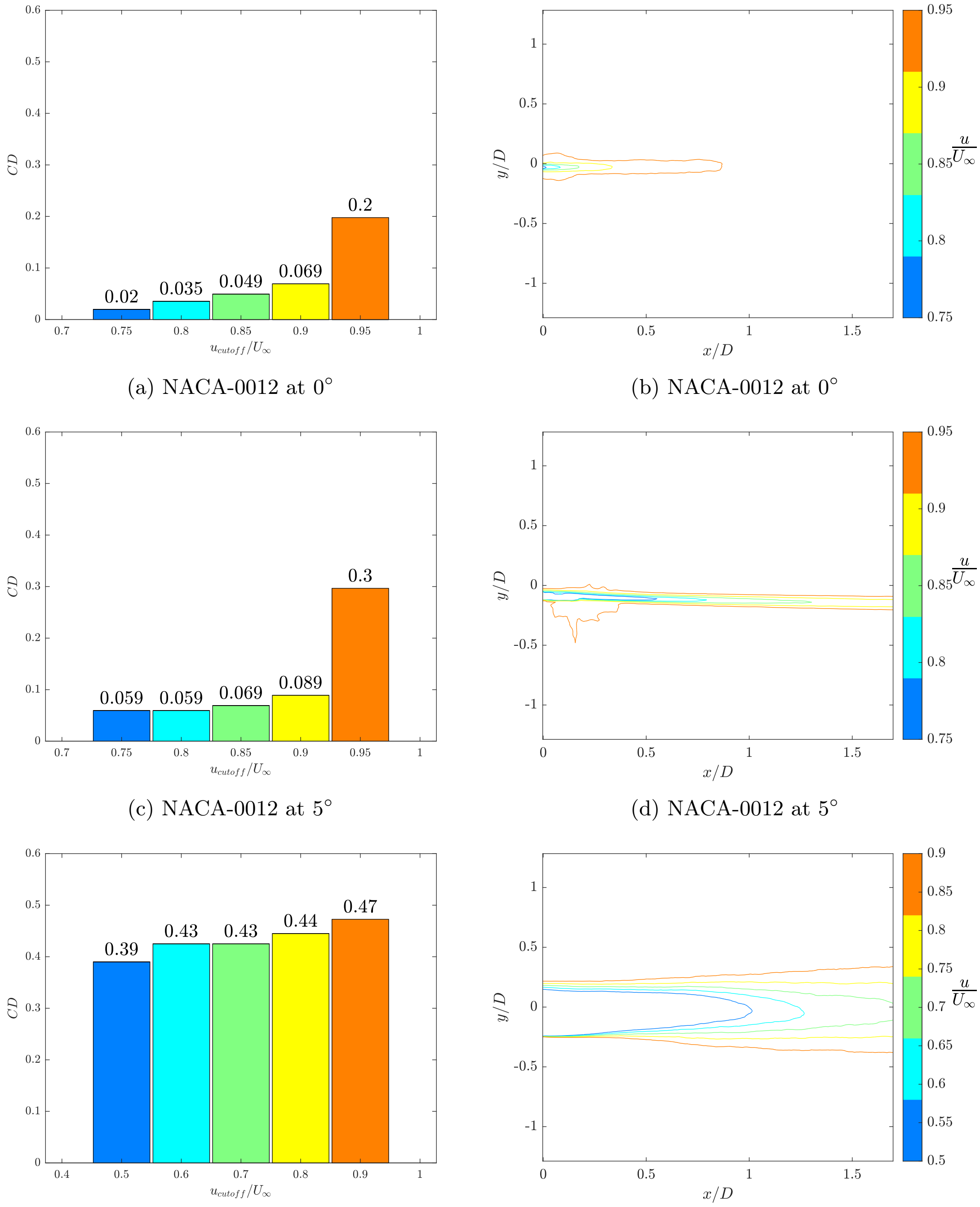

(a) NACA-0012 at 0°

(b) NACA-0012 at 0°

(c) NACA-0012 at 5°

(d) NACA-0012 at 5°

(e) NACA-0012 at 15°

(f) NACA-0012 at 15°

Figure 6.19: Velocity contour-lines corresponding to the chosen cut-off velocity (Left), Drag coefficient obtained through the EWA approach as a function of the cut-off velocity parameter (Right).

Geometry	$\Delta CD(0.8U_\infty)$	$\Delta CD(0.85U_\infty)$	$\Delta CD(0.9U_\infty)$	$\Delta CD(0.95U_\infty)$
NACA-0012 (0°)	44.2%	60%	71.4%	90%
NACA-0012 (5°)	0%	14.2%	33.3%	90%
Geometry	$\Delta CD(0.6U_\infty)$	$\Delta CD(0.7U_\infty)$	$\Delta CD(0.8U_\infty)$	$\Delta CD(0.9U_\infty)$
NACA-0012 (15°)	8.3%	8.3%	12.3%	17.5%

Table 6.9: Percentage differences in the drag coefficients obtained for different cut-off velocities with respect to the drag coefficient obtained for the standard cut-off velocity.

All the contoured regions result closed for the airfoil at 0°; on the other hand, the region corresponding to $0.9U_\infty$ and $0.95U_\infty$ are open for the airfoil at 5°. In the latter case, the wake-contoured regions appear to be more elongated; nonetheless, the width of those areas are narrow, thus leading to low drag coefficients.

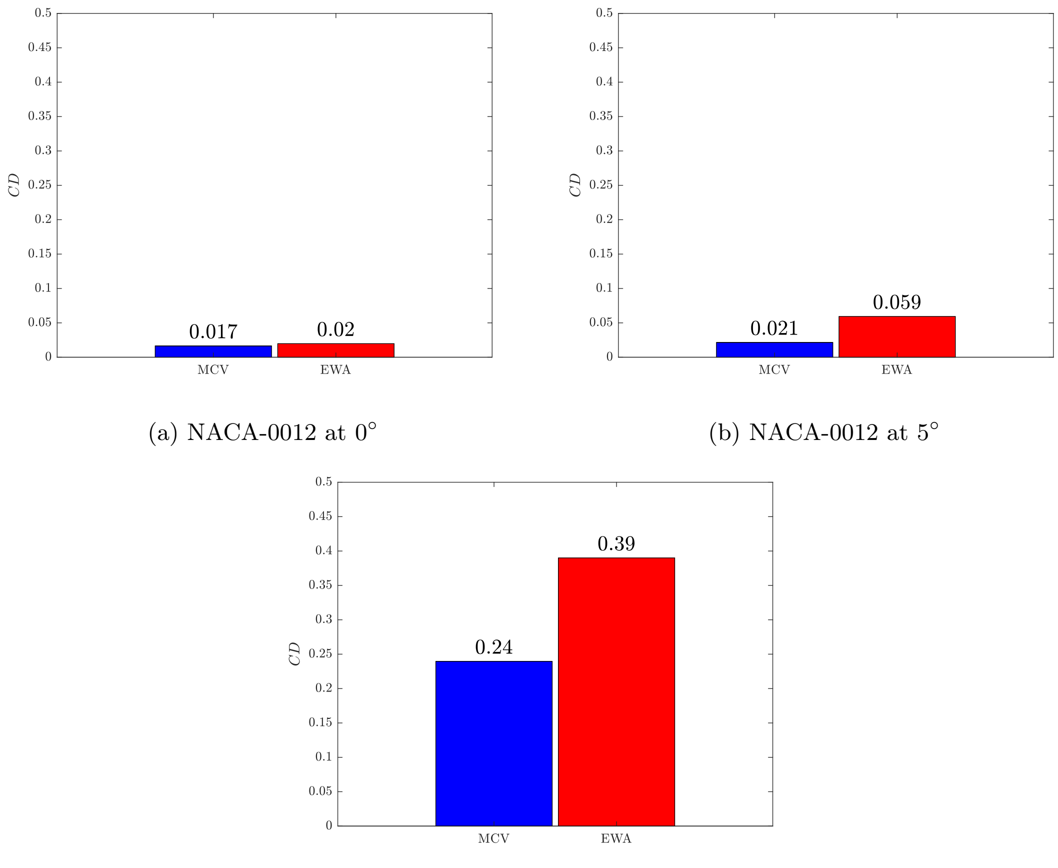

(a) NACA-0012 at 0°

(b) NACA-0012 at 5°

(c) NACA-0012 at 15°

Figure 6.20: Comparison between EWA and MCV models' drag coefficients.

On the other hand, the contoured wake's region appears wider for the airfoil in a stalled configuration. The drag coefficients obtained through the EWA approach are reported in Tab.6.9. Contrary to the bluff bodies' cases, this approach results much more sensitive for streamlined bodies. That is especially true for the last cut-off velocity, for which percentage differences between 80% and 90% are reached. Nonetheless, the sensitivity of the model seems to decrease with the incidence; the stalled configuration shows a much lower dependency on the cut-off velocity. The results obtained through the two approaches have been reported and compared in Fig. 6.20. The best agreement between the two models is presented by the null-incidence configuration; the difference in drag is about 16.6%. Despite the good agreement for such a case, higher discrepancies have been found for the remaining configurations. In particular, the airfoil at 5° exhibits a major difference of 73.5%; meanwhile, the configuration at 15° shows a 38.5% of difference between the two approaches. The drag coefficients obtained through the two models and the relative percentage differences have been summarized in Tab.6.10.

Geometry	CD_{MCV}	CD_{EWA}	ΔCD
NACA-0012 (0°)	0.017	0.02	+16.5%
NACA-0012 (5°)	0.021	0.059	+73.5%
NACA-0012(15°)	0.24	0.39	+38.5%

Table 6.10: Drag values obtained through the MCV and the EWA approaches with relative percentage difference

Geometry	**Symbol**
Circular body	C
Circular body with Zig-Zag strips	CZZS
Triangle	T
Reverse Triangle	RT
D-Shape body	D
D-Shape body with the strips	DZZS

Table 6.11: Bluff Bodies Nomenclature

Chapter 7

Conclusions and Recommendations

This project proposes a novel approach for the aerodynamic drag estimation of constant-speed translating objects. The new model found its bases in the energy exchange between the fluid and a moving body; hence, it has been named as Energized Wake Area (EWA) model. In order to evaluate its feasibility, an experimental campaign has then been conducted. Wind tunnel 2D2C-Particle Image Velocimetry (PIV) measurements were taken in the wake of different 2D bluff bodies. Finally, the acquired data-sets have been used to assess the new model, by comparing it with the Momentum Control Volume (MCV) approach. The conclusions of the investigations are drawn and exposed in the first section of this chapter. Finally, the author's recommendations for the next developments of the model and future works are presented in the chapter's final part.

7.1 Conclusions

Aerodynamic loads' estimation techniques have experienced a fast evolution during the years, especially in the determination of aerodynamic drag. Despite the huge improvements, most of them are still not capable of providing a physical relationship with the flow field. Nonetheless, the momentum conservation inside a control volume has been proven to be effective in that sense; however, this kind of approach is complex and usually presents some drawbacks. To reduce the complexity for the aerodynamic drag estimation, while still providing the relationship between the flow topologies and drag, is the main motivation behind the development of the approach developed in this project.

The accuracy of the new model has been investigated by determinating the drag of different 2D bluff and streamlined bodies, by means of 2D2C PIV measurements. The test cases were chosen in such a way that a range of drag coefficients between 0.6 and 2 was provided for the analysis at Reynolds numbers between 60×10^4 and 10^5. The tested bodies include a circular body, a triangle one with the vertex facing the flow, a triangle one with the flat edge facing the flow, an elongated D-Shape body and a NACA-0012 airfoil. Furthermore, the drag coefficients range was enlarged by modifying the geometric configuration of the test cases. Incidence variations were adopted for the airfoil to achieve higher drag values. A passive flow control device (Zig-Zag Strips) was instead applied to the circular and the D-Shape bodies to reduce the drag. Despite successfully achieving a drag reduction for circular body, both the flow topologies and the retrieved drag values suggest an ineffectiveness of such a device in the D-Shape case. As a recommendation for future works, the author deems it appropriate either to use strips with a higher relative thickness or to increase the Reynolds number in order to trigger the transition.

Being the model based on a velocity-contouring approach, the sensitivity of the model to the cut-off velocity parameter has been investigated. The sensitivity of the model has proven to be generally low for bluff bodies. For cut-off velocity values lower $0.9U_\infty$, the difference in drag with respect to the drag value obtained through the standard cut-off velocity doesn't change more than the 5%. The D-Shape body with the strips and the reverse triangle case result slightly more sensitive, drag percentage differences between 6% and 8% have been observed. On the other hand, the model results highly sensitive to such a parameter in the case of a streamlined body. For the airfoil at 0° and 5°, discrepancies up to 90% have been found, on the other hand, the airfoil at 15° shows a much lower degree of sensitivity.

A comparison between the EWA model and the conservation of momentum in a control volume was carried out, in order to assess the accuracy of the new approach. Particularly good agreement between the two methods was found for the circular body; in that case, a drag difference of 1% was found between the two methods. Also, good agreements were found for the triangular cases, presenting differences lower than 11%. Major discrepancies of approximately 30% were instead found for the circular body with the strips and both the D-Shape bodies. Good agreements between the two approaches are shown by the airfoil cases, with the best one corresponding to the most streamlined configuration at 0°. In that case, the percentage difference between the two models is 16%. On the other hand, the EWA model is not able of accurately estimate the drag for both the not-null incidence configurations. The difference between the two approaches is about 73.5% for the airfoil at 5° and 38% for one at 15°. Nonetheless, the approach has proven to be effective in capturing the drag's increase with the angle of attack.

It can be concluded that the EWA model has successfully proven to be capable of capturing the drag's order of magnitude for all the test cases. Hence, the main goal of the present thesis:

"*Assess the feasibility of a novel drag-estimating approach (Energized Wake Area), developed for reducing the complexity of aerodynamic drag estimation, while still providing a physical relationship with the wake-field.*"

Has been successfully achieved. The experimental investigations lead the author to conclude that, the presented model is able to provide an accurate estimate of the drag for simple-shape bluff bodies (e.g. circular bodies and triangles) and streamlined ones (e.g. symmetric airfoils at null-incidence). On the other hand, more sophisticated configurations (e.g control flow devices, elongated afterbodies, and incidence angles) have proven to be too complex for the model at its current state. Possible recommendations for improving the model and suggestions for future works are discussed in the next section.

7.2 Recommendations

The Energized Wake Area model is still in its infancy; hence, several improvements can be thought of to improve its effectiveness.

Despite successfully providing the drag coefficients' order of magnitude, the model has proven not to be able to accurately estimate the drag for all the test cases. The author suggests a review of the model's base assumptions to achieve further improvements in that sense. Currently, the energized portion of the wake has been approximated as a cylinder, thus obtaining a simplified expression for the drag coefficient. Nonetheless, a more accurate definition of the volume of the fluid energized by the body's passage can lead to a better estimation of the drag coefficient.

The velocity-based contouring method described in Section 5.5 can be improved in order to achieve higher accuracy. On the other hand, the current area-projection method consists of a simple linear interpolation onto the body's trailing edge. Such an approach is analytically correct for bodies presenting a flattened trailing edge; however, it does not account for the actual shape of the object's backside in the case of rounded, pointed trailing edges. Hence, a more refined projecting approach could be implemented for more complex geometries.

Possible future applications of the proposed method concern the application of the model on more complex three-dimensional geometries. However, the implementation of this novel approach for the latter would require the use of more advanced 3C measurement techniques.

Finally, the EWA model indeed shows an intriguing perspective towards the determination of aerodynamic drag of large-scale moving bodies. The author highly recommends the implementation of the model in the innovative large-scale Stereoscopic-PIV *Ring of Fire* system, described in Section 3.3. Nonetheless, it has to be accounted that the EWA approach is still in its infancy; hence, its effectiveness on complex multi-scale flows still needs to be assessed.

Bibliography

Anderson Jr, John D (1985). *Fundamentals of aerodynamits.*

Balmford, Andrew, Adrian LR Thomas, and Ian L Jones (1993). "Aerodynamics and the evolution of long tails in birds". In: *Nature* 361.6413, pp. 628–631.

Batchelor, Cx K and GK Batchelor (2000). *An introduction to fluid dynamics.* Cambridge university press.

Benjamin, T Brooke (1986). "Note on added mass and drift". In: *Journal of Fluid Mechanics* 169, pp. 251–256.

Buresti, Guido (1998). "Vortex shedding from bluff bodies". In: *Wind effects on buildings and structures*, pp. 61–95.

Caridi, Giuseppe Carlo Alp (2018). "Development and application of helium-filled soap bubbles: For large-scale PIV experiments in aerodynamics". In.

Carmody, Thomas (1964). "Establishment of the wake behind a disk". In.

Cheeseman, IC (1976). "Fluid-Dynamic Drag: Practical Information on Aerodynamic Drag and Hydrodynamic Resistance. SF Hoerner. Hoerner Fluid Dynamics, Brick Town, New Jersey. 1965. 455 pp. Illustrated. 24.20.". In: *The Aeronautical Journal* 80.788, pp. 371–371.

Crowe, C et al. (1998). "Multiphase Flows with Droplets and Particles CRC". In: *Boca Raton, FL.*

Dabiri, Dana (2006). "Cross-correlation digital particle image velocimetry-a review". In: *Turbul. ABCM Curitiba*, pp. 155–199.

Dabiri, John O (2006). "Note on the induced Lagrangian drift and added-mass of a vortex". In: *Journal of Fluid Mechanics* 547, pp. 105–113.

Darwin, Charles (1953). "Note on hydrodynamics". In: *Mathematical Proceedings of the Cambridge Philosophical Society.* Vol. 49. 2. Cambridge University Press, pp. 342–354.

David, Laurent, Thierry Jardin, and Alain Farcy (2009). "On the non-intrusive evaluation of fluid forces with the momentum equation approach". In: *Measurement Science and Technology* 20.9, p. 095401.

Eames, I, SE Belcher, and JCR Hunt (1994). "Drift, partial drift and Darwin's proposition". In: *Journal of Fluid Mechanics* 275, pp. 201–223.

Elsinga, GE and J Westerweel (2012). "Tomographic-PIV measurement of the flow around a zigzag boundary layer trip". In: *Experiments in fluids* 52.4, pp. 865–876.

Elsinga, GE, J Westerweel, et al. (2011). "On the velocity of ghost particles and the bias errors in Tomographic-PIV". In: *Experiments in fluids* 50.4, pp. 825–838.

F.Scarano, 2013a (2013a). *Experimental aerodynamics. Delft University of Technology,Course reader, Flow Measurement Techniques (AE4-180).*

Fei, R and W Merzkirch (2004). "Investigations of the measurement accuracy of stereo particle image velocimetry". In: *Experiments in fluids* 37.4, pp. 559–565.

Galler, Joshua N, Gabriel D Weymouth, and David E Rival (2021). "On the concept of energized mass: A robust framework for low-order force modeling in flow past accelerating bodies". In: *Physics of Fluids* 33.5, p. 057103.

Greenewalt, Crawford H (1975). "The flight of birds: the significant dimensions, their departure from the requirements for dimensional similarity, and the effect on flight aerodynamics of that departure". In: *Transactions of the American philosophical society* 65.4, pp. 1–67.

Gurka, Roi et al. (2017). "Flow pattern similarities in the near wake of three bird species suggest a common role for unsteady aerodynamic effects in lift generation". In: *Interface focus* 7.1, p. 20160090.

Gutierrez, Eric et al. (2016). "Lift calculations based on accepted wake models for animal flight are inconsistent and sensitive to vortex dynamics". In: *Bioinspiration & biomimetics* 12.1, p. 016004.

Håkansson, Jonas et al. (2015). "The wake of hovering flight in bats". In: *Journal of The Royal Society Interface* 12.109, p. 20150357.

Hinsch, Klaus D (1995). "Three-dimensional particle velocimetry". In: *Measurement Science and Technology* 6.6, p. 742.

Hirsch, Max (2018). "Accuracy assessment of the Ring of Fire system for on-site aerodynamic drag measurements". In.

Jux, Constantin et al. (2018). "Robotic volumetric PIV of a full-scale cyclist". In: *Experiments in Fluids* 59.4, pp. 1–15.

KarlTaylorEducation (Feb. 2020). *Aperture and Depth of Field.* URL: `https://www.lavision.de/en/techniques/piv-ptv/`. Accessed on: 17.11.2021.

Kat, Roeland de and Bas W van Oudheusden (2010). "Instantaneous planar pressure from PIV: analytic and experimental test-cases". In: *Proceedings of the 15th international symposium on applications of laser techniques to fluid mechanics, Lisbon, Portugal.*

Koradiya, Jaydeep (2018). "Cylinder drag reduction by geometric modification in 3-Diameter confined space: Towards speed skiing application". In.

Kurtulus, DF, F Scarano, and L David (2007). "Unsteady aerodynamic forces estimation on a square cylinder by TR-PIV". In: *Experiments in fluids* 42.2, pp. 185–196.

LaVision (June 2017). *Particle Image Velocimetry techniques.* URL: `https://www.lavision.de/en/techniques/piv-ptv/`. Accessed on: 17.11.2021.

— (n.d.). *PIV Image Evaluation.* URL: `https://www.piv.de/piv/measurement_principle/page_1.php`. Accessed on: 17.11.2021.

Lentink, David, Andreas F Haselsteiner, and Rivers Ingersoll (2015). "In vivo recording of aerodynamic force with an aerodynamic force platform: from drones to birds". In: *Journal of The Royal Society Interface* 12.104, p. 20141283.

Lighthill, MJ (1956). "Drift". In: *Journal of Fluid Mechanics* 1.1, pp. 31–53.

Liu, Zhengliang et al. (2006). "Stereoscopic PIV studies on the swirling flow structure in a gas cyclone". In: *Chemical Engineering Science* 61.13, pp. 4252–4261.

Loboda, Egor L et al. (2018). "Evaluating characteristics of turbulent flames by using IR thermography and PIV". In: *Infrared Physics & Technology* 92, pp. 240–243.

Mahalingesh, Nikhil (2020). "On-site drafting aerodynamics of cyclists using the Ring of Fire". In.

Martino Norante, Luigi de (2018). "Advances and assessment of the Ring of Fire concept for on-site cycling aerodynamics". In.

McPhaden, Cameron J and David E Rival (2018). "Unsteady force estimation using a Lagrangian drift-volume approach". In: *Experiments in Fluids* 59.4, pp. 1–11.

Meerendonk, Remco van de, Mustafa Percin, and Bas W van Oudheusden (2016). "Three-dimensional flow and load characteristics of flexible revolving wings at low Reynolds number". In: *18th Int. Symp. Appl. Laser Techn. Fluid Mech.*

Meinhart, Carl D, Steve T Wereley, and Juan G Santiago (1999). "PIV measurements of a microchannel flow". In: *Experiments in fluids* 27.5, pp. 414–419.

Muijres, Florian T et al. (2012). "Comparing aerodynamic efficiency in birds and bats suggests better flight performance in birds". In: *PloS one* 7.5, e37335.

Nakagawa, Takeo (1989). "Vortex shedding mechanism from a triangular prism in a subsonic flow". In: *Fluid dynamics research* 5.2, p. 69.

Nedić, J, Bharath Ganapathisubramani, and John Christos Vassilicos (2013). "Drag and near wake characteristics of flat plates normal to the flow with fractal edge geometries". In: *Fluid Dynamics Research* 45.6, p. 061406.

Parezanović, Vladimir and Olivier Cadot (2012). "Experimental sensitivity analysis of the global properties of a two-dimensional turbulent wake". In: *Journal of Fluid Mechanics* 693, pp. 115–149.

Pattnaik, Pallav (2017). "Aerodynamic investigation of the near wake flow topology on a two-man bobsleigh". In.

Prasad, AK et al. (1992). "Effect of resolution on the speed and accuracy of particle image velocimetry interrogation". In: *Experiments in Fluids* 13.2, pp. 105–116.

Raffel, Markus et al. (2018). *Particle image velocimetry: a practical guide.* Springer.

Ragni, D, BW Van Oudheusden, and F Scarano (2012). "3D pressure imaging of an aircraft propeller blade-tip flow by phase-locked stereoscopic PIV". In: *Experiments in fluids* 52.2, pp. 463–477.

Rival, David E and Bas Van Oudheusden (2017a). "Load-estimation techniques for unsteady incompressible flows". In: *Experiments in Fluids* 58.3, pp. 1–11.

— (2017b). "Load-estimation techniques for unsteady incompressible flows". In: *Experiments in Fluids* 58.3, pp. 1–11.

Santiago, Juan G et al. (1998). "A particle image velocimetry system for microfluidics". In: *Experiments in fluids* 25.4, pp. 316–319.

Scarano, F, C van Wijk, and LJEIF Veldhuis (2002). "Traversing field of view and AR-PIV for mid-field wake vortex investigation in a towing tank". In: *Experiments in fluids* 33.6, pp. 950–961.

Scarano, Fulvio (2012). "Tomographic PIV: principles and practice". In: *Measurement Science and Technology* 24.1, p. 012001.

Sciacchitano, Andrea (2014). "Uncertainty quantification in particle image velocimetry and advances in time-resolved image and data analysis". In.

Sciacchitano, Andrea, Fulvio Scarano, and Bernhard Wieneke (2012). "Multi-frame pyramid correlation for time-resolved PIV". In: *Experiments in fluids* 53.4, pp. 1087–1105.

Sciacchitano, Andrea and Bernhard Wieneke (2016). "PIV uncertainty propagation". In: *Measurement Science and Technology* 27.8, p. 084006.

Spedding, Geoffrey R and Anders Hedenström (2010). "PIV-based investigations of animal flight". In: *Animal Locomotion.* Springer, pp. 187–201.

Spedding, GR, Mikael Rosén, and Anders Hedenström (2003). "A family of vortex wakes generated by a thrush nightingale in free flight in a wind tunnel over its entire natural range of flight speeds". In: *Journal of Experimental Biology* 206.14, pp. 2313–2344.

Spoelstra, Alexander (2017). "Aerodynamics of transiting objects via large-scale PIV-the Ring of Fire Concept". In.

Spoelstra, Alexander, Maximilian Hirsch, et al. (2020). "Uncertainty assessment of the Ring of Fire concept for on-site aerodynamic drag evaluation". In: *Measurement Science and Technology.*

Spoelstra, Alexander, Luigi de Martino Norante, et al. (2019). "On-site cycling drag analysis with the Ring of Fire". In: *Experiments in Fluids* 60.6, pp. 1–16.

Stephens, Richard G, Patrick RRJ Stevens, and Holger Babinsky (2016). "A method for truck underbody aerodynamic investigation". In: *SAE International Journal of Commercial Vehicles* 9.2016-01-9020, pp. 429–437.

Stevens, Patrick Robert Robbie James (2015). "Unsteady low Reynolds number aerodynamic forces". PhD thesis. University of Cambridge.

Tao, Yao et al. (2018). "Experimental visualisation of wake flows induced by different shaped moving manikins". In: *Building and Environment* 142, pp. 361–370.

Terra, W, A Sciacchitano, and F Scarano (2017). "Aerodynamic drag of a transiting sphere by large-scale tomographic-PIV". In: *Experiments in Fluids* 58.7, pp. 1–14.

Terra, W, A Sciacchitano, F Scarano, and BW van Oudheusden (2018). "Drag resolution of a PIV wake rake for transiting models". In: *Experiments in Fluids* 59, pp. 1–6.

Thomas, Adrian LR (1993). "On the aerodynamics of birds' tails". In: *Philosophical Transactions of the Royal Society of London. Series B: Biological Sciences* 340.1294, pp. 361–380.

Tobalske, Bret W, Jason WD Hearn, and Douglas R Warrick (2010). "Aerodynamics of intermittent bounds in flying birds". In: *Animal Locomotion*. Springer, pp. 401–411.

Tucker, Vance A and G Christian Parrott (1970). "Aerodynamics of gliding flight in a falcon and other birds". In: *Journal of Experimental Biology* 52.2, pp. 345–367.

TUDelft (Mar. 2021). *Measuring system using laser beams and helium bubbles helps top skaters go for gold.* URL: `https://www.tudelft.nl/en/2021/tu-delft/measuring-system-using-laser-beams-and-helium-bubbles-helps-top-skaters-go-for-gold`. Accessed on: 17.11.2021.

Turkoz, Emre and Murat Celik (2015). "AETHER: A simulation platform for inductively coupled plasma". In: *Journal of Computational Physics* 286, pp. 87–102.

Usherwood, James R et al. (2020). "High aerodynamic lift from the tail reduces drag in gliding raptors". In: *Journal of experimental biology* 223.3.

Van Oudheusden, BW (2013). "PIV-based pressure measurement". In: *Measurement Science and Technology* 24.3, p. 032001.

Van Oudheusden, BW, F Scarano, and EWF Casimiri (2006). "Non-intrusive load characterization of an airfoil using PIV". In: *Experiments in Fluids* 40.6, pp. 988–992.

Wang, Junwei et al. (2012). "Experimental study of spoiler influence to delta wing generated vortex in water towing tank". In.

Westerweel, Jerry and Fulvio Scarano (2005). "Universal outlier detection for PIV data". In: *Experiments in fluids* 39.6, pp. 1096–1100.